Theoretical Studies of Molecule-substrate Interaction at Complex Gold and Silicon Oxide Surfaces Using Surface and Cluster Models

by

Chao-Ming Ting

B.Sc., University of Victoria, 2012

A Dissertation Submitted in Partial Fulfillment of the

Requirements for the Degree of

DOCTOR OF PHILOSOPHY

in the Department of Chemistry

© Chao-Ming Ting, 2020

University of Victoria

All rights reserved. This dissertation may not be reproduced in whole or in part, by photocopying or other means, without the permission of the author.

Theoretical Studies of Molecule-substrate Interaction at Complex Gold and Silicon Oxide Surfaces Using Surface and Cluster Models

by

Chao-Ming Ting

B.Sc., University of Victoria, 2012

Supervisory Committee

Dr. Irina Paci, Supervisor

(Department of Chemistry)

Dr. David Harrington, Departmental Member

(Department of Chemistry)

Dr. Dennis Hore, Departmental Member

(Department of Chemistry)

Dr. Michel Lefebvre, Outside Member

(Department of Physics and Astronomy)

ABSTRACT

The formation and patterns of a monolayer are determined by the interplay of two fundamental interactions, adsorbate-substrate and intermolecular interactions. The binding strength between adsorbate and substrate affects the mobility of the adsorbate at the surface and the stability of the complex. The intermolecular interaction plays a significant role in the monolayer patterns on the epitaxial layer of the substrate. A monolayer can be formed either by a spontaneous self-assembly, or by fabrication via atomic-layer deposition (ALD). The physical and chemical properties of the resulting monolayer have a broad array of applications in fabricating functional materials for hydrophobic or hydrophilic surfaces, biological sensors, alternating the properties of the substrate, catalysis and forming ordered layered structures. In this dissertation, the investigation focuses primarily on the influence of the surface topology on the binding behaviour of adsorbate-surface complexes. The state of the art DFT-TS method is used to simulate the sulfur-containing amino acids at complex gold surfaces and examine the relationship between the binding strengths and the binding sites with various nearest neighbouring environments. The same method is also used to determine if a chemical reaction will take place for various catalytic silicon precursors at a silicon oxide surface.

Simulating surface chemistry using the DFT-TS method requires intensive computing resources, including CPU use and computing time. Another focus of this dissertation is to increase the data generating speed by reducing the size of the simulated systems without altering the outcome. A relatively small gold cluster is used to study the binding behaviours of small organic molecules on the cluster. The same strategy is also used to simulate the chemical reactions between various self-catalying silicon precursors and a water molecule.

Contents

Supervisory Committee **ii**

Abstract **iii**

Table of Contents **iv**

List of Tables **viii**

List of Figures **x**

List of Abbreviations **xvi**

List of Abbreviations **xvi**

Acknowledgements **xviii**

Dedication **xix**

1 Introduction **1**

1.1 Functionalized monolayer on a metallic surface 1

1.2 Silicon-based monolayer on a SiO_2 surface 4

1.3 Interaction on the interfacial layer 6

1.4 Sulfur-containing amino acids on gold surfaces 7

1.4.1 The correlation of the binding site reactivities and their coordination numbers 7

1.4.2 Targeting substrate and adsorbate pairs 9
1.4.3 The phenomenon of chiral recognition and separation for racemic mixtures of chiral adsorbates 10
1.5 Chemical deposition of silicon precursors on an ideal SiO_2 surface using ALD 13
1.5.1 High-temperature ALD 13
1.5.2 Catalytic silicon precursors for lower temperature ALD 16
1.5.3 Establishing a predictable model 19
1.6 The objectives of my studies 21
1.7 Outline 21

2 Methodology **23**

2.1 Introduction 23
2.2 Density-functional method approach 28
2.2.1 The total energy equations 29
2.2.2 Geometry optimization 32
2.2.3 Pseudo-atomic orbital basis set 34
2.2.4 Periodic boundary conditions 36
2.2.5 The binding energy equations 37
2.3 Improvement and Corrections 37
2.3.1 Basis set superposition error and counterpoise method 38
2.3.2 Energy shift and PAO cutoff 40
2.3.3 Van der Waals corrections 42
2.4 Limitations of the DFT method 49
2.5 Conclusions 51

3 Coordination Numbers and Binding Reactivities **52**

3.1 Introduction 52
3.2 Methodology 54
3.3 Results and Discussion 57
3.3.1 Dissociative adsorption: the methyl-thiolate form 57
3.3.2 Non-dissociative adsorption: the methylthiol form 62
3.3.3 A stronger dispersive interaction: the dimethyl sulfide 64
3.3.4 A lone-pair to metal interaction: the methylamine 67
3.4 Conclusions 70

4 Amino Acids on Complex Gold Surfaces 71
4.1 Introduction 71
4.2 Methodology 74
4.2.1 Models 75
4.2.2 Numerical details 76
4.3 Results and Discussion 77
4.3.1 Amino acid adsorption at the ideal Au(111) surface 77
4.3.2 Amino acid dimers in the gas phase 90
4.3.3 Amino acid dimers on Au(111) 91
4.3.4 AA monomers on an adatom defect gold surface 100
4.4 Conclusion 109

5 Atomic Layer Deposition on a Silicon Oxide Surface 111
5.1 Introduction 111
5.2 Methodology 114
5.3 Results and Discussion 116
5.3.1 Catalyst adsorption on the SiO_2 slab 116
5.3.2 Self-catalying silicon precursors on a SiO_2 slab 121

5.3.3 Hydrolysis reaction for self-catalying precursors 126
5.4 Conclusion 131

6 General Conclusions and Future Work **132**
6.1 General conclusions 132
6.2 Future work 135

Bibliography **137**

List of Tables

Table 2.1 Binding energies of MeSH and MeS–Au_{20} complexes on the binding sites with various neighbours using various simulation settings. 35

Table 2.2 Binding energies of zwitterionic, chemisorbed and physisorbed cysteine monomer and dimer on Au(111) surface 48

Table 2.3 Computational costs for various simulating systems in this thesis. 50

Table 3.1 Binding energies and relevant distances for MeS–Au adsorption. 61

Table 3.2 Binding energies and relevant distances for MeSH–Au adsorption. 63

Table 3.3 Binding energies and relevant distances for Me_2S–Au adsorption. 65

Table 3.4 Binding energies and relevant distances for $MeNH_2$–Au adsorption. 69

Table 4.1 CP corrected binding energies and distances for adsorbed non-ionic cysteine, homocysteine and methionine configurations on the Au(111) surface. 78

Table 4.2 CP corrected binding energies and distances for cooperatively adsorbed homocysteine and methionine on Au(111) surface. . 83

Table 4.3 CP corrected binding energies and distances for adsorbed unconventional zwitterionic cysteine and homocysteine on Au(111) surface. 89

Table 4.4 CP corrected binding energies and the corresponding intermolecular interactions for cysteine, homocysteine and methionine dimers in the gas phase. 90

Table 4.5 CP corrected binding energies and distances for adsorbed cysteine, homocysteine and methionine dimers with COOH – COOH interaction on Au(111) surface. 94

Table 4.6 CP corrected binding energies and distances for adsorbed cysteine, homocysteine and methionine dimers with COOH – (NH_2,OH) interaction on the Au(111) surface. 95

Table 4.7 CP corrected binding energies and distances for adsorbed homocysteine and methionine *dimers* with (NH_2,OH) – (OH,NH_2) binding motif on Au(111) surface. 97

Table 4.8 CP corrected binding energies and distances for adsorbed zwitterionic cysteine dimer and nonionic homocysteine dimer with partial charge interaction on the Au(111) surface. 99

Table 4.9 CP corrected binding energies and distances for adsorbed unconventional zwitterionic cysteine and homocysteine on the adatom surface. 101

Table 4.10 CP corrected binding energies and distances for cooperatively adsorbed amino acids on the adatom surface. 106

Table 4.11 CP corrected binding energies and distances for adsorbed nonionic amino acids on the adatom surface. 109

Table 5.1 pK_a values for some N-containing catalysts. 117

List of Figures

Figure 1.1 Schematic diagram of an ideal self-assembled monolayer of alkanethiols/alkanethiolates mixture on an Au(111) substrate. 2

Figure 1.2 Sulfur-containing amino acids: **(a)** *L*-cysteine, **(b)** *L*-homocysteine and **(c)** *L*-methionine. 3

Figure 1.3 Cross-sectional SEM image of an Al_2O_3 film with a thickness of 300 nm on a Si wafer with a trench structure using ALD technique. 5

Figure 1.4 The *L*-cysteine dimer structure at the four-atom vacancy reconstructed Au(110)-(1×2) gold surface. 9

Figure 1.5 Schematic representation of ALD in self-limiting and sequential fashion. 14

Figure 1.6 The chemical reaction of the precursor (Di(pyrrolidinyl)dimethoxysilane) and a water molecule at the transition state via a four-membered ring reaction mechanism. 17

Figure 2.1 The formation of the zwitterionic cysteine was proposed to occur under higher surface coverage on Au(111) surface. . . . 25

Figure 2.2 Schematic diagram of preparation of alkanethiolates SAM on a Au(111) substrate. The head group here is thiol/thiolate functional group. 25

Figure 2.3 Schematic diagram of the silicon cycle using silicon tetrachloride as the precursor on a silicon oxide (SiO_2) surface. 26
Figure 2.4 Optimized configurations using classical MD and DFT optimization. 27
Figure 2.5 J. Perdew's metaphorical Jacob's ladder for the five generations (rungs) of DFT functionals. 30
Figure 2.6 Schematic diagram of illustrating the simulation algorithm which can be geometry optimization or molecular dynamics. 33
Figure 2.7 Cutoff radius dependence of the binding energy. 41
Figure 2.8 Optimized chemisorbed geometries of protonated cysteine on Au(110)-(1×2) missing row surface with two orbital cutoff R_c values for the first ζ pseudo-orbitals of the carbon atom. . . . 42
Figure 2.9 Benchmarking the simulation settings: basis sets, vdW correction and global scaling factor. 45
Figure 2.10 Comparing the values of global scaling factor s_6 with the SIESTA default value ($s_6 = 1.66$) and with the suggested value by Tkatchenko ($s_6 = 1.00$).[1,2] 47

Figure 3.1 Cluster geometry and configurational variables sampled. . . . 54
Figure 3.2 Binding energies and relevant distances for MeS dissociative adsorption on the Au_{20} cluster. 58
Figure 3.3 The most stable MeS–Au cluster binding configurations for various binding sites on the model Au_{20} cluster. 59
Figure 3.4 The most stable and a higher energy binding configurations. . 60
Figure 3.5 Representative minimum energy structures for the non-dissociative adsorption of MeSH at various binding sites on the Au_{20} cluster. 62

Figure 3.6 The binding configurations for the non-dissociative adsorption of MeSH at the kink site on the Au_{20} cluster. 63
Figure 3.7 Representative minimum energy structures for the adsorption of Me_2S at various binding sites on the Au_{20} cluster. 65
Figure 3.8 The binding configurations for the adsorption of Me_2S at the kink site on the Au_{20} cluster. 66
Figure 3.9 Binding energy contributions and bond lengths of Me_2S on the Au_{20} cluster via physisorption with strong dispersion. 66
Figure 3.10 Representative minimum energy structures for the adsorption of $MeNH_2$ at various binding sites on the Au_{20} cluster. 68
Figure 3.11 The binding configurations for the adsorption of $MeNH_2$ at the kink site on the Au_{20} cluster. 68
Figure 3.12 Binding energy contributions and bond lengths of $MeNH_2$ on the Au_{20} cluster via lone pair metal interaction. 69

Figure 4.1 Amino acids investigated in this study: **(a)** *L*-cysteine, **(b)** *L*-homocysteine and **(c)** *L*-methionine. 76
Figure 4.2 Configurations of nonionic cysteine monomer on Au(111) surface. 80
Figure 4.3 Configurations of nonionic homocysteine monomer on Au(111) surface. 81
Figure 4.4 Configurations of nonionic methionine monomer on Au(111) surface. 82
Figure 4.5 Cooperative binding configurations of homocysteine and methionine monomer on Au(111) surface. 84
Figure 4.6 Zwitterionic cysteine and homocysteine on Au(111) surface via direct proton transfer. 86

Figure 4.7 Zwitterionic cysteine monomer on Au(111) surface via indirect proton transfer. 87
Figure 4.8 Zwitterionic homocysteine monomer on Au(111) surface via indirect proton transfer. 88
Figure 4.9 Four distinct intermolecular interactions. 90
Figure 4.10 Configurations of cysteine dimer on the Au(111) surface with COOH–COOH intermolecular interaction. 92
Figure 4.11 Configurations of homocysteine and methionine dimers on Au(111) surface with COOH–COOH intermolecular interaction. 93
Figure 4.12 Configurations of zwitterionic homocysteine and methionine dimers on the Au(111) surface with COOH – (NH_2,OH) intermolecular interaction. 95
Figure 4.13 Configurations of nonionic cysteine and methionine dimers on the Au(111) surface with COOH – (NH_2,OH) intermolecular interaction. 97
Figure 4.14 Configurations of homocysteine and methionine dimers on the Au(111) surface with (NH_2,OH) – (OH,NH_2) binding motif. . 98
Figure 4.15 Configurations of zwitterionic cysteine dimer and nonionic homocysteine dimer interacting intermolecularly via partial charge on the Au(111) surface. 99
Figure 4.16 Configurations of the unconventional zwitterionic cysteine and homocysteine monomers on the adatom surface via direct proton transfer. 102
Figure 4.17 Configurations of the unconventional zwitterionic cysteine and homocysteine monomers on the adatom surface via indirect proton transfer. 103

Figure 4.18 Cooperative binding mode of nonionic cysteine monomer with the mercapto group binding to the adatom and with the amino group binding to the adatom. 104
Figure 4.19 Cooperative binding mode of nonionic homocysteine monomer with the mercapto group binding to the adatom and with the amino group binding to the adatom. 105
Figure 4.20 Cooperative binding mode of nonionic methionine monomer with the sulfide group binding to the adatom and with the amino group binding to the adatom. 105
Figure 4.21 Configurations of nonionic cysteine on adatom surface via S–adatom and N–adatom single-coordinate bonds. 107
Figure 4.22 Configurations of nonionic homocysteine on adatom surface via S–adatom and N–adatom single-coordinate bonds. 108
Figure 4.23 Configurations of nonionic methionine on adatom surface via S–adatom and N–adatom single-coordinate bonds. 108

Figure 5.1 Trimolecular catalyzed deposition of SiO_2. 112
Figure 5.2 Structures of the selected catalysts. 117
Figure 5.3 The binding energies of the nine selected N-containing catalysts on a SiO_2 slab. 118
Figure 5.4 Configurations of the selected catalysts on a slab. 119
Figure 5.5 Conformational evolution of a pyrrolidine on a SiO_2 slab at 300 K. 120
Figure 5.6 Conformational evolution of a TMG on a SiO_2 slab at 300 K. 120
Figure 5.7 Conformational evolution of a pyridine on a SiO_2 slab at 300 K. 120
Figure 5.8 The binding configurations of H_2–Si–$(Py)_2$ and of H–Si–$(Py)_3$. 122

Figure 5.9 The binding configurations of (OMe)–Si–$(Py)_3$ and $(OMe)_2$–Si–$(Py)_2$. 123

Figure 5.10 The binding configurations of $(OMe)_3$–Si–(Py). 123

Figure 5.11 The binding configurations of $(OMe)_3$–Si–$(TMG)_1$ and $(OMe)_2$–Si–$(TMG)_2$. 125

Figure 5.12 A energy diagram of presenting reaction enthalpy (ΔH) and activation energy (ΔE_a) for a hydrolysis reaction. 127

Figure 5.13 Hydrolysis reaction pathways of the self-catalying precursor, $(OMe)_n$–Si–$(Py)_m$ where $m + n = 4$. 129

Figure 5.14 Hydrolysis reaction pathways of the self-catalying precursor, $(OMe)_n$–Si–$(TMG)_m$ where $m + n = 4$. 130

List of Abbreviations

AAs	amino acids
AIMD	*ab initio* molecular dynamics
ALD	atomic layer deposition
AP	aminopyridine
B3LYP	Becke, three-parameter, Lee-Yang-Parr
BEs	binding energies
BSSE	basis set superposition error
CNs	coordination numbers
CP	counterpoise
CVD	chemical vapour deposition
DFT	density-functional theory
DMAP	dimethylaminopyridine
DMS	dimethyl sulfide
DZP	double-zeta plus polarization functions
GGA	generalized gradient approximation
KS	Kohn-Sham
LDA	local density approximation
LJ	Lennard-Jones
LT-ALD	low temperature atomic layer deposition

MD	molecular dynamics
MR	member ring
PAOs	pseudo-atomic orbitals
PBCs	periodic boundary conditions
PBE	Perdew-Burke-Ernzerhof
PES	potential energy surface
PW	plane wave
SAMs	self-assembled monolayers
SCF	self-consistent field
SPE	single-point energy
TBD	triazabicycledecene
TMG	tetramethylguanidine
TS	transition state
TZP	triple-zeta plus polarization functions
UHV	ultra-high vacuum
vdW	van der Waals

ACKNOWLEDGEMENTS

Foremost, I would like to express my sincere gratitude to my supervisor Dr. Irina Paci for the continuous support throughout my PhD study and research, for her mentoring, knowledge, motivation, patience and encouragement. I certainly could not finish this dissertation without her guidance and constant support.

I also want to thank my second supervisor Dr. Rajesh Odedra for the internship opportunity in Seastar Chemicals Inc. company. The internship provided me with working on diverse and exciting projects.

Besides my supervisors and committee members, I would like to thank Dr. Belaid Moa for resolving all the technical difficulties relating to Compute Canada and Westgrids' supercomputers.

I would like to thank my committee members: Dr. David Harrington, Dr. Dennis Hore, Dr. Michel Lefebvre, and external examiner Dr. Yan Alexander Wang, for their encouragement, valuable comments and insightful questions.

I thank my colleagues in UVic Paci Group: Dr. Tatiana Popa, Chris Chapman, Dr. James McFarlane, Dr. Emilian Tuca, David Hally and Silvija Smith, and in other groups: Dr. Eric Janusson, Dr. Paul Gray, Brian Coleman, Fraser Burns, for endless almost-research-related discussions, for the sleepless nights on marking reports, and for all the beer we have had since 2012.

To my parents and wife Abby Xu, I here thank your patience, support and encouragement. Without you, I cannot finish this degree. To my son and two cats, I thank you for all the fun and cuddle time.

DEDICATION

I dedicate this work to my parents and my wife.

To my son Nicholas

without you

this dissertation would have been finished two years earlier.

Chapter 1

Introduction

The interactions between molecules and surfaces have been the subject of significant interest in recent years, because of their fundamental relevance in a broad array of nano-science applications. Growing or coating a layer of material on a substrate is possibly one of the most popular ways to modify the chemical, physical and electronic properties of a surface including surface reactivity, conductivity, wettability, corrosion resistance and biocompatibility.[3–6] A well-ordered one-molecule-thick functionalized monolayer can be grown on a metallic substrate spontaneously via self-assembled monolayer (SAM) formation, and can also be formed via chemical deposition.[7]

1.1 Functionalized monolayer on a metallic surface

The two-dimensional nanomaterials provide some excellent systems for the studies of interfacial and lateral interactions of various molecules-substrates combinations.[5] In general, an adsorbate consists of three parts: a head, a backbone and a functional group as shown in Fig. 1.1. The head groups are responsible for the interfacial interaction through molecule-surface binding, and the backbones and/or the end groups are responsible for the lateral interaction through van der Waals and/or Coulombic

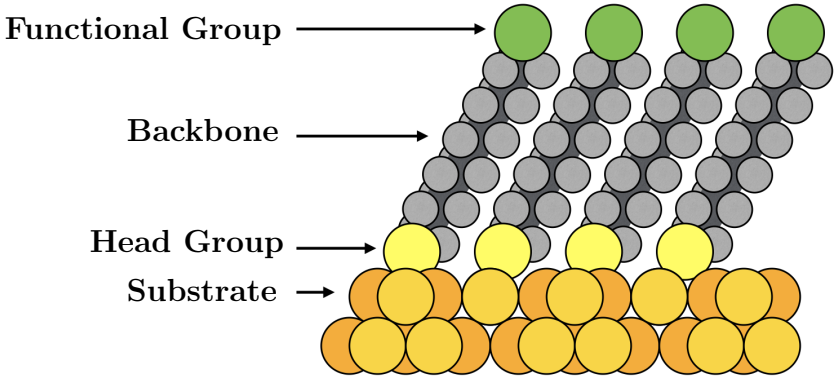

Figure 1.1: Schematic diagram of an ideal SAM of alkanethiols/alkanethiolates mixture on an Au(111) substrate. The head group is responsible for forming an immobilized layer with the substrate. The backbone acts as a linker which connects the head group and the functional group, and the thickness of a monolayer depends on the length of the backbone. The functional group is designed to perform the desired surface properties.

forces. Three common families of SAM are: a) a sulfur-containing adsorbate on a surface of the group 11 elements (copper, silver and gold),[3,6,8–11] b) alkylsilanes on oxide surfaces,[12–15] and c) carbene molecules on a gold surfaces.[4,16–20] The sulfur-containing molecules as the head group anchors on a gold surface have been long used experimentally due to their strong binding affinity and simple preparation of SAMs.[3,5,9,21] For oxide or metal oxide surfaces, the silane head group binds to the surfaces via strong Si–O bonds, and various functional groups can be synthesized onto the end of the alkyl backbones.[12–15] Carbene molecules on gold surfaces have also been studied intensively since 2013 because of its high-quality well-ordered monolayer.[4,16–20]

Applications and usages of the functionalized complex materials, from small biomedical devices to nano-electronics

One area of interfacial research has focused on the binding properties of amino acids and peptides on metal substrates,[6,9,22–27] due to the relevance of these interactions in device fabrication for biological sensors,[23,28–31] for in vivo nanoparticle imaging,

tagging, tracing and other new medicinal techniques,[26,30,32–36] and for developing a general understanding of nanoparticle biosafety,[11,37–39] among other issues. Not only the biomedical applications, many current modern electronic devices are also fabricated in a similar fashion such as devices for energy conversion,[35] organic light-emitting diode (OLED) display[40–42] and metal-oxide-semiconductor-field-effect transistor (MOSFET).[7]

Amino acids on metallic surfaces

A binding complex of the sulfur-containing amino acids (cysteine, homocysteine and methionine, shown in Fig. 1.2) on low-Miller-index [(111), (100), (110)] gold and silver surfaces is another interesting system.[3,19,25,43–55] Much is studied both experimentally

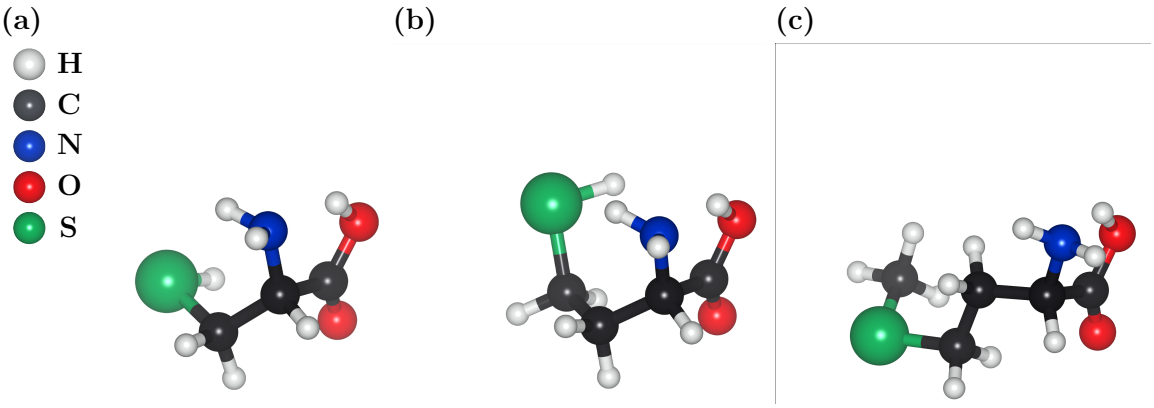

Figure 1.2: Sulfur-containing amino acids: **(a)** *L*-cysteine, **(b)** *L*-homocysteine and **(c)** *L*-methionine.

and computationally of the adsorption behaviour and binding modes; however, many questions regarding binding modes and condensed phase behaviour still remain unclear. Several classical simulation studies exist, generally focused on investigating peptide behaviour and amino acids multimer at a metal surface.[39,56–58] As computer hardware became more powerful, quantum calculations have been used to examine the behaviour of single molecules or small molecular clusters on ideal surfaces.[47,51–55,59,60]

1.2 Silicon-based monolayer on a SiO_2 surface

Two deposition methods, Chemical Vapour Deposition (CVD) and Atomic Layer Deposition (ALD) have been widely used to achieve a thin layer coating on a substrate. In general, both methods require two precursors, silicon and oxidant precursor, as the fundamental building blocks in the deposition process. The difference between the two methods is when the two precursors are introduced to the deposition chamber. CVD allows the two kinds of precursors into the deposition chamber simultaneously while ALD allows one precursor at a time, in a sequential fashion.[7] In the study of chemical deposition, our focus is on the ALD.

Chemical deposition of silicon precursors on a silicon oxide surface

CVD techniques have been used for coating a layer of substance on a substrate for over a century.[61] The advantages of the deposition technique include: higher deposition rate, a wider pressure and temperature range of the deposition chamber, and relatively cheaper than ALD.[7,61] Due to the nature of the deposition method, the thickness of a film via CVD technique is generally not thinner than 10 nm.[61] When integrated circuits (ICs) were in the micrometre scale, CVD technique served the demand.

The disadvantages of CVD as the size of the substrates is reduced

Non-uniformity of the coated layer is a known issue for the CVD technique. For example, when the aspect ratio of a substrate is relatively high (the width and the depth of opening gaps are narrow and deep), the deposition growth rate is faster on the top corners of the trench structure (see Fig. 1.3 for an example of the trench structure) than on the bottom corners. The deposited molecules eventually fuse from the top two corners of the trench and close the gap. Consequently, the trench structure

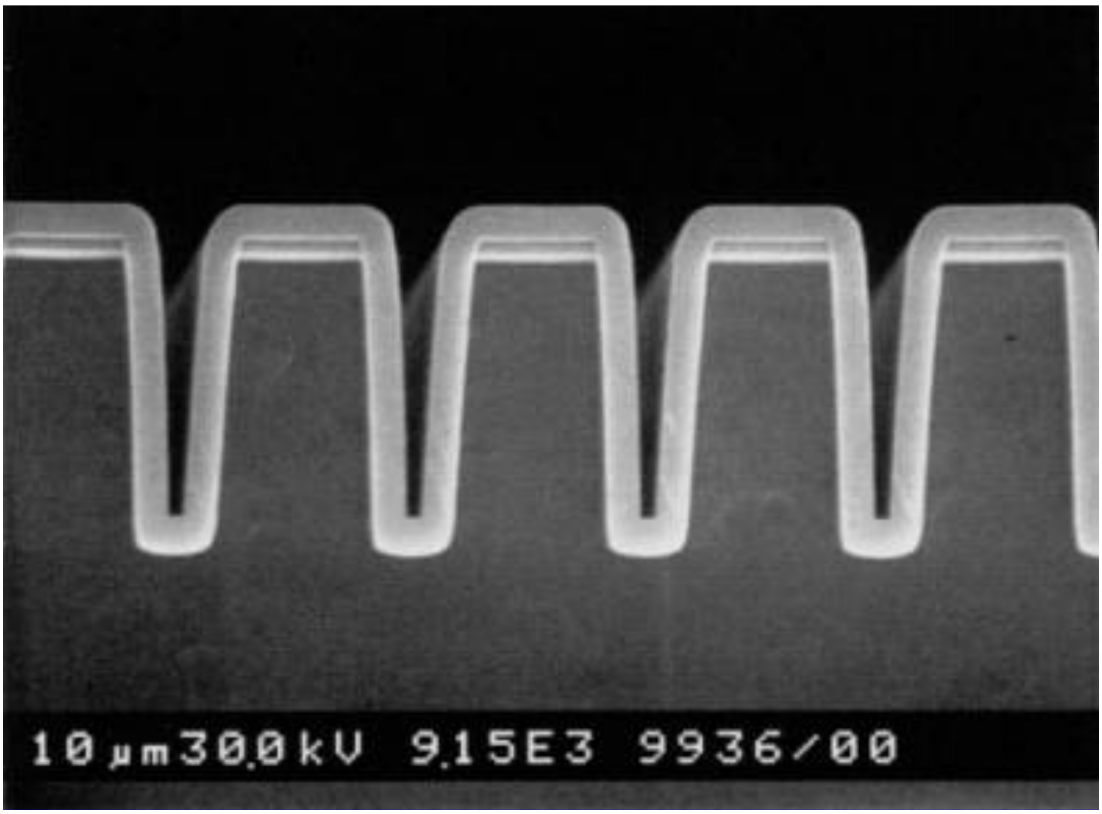

Figure 1.3: Cross-sectional SEM image of an Al_2O_3 film with a thickness of 300 nm on a Si wafer with a trench structure using ALD technique. (Reprinted with permission from ref.[62] Copyright 1999 John Wiley & Sons.)

is lost. The CVD technique fails to deposit a uniform thin film only on the epitaxial surface. As modern electronics shrunk in size, the need for smaller integrated circuits (ICs) pushed the thickness to a new standard, thus a better deposition technique became necessary.[7,61,63–65]

A more adequate layer deposition technique for nano-scale substrates

ALD has become one of the essential techniques for depositing a uniform ultra-thin film on a substrate because of the qualities of the thin film: uniformity, homogeneity, pinhole-free and (atomic) molecular thickness. The deposition technique was first demonstrated in 1977,[66] and the technique has been improved through the early 1990s.[64,67–69] However, the technique was less used commercially due to its slow de-

position rate. Not until the mid-1990s did the technique gain attention again because of the miniaturization of modern electronics, where ALD holds a promise to satisfy all the requirements of a desired thin-film.[7,64,70]

Alkylsilanes on silicon/silicon oxide surfaces

The application of the alkylsilanes on an oxide surface is heavily implemented in the semiconductor industry for decades. By depositing various kinds of materials layer by layer sequentially, numerous ICs are fabricated with different functions.[5,7,42,63,71] The invention of ICs benefits most modern electronics. One of the current directions of research and development is to search for some better candidate adsorbates for maximizing deposition efficiency in terms of energy, time and cost.[5,7,15]

1.3 Interaction on the interfacial layer

The formation of a uniform well-ordered monolayer involves the interplay of the molecule-surface and the intermolecular interactions. A relatively strong adsorbate-surface interaction guarantees the stability of the monolayer-substrate complex, and the intermolecular interaction results in a well-ordered pattern of the monolayer. Here, investigating the adsorbate-surface interaction on the interfacial layer of a monolayer-surface complexes was our primary focus, and this dissertation is formatted in the following two-fold fashion:

1. Sulfur-containing amino acids on gold surfaces

2. Atomic layer deposition of silicon precursors on a silicon oxide surface

1.4 Sulfur-containing amino acids on gold surfaces

The sulfur-containing amino acids cysteine, homocysteine and methionine are a large piece of the biomolecule/metal puzzle, as frequently they serve as the surface anchoring residues of proteins and peptides.[25,54,72] Simulating small proteins, peptides and amino acid multimers on a surface using quantum methods is impractical because of the limitation of the current computational resources and other issues. Narrowing down the complexity and the numbers of molecules of the simulating systems to a feasible size, only the amino acid monomers and dimers are studied in this investigation.[6,11,73] This simplification not only eases the computational resources required but also allows us to study the fundamental interactions of the monomers and dimers on the surfaces: molecule-surface and intermolecular interactions.

1.4.1 The correlation of the binding site reactivities and their coordination numbers

Much of the experimental and computational work on amino acids-metal complexes considered the low-Miller-index gold surfaces,[19,25,49,52–55] though recent work on naturally chiral surfaces and nanoparticles has shown the importance of considering the effects of the adsorption site coordination and the identity of vicinal atoms on the adsorption process.[74–80] The coordination number (CN) of an atom on a surface associating with binding event means the numbers of neighbouring atoms around the binding site. For an ideal Au(111) surface, a surface gold atom has notation CN(9); there are six neighbours on the same layer and three at the layer below. Based on this definition, the low-Miller-index surfaces have higher coordination numbers. The ideal [(111), (100), (110)] gold surfaces are often considered in simulations, due to the reason of high annealing temperatures experimentally, and surface reconstruction, a

well-known experimental fact, can alter the surface topology.[81,82] A still outstanding issue is the change in amino acid or peptide binding behaviour upon adsorption on non-ideal surfaces, (i.e., substrates with adatoms, high-Miller-index facets or surface curvature have been examined individually).[3,19,21,43,44,83–85] In our previous study, the reconstructed Au(110)-(1×2) surface shown in Fig. 1.4 presents three different binding sites: ridges, flats and troughs with CN(7, 9, 11) respectively. The structural binding behaviour and stereospecificity in adsorbed phases obtained in the deposition of cysteine on the reconstructed surface are particularly complex. The binding strengths of cysteine dimer on the three distinct binding sites also shows the preference for where

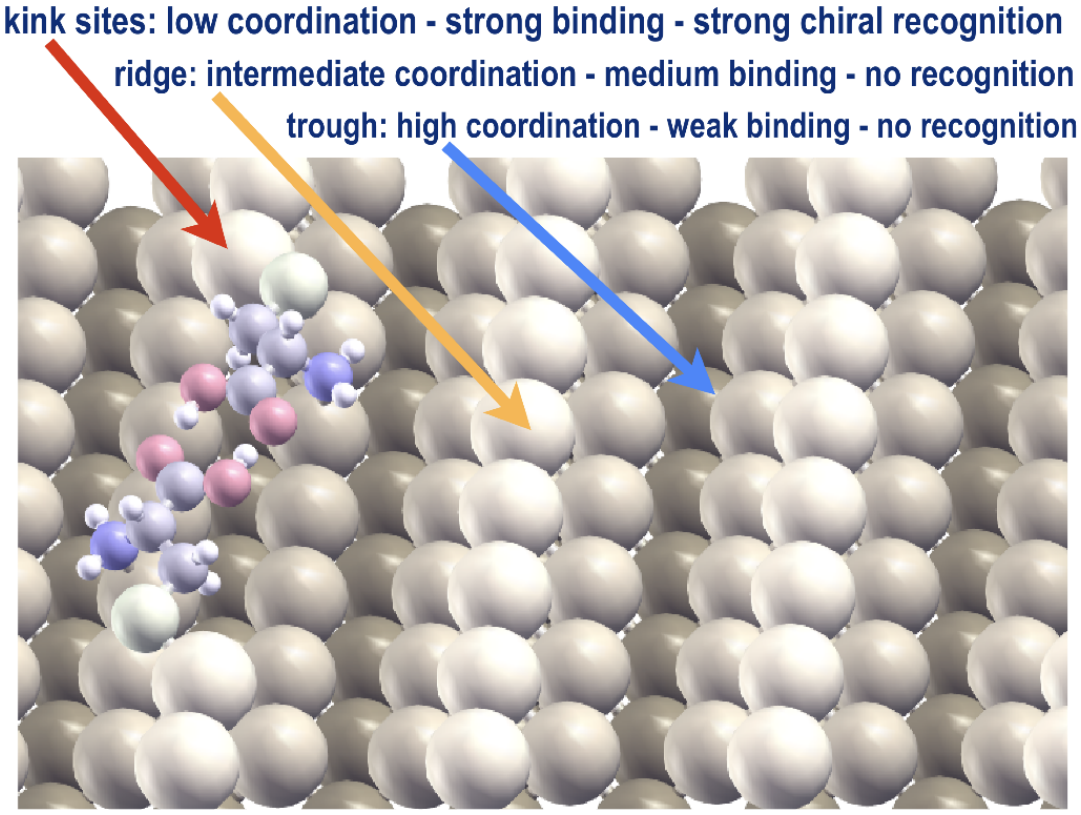

Figure 1.4: The *L*-cysteine dimer structure at the four-atom vacancy reconstructed Au(110)-(1×2) gold surface (proposed by Kühnle *et al.*, *Nature* **2002**, *415*, 891). The surface consists with three binding sites: kink, ridge and trough binding sites. The *L*-cysteine dimer structure shows strong chiral recognition on the kink binding sites but not on the ridge and trough binding sites. The surface facets not only affect the binding reactivities of a site but also the overall configurations of dimer structures.

the binding event occurs.[60] Despite a series of theoretical calculations, ranging from single molecule on a surface to peptide on a surface binding behaviour,[51,86–95] no rigorous studies of the dependence of surface binding on site reactivity or coordination have so far been done for amino acids.

Thus, we focus on the study of site reactivities and CNs. The stronger binding reactivity of the unsaturated metal atoms to adsorbates has been long established in the literature, particularly as a result of nanoparticle studies.[11,83,89,96–105] Several thorough studies by Nørskov and co-workers investigated site coordination effects on the catalytic oxidation on Pt and Au nano-clusters, seeking to elucidate the experimentally observed dependence of catalytic activity on nanoparticle size and shape.[83,98,99] A recent experimental study by Mostafa *et al.*[102] convincingly demonstrated that the catalytic activity of Pt nanoparticles for the oxidation of 2-propanol is positively correlated to not only the average unsaturation of the surface metal atoms, but also to the fraction of edge and kink atoms (i.e., lower coordination number sites). The correlation between the CNs and the binding reactivities is investigated in Chapter 3 using a small gold cluster with various CNs ranging from 3 to 9.

1.4.2 Targeting substrate and adsorbate pairs

Two kinds of substrates - a small gold cluster and a gold surface

Chapter 3 focuses on the study of CNs using a small gold cluster and few small molecules (methyl thiol, dimethyl sulphide and methylamine); however, the binding modes and strengths of the sulfur-containing amino acids can not be appropriately described using the small gold cluster. The cluster is not large enough for the three amino acids. To resolve the substrate size issue, two Au slabs with periodic boundary condition were used to study the binding modes of sulfur-containing amino acids on a Au(111) and an adatom-defect gold surface in Chapter 4.

The adsorbates - chiral amino acids

The adsorption behaviour of chiral amino acids on a gold surface introduces the extra complexity of a true wealth of binding modes. Chirality is ubiquitous on surfaces, as enantiospecific surface patterning can occur by the adsorption of molecules that are chiral, prochiral or even achiral in solution. Achiral molecules may form chiral patterns when deposited and assembled on an achiral surface. The adsorption of chiral amino acids on surfaces provides a fundamental level of understanding for the behaviour of biomolecules in general. The surface also provides complexity in understanding the recognition process, by biasing molecular conformations, binding, and diffusion.[23,27,106–108]

1.4.3 The phenomenon of chiral recognition and separation for racemic mixtures of chiral adsorbates

Changing the patterns of the monolayer by varying the temperatures

The chiral self-assembly of cysteine on gold surfaces has been under intensive investigation with many experimental and theoretical results;[25,45,47–50,55,60,91,109] however, the adsorption behaviours and the formation of the surface periodic 2D patterns are still not well understood at the molecular level. Experimental and computational studies have established the distinct behaviour of sulfur-containing amino acids on various metal facets.[25,51,55,110] In 2002, Kühnle *et al.* published results for deposition of racemic mixtures of cysteine on a reconstructed Au(110) surface. Experimentally, upon annealing to 270 K, small, uniform and highly stereospecific nano-clusters of cysteine are observed on the surface, even when racemic mixtures of cysteine are deposited in low-surface-coverage and low-temperature ultra-high vacuum (UHV) conditions.[25,46,55,60] When the annealing temperature rises to 340 K, a phase transition

occurs, and a new phase of homochiral dimers is observed.[25,45,46] The reorganization of the nano-clusters is accompanied by the surface reconstruction at these temperatures, and the presence of the adsorbate molecules. The surface gold atoms which neighbour the binding sites along the top row ridge diffuse to other sites on the surface, and the reconstructed Au(110) ridge facet turns into a lower coordination number kink facet. As a result, the binding strength between the adsorbates and the kink sites is enhanced and appears to be chemically bound. As the surface coverage is increased at higher annealing temperatures, the cysteine islands reorganize into a well-ordered double-row structure, and the formation of this new surface structure has been explained as due to the presence of the kink sites.[25]

Chiral recognition due to the chiral nature and the surface topology - on kink binding sites

Chiral recognition during a surface deposition process leads to the possibility of separation of racemic mixtures that do not undergo chiral separation at crystallization. Computationally, a significant fraction of thiol molecules do not bind covalently to the substrate at room temperature on the highly-coordinated Au(111) surface with CN(9). On the other hand, system-wide chemisorption is observed on the reconstructed Au(110)-(1×2) surfaces in similar conditions.[25,110] From our previous study, the dimer configurations of *L*-cysteine depend heavily on the local surface facets. Fig. 1.4 illustrates three different surface facets: kink, ridge and trough binding sites with ascending coordination numbers. The facets not only affect the binding strengths of the *L*-cysteine on the gold surface but also the dimer configurations of *L*-cysteine. The chiral recognition of the dimer only occurs on the kink binding sites with CN(6).[60] Apart from the ridge, trough and kink facets that appear on the reconstructed Au(110) surface, the Au(111) surface with a single adatom has also

attracted much attention.[10,21,23] Our own results on sulfur-containing amino acids on ideal and adatom-defect gold surfaces are discussed in Chapter 4.

The formation of zwitterionic form due to the surface coverages

The Au(111) surface is known to undergo surface reconstruction with a $(22 \times \sqrt{3})$ herringbone patterns.[111,112] However, adsorption behaviour on the reconstructed surface is computationally challenging due to the large size of the unit cell.[113–115] The binding modes of cysteine and homocysteine on this realistic Au(111) surface can, therefore, vary slightly due to the non-uniform surface reactivities.[115] The substrate facet also appears to impact the molecular charging state with repercussions over the nature and extent of hydrogen bonding. Experimental work is inconclusive, though it appears that cysteine and homocysteine adsorb in a mixture of nonionic and zwitterionic forms on Au(111), despite UHV conditions.[60,91,116] The general consensus is that cysteine chemisorbs in the nonionic and zwitterionic forms on the Au(110) surface at low and high surface coverages respectively.[25,46,60,90,92,117] Self-assembled conformations depend strongly on substrate geometries and local facets due to the interplay of molecule-surface and molecule-molecule interactions. The combination of the reactive kink binding sites and the missing gold atom vacancy in Fig. 1.4 stabilize the deprotonated thiol group and the protonated amine group respectively. A stable zwitterionic form of the *L*-cysteine dimer only appears at kink binding sites.[25,60]

The formation of zwitterionic form due to the temperatures

Experimental work by Ataman *et al.* showed the formation of *L*-cysteine thick film (greater than 40 Å) on a TiO_2(110) substrate under various temperatures and UHV condition.[118] X-ray photoelectron spectroscopy (XPS) analysis showed that the zwitterionic *L*-cysteine film has protonated amino groups and largely deprotonated thiol

groups at low temperature (100 K). The deprotonation switched from the thiol group to the carboxylic group when the film is formed at over 200 K. The carboxylic groups are completely deprotonated at the higher temperature.[118–122] Cossaro *et al.* had demonstrated the fabrication of the thin film of the zwitterionic state of cysteamine (which is a cysteine without the carboxylic group) on an Au(111) surface under the UHV condition at low temperature.[121] However, the proton transfer events of cysteines on an adatom-defect gold surface have not yet been examined computationally. In Chapter 4, we investigate the zwitterionic *L*-cysteine and *L*-homocysteine on a Au(111) surface and on an adatom-defect surface.

1.5 Chemical deposition of silicon precursors on an ideal SiO_2 surface using ALD

The objective of the second topic of this work is to integrate computational simulation models with experimental results for depositing silicon and oxidant precursors on a silicon oxide substrate. The ALD schematic in Fig. 1.5 shows how a thin film is achieved by sequentially depositing two kinds of precursors.

1.5.1 High-temperature ALD

Fabricating a molecular-thickness layer with uniformity, homogeneity, pinhole-free quality in a self-limiting fashion

In ALD, a chemical reaction occurs in self-limiting fashion because there are only a finite number of reactive binding sites on the epitaxial layer for the precursors in the first half-cycle. Once the (red) precursors in Fig. 1.5 (a) to (b) occupy and react with all the binding sites on the surface, the deposition finishes. A monolayer

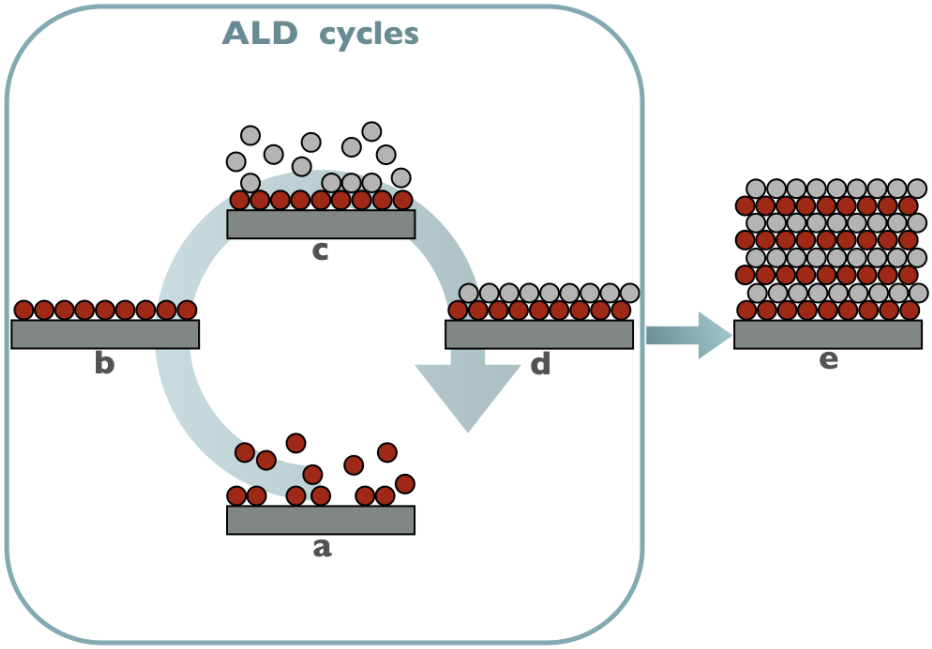

Figure 1.5: Schematic representation of ALD in self-limiting and sequential fashion. a) The precursors in red are deposited onto the surface. b) Due to the self-limiting nature of ALD, a monolayer of red precursors is formed. c) The precursors in grey are then deposited onto the monolayer of the red precursors in a sequential fashion. d) A monolayer of grey precursors is formed. e) The deposition stops when the thickness of the thin film reaches the request. The self-limiting and sequential fashion of ALD guarantees the thickness of the thin film with atomic level control and precision.

is formed with uniformity, homogeneity and pinhole-free. The self-limiting fashion guarantees not only the thickness of a monolayer of one kind of precursor but also the quality of the monolayer with (atomic) molecular-level of control. Purge is then applied as in Fig. 1.5 (b) to remove the byproducts that do not react with the surface but weakly interact with the monolayer of the precursors. The second precursors are then deposited onto the monolayer-surface complex in the second half-cycle shown in Fig. 1.5 (c). The overall thickness of the film depends on the number of reaction cycles.[7,70,123–125]

The current method of growing a silicon oxide/nitride thin layer is to deposit silicon precursors on a substrate under high temperature around 400 °C. This tem-

perature guarantees the quality of the thin layer which is a uniform, pinholeless monolayer coating on the substrate. Lowering the deposition temperature worsens the quality of the thin film. Insufficient kinetic energy results in lower chemical reaction rates between the precursors and the surface. Only a small portion of precursors have sufficient amount of kinetic energy to overcome the potential energy barrier and form products. However, low temperature ALD has a couple advantages. What if one wants to coat a thin film of silicon oxide/nitride on top of a bio-substrate or a piece of plastic (polymer), etc. for wearable devices? High temperature in a deposition chamber can destroy these thermal-fragile materials easily. To achieve lower temperature deposition, some modifications are needed for the deposition process. Our approach is to seek to increase the reactivity of a precursor so that it reacts with the surface fast and with lower thermal energy. The modifications should satisfy the following criteria:

- a precursor has relatively high stability on the silicon oxide/nitride substrate
- an exothermic chemical reaction is preferred
- a chemical reaction with lower activation energy is preferred
- the byproduct of the chemical reaction should be easily removable from the thin-layer-substrate complex

The ALD reactions on SiO_2 substrate without catalyst are usually very slow and require high temperatures and large precursor fluxes.[126] The classic precursor for silicon is $SiCl_4$. Unfortunately, the use of the halide results in the corrosive product HCl which can contaminate the monolayer. In addition, the HCl can react with most amine catalysts to form chloride salts that can lead to film contamination.[7,127]

The vaporization temperature and the deposition temperature

Temperature is one crucial factor which affects the quality of a thin film during the deposition process. The deposition temperature depends on materials, precursors and substrates. During the entire deposition process, two temperature settings are important: the temperature that allows the precursors to vaporize or sublimate, and the temperature to start the chemical reaction between the precursors and the substrate. In general, a higher temperature within the operating range in the deposition chamber produces a better quality thin film in terms of the conformity, homogeneity and pinhole-free quality.[7,14,64,65,67] For example, a typical operating temperature for depositing SiO_2 film using $SiCl_4$ and H_2O as the precursors ranges from 500 to 800 °C.[7,125,128–130] The drawbacks of this original recipe for fabricating a SiO_2 film include requiring large reactant pressures (about 1.3 atm) and producing the corrosive byproduct HCl.[129] The high temperature during the deposition is problematic when the desorption rate becomes significantly large, the precursors decompose, or the substrate is thermally fragile (such as polymers, plastic and biological samples).[7,129,131,132] The necessity of low-temperature deposition is obvious for fabricating thermally fragile electronic devices.[7] One solution is to introduce catalysts in the deposition reactions. Low-temperature catalytic ALD started getting much attention since the early 2000s (2004 and 2005).[129,131]

1.5.2 Catalytic silicon precursors for lower temperature ALD

Lowering the activation energy by introducing catalysts to the deposition

The activation energy ΔE_a is the amount of energy required to bring precursors to the SiO_2 surface in proximity and rearrange the precursors into some particular configurations for a chemical reaction to take place. During the transition state, the

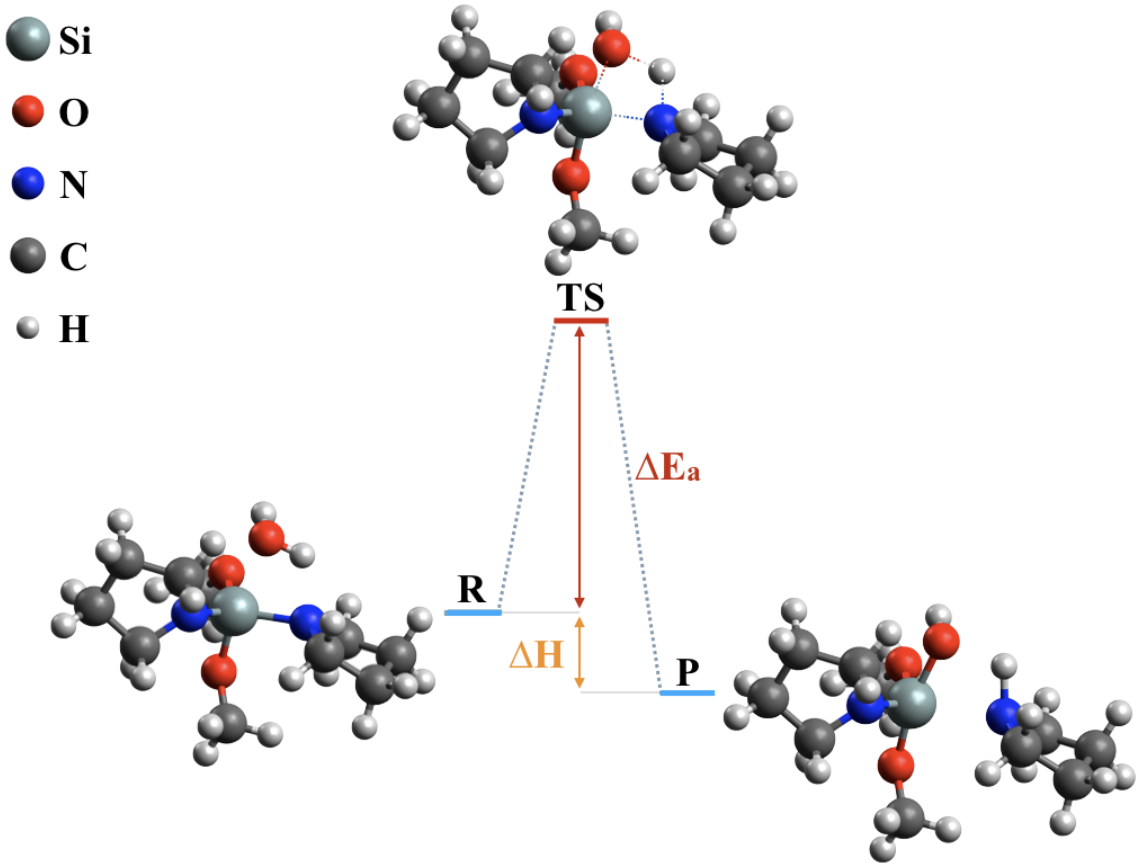

Figure 1.6: The chemical reaction of the precursor (Di(pyrrolidinyl)dimethoxysilane) and a water molecule at the transition state (TS) via a four-membered ring reaction mechanism. The activation energy (ΔE_a) is the energy that rearranges the reactants (R) in to some particular configurations for a chemical reaction to take place at the TS. The energy difference between the reactants (R) and the products (P) is the reaction enthalpy (ΔH). At the TS, the Si-N and the O-H bonds undergo deformation while the Si–O and the N–H bonds undergo formation simultaneously.

formation and deformation of bonds happen simultaneously as shown in Fig. 1.6. Since our goal is to achieve lower temperature deposition, the necessity of lowering activation energy is unquestionable. Catalytic ALD provides a solution to achieve low-temperature ALD. For example, depositing a SiO_2 film by $SiCl_4$ (silicon source) and H_2O (oxygen source) requires the deposition temperature to be more than 500 °C with a substantial partial pressure of the reactants. By introducing pyridine (or ammonia) as the catalyst in the deposition process, the catalytic ALD can occur near to room

temperature with significantly less partial pressure of the precursors.[7,128,129,131] In general, the binding strength of a catalyst on a substrate depends on two competing factors, the pK_a value and the steric hindrance of the catalyst. The binding strength increases with the pK_a value while the catalyst decreases with the physical size.[130] The temperature reduction comes with the price of producing inferior SiO_2 films compared with the thermal SiO_2 film.[7]

The silicon precursors with catalytic Lewis bases as ligand

Catalytic ALD is not problem free. A successful catalytic ALD reaction requires three species: the precursor, the catalyst and the binding site of the substrate to be in proximity for the chemical reaction to take place.[7,128,131,133] The presence of catalysts introduce an alternative reaction pathway with lower activation energy barriers which provide a solution of lower temperature deposition. One of the limitations is that most Lewis base catalysts leave the surface at temperature ranges which are notably lower than the temperature to produce a quality film.[130] Based on the experimental observations from Du *et al.*, the growth rate of the catalyzed SiO_2 ALD drops significantly at higher temperatures, and the decreasing rate is correlated to the lower surface coverage of the catalyst.[131] Thus, a higher partial pressure of the catalyst is needed for low-temperature catalytic ALD.[7,130] Another limitation is that the byproduct of the reaction can accumulate on the epitaxial layer. The byproduct (salt) is formed from a cation and an anion that attract by Coulombic force. For example, when ammonia (NH_3) is introduced to the classic SiO_2 deposition which is fabricated by $SiCl_4$ and H_2O, the byproduct salt is NH_4Cl as shown in the silicon

precursor half-reaction equations (1.1).[7,128,131,133,134]

$$\begin{aligned} \mathrm{SiOH^* + NH_3 \rightarrow SiO^{*-} + NH_4^+} \\ \mathrm{SiO^{*-} + SiCl_4 \rightarrow SiOSiCl_3^* + Cl^-} \\ \mathrm{Cl^- + NH_4^+ \rightarrow NH_4Cl} \\ \mathrm{Cl^- + NH_4^+ \rightarrow HCl + NH_3} \end{aligned} \tag{1.1}$$

where the asterisks denote the surface species. The accumulation of the salt (NH_4Cl) trapped on the surface can physically block the surface reaction of the precursors and the epitaxial layer. Although the byproduct eventually desorbs from the surface by reducing the vapour pressure of the salt, a longer deposition time per deposition cycle is required. If the time is insufficient, then poor quality film is fabricated.[7] An elegant solution is to attach a catalytic Lewis base ligand to the silicon precursor - a self-catalyzing silicon precursor. This way solves the issues of keeping catalytic Lewis base at the surface at a higher temperature and reducing a three-body (surface, Si precursor and catalyst) chemical reaction to a two-body (surface and self-catalyzing Si precursor). In this dissertation, some selected self-catalying silicon precursors were studied, and we focused on investigating the binding strengths of the precursors with a SiO_2 surface, and their theoretical activation energies.

1.5.3 Establishing a predictable model

The final goal of this industrial collaboration is to search for some potential catalytic precursors for low-temperature silicon nitride deposition by using computational simulation as the tool. Our initial short term goal is to integrate the known experimental results that are provided by Seastar Chemicals Inc. company with proper theoretical models, efficient computational methods and optimized simulation parameters.

Since the company had the results of depositing a silicon oxide film by using various catalytic (Lewis base ligand derivative) silicon precursors, the results such as the deposition rates, solution phase reaction rates, thermal stabilities and pK_a values were used to verify the simulation results and optimize the parameters.

Determining the most likely reaction pathway(s) by considering the reaction enthalpies and activation energies

Combining the experimental and simulation results, we have a more complete picture and a better understanding of the deposition process in terms of the molecular configurations, the binding modes, the reaction enthalpy, activation energy and charge distribution. The reaction enthalpy relates to reactivity and selectivity of a precursor. The activation energy relates to the most likely chemical reaction mechanism and the reaction rate. The combination of the reaction enthalpy and the activation energy can predict if a byproduct of a chemical reaction is going to be a competing reaction. The combination of the temperature, the binding energy and the molecular configuration can show a similar trend as the pK_a value of a catalyst.[130]

Tuning the simulation parameters and models for fast calculations

The experimental results also help verifying if the simulation parameters are optimal for a set of molecules. The parameters include the choice of modelling methods, functionals, basis set sizes, etc. Because ALD is a surface process, a proper way of simulating the deposition process is to consider the substrate as a surface with periodic boundary condition (discuss in Chapter 2). However, the accuracy comes with a price: resources. The resources include: the usage of CPUs, memories, disk sizes and computing time. In order to satisfy the fast-paced research schedule, many modifications and simplifications are applied to reduce the usage of the resources

especially the computing time.

1.6 The objectives of my studies

My objectives were: **a)** to investigate the correlation of binding strength on various local structures (geometries) of substrates which can be a surface or a cluster, **b)** to perform molecular dynamics simulation in the quantum level with reasonable computing resources and to contain efficient accuracy for meaningful analysis, and **c)** to integrate the theoretical knowledge, computational predictions and known experimental results and to better search the candidate precursors for ALD.

1.7 Outline

This dissertation has the following structure:

Chapter 1 provides background information for motivation and states the questions and challenges for us to tackle, understand and possibly to answer in the later chapters.

Chapter 2 provides the computational methods, method corrections and simulation models, and the reasons for using quantum theory and wavefunction approach rather than using classical molecular dynamics methods. Some terminologies of computational chemistry (such as DFT, functionals, basis set, etc.) are introduced and clarified.

Chapter 3 investigates how coordination numbers, facets and local geometries affect the binding strengths, binding modes and the configurations of the complexes. The selected substrate is a Au_{20} cluster, and the adsorbates are: methyl thiol, dimethyl sulphide and methylamine. They are associating with the binding events on a gold substrate via chemisorption or physisorption.

Chapter 4 focuses on the actual sulfur-containing amino acids, cysteine, homocysteine and methionine on gold surfaces. The amino acid monomers on a gold surface is to study the molecule-surface interactions that involve the binding events of the sulfur-gold and amino-gold. The binding energies, binding modes and configurations are discussed. The intermolecular interactions are investigated the dimer forms of the amino acids on a gold surface. For cysteine and homocysteine, the zwitterionic forms are also considered in the study.

Chapter 5 presents the work with industrial partner, Seastar Chemicals Inc. company. The goal is to establish a predictable model that supports experimental surface deposition and hydrolysis results. Surface calculations are performed to study the steric hindrances, binding strengths and binding modes of precursors. Reaction enthalpies and activation energies are computed for various catalytic silicon precursors using the simulation program, Gaussian 09. The procedure of considering the reaction enthalpies and the activation energies as a whole extends to the deposition of a silicon nitride surface.

Chapter 6 concludes the results on the sulfur-containing amino acids and adsorbates on gold substrates, and on the energy profiles, conformational evolution and stable configurations of selected self-catalying silicon precursors.

Chapter 2

Methodology

2.1 Introduction

Depending on the size and complexity of a large system (e.g., solvated protein, multimers on a surface, etc.), classical molecular dynamics (MD) is capable of handling, with computational efficiency, some thousands of molecules for simulation times up to the microsecond scale. In terms of simulation results, most physical properties including: binding strengths, intermolecular interactions, binding conformations and phase transitions can be approximately described by a well-constructed and parametrized force field for a particular system.[35,39,56–58,135–137] Therefore, classical MD simulation is naturally the method of choice to study multimer systems of various amino acids (cysteine, homocysteine and methionine) on a gold surface. However, classical MD simulation has three limitations:

1. Because a force field is generally designed and parameterized using experimental data[35,56,135] or higher level theory results such as density-functional theory (DFT) results[57,58,135] for some particular systems, transferability of a force field is often low. The accuracy of describing the physics of the simulated systems

may be off to a significant degree, if a particular force field is used to simulate some other systems.[35]

2. Classical simulations cannot easily describe bond breaking and forming. In the simulation, the bonds of a molecule are usually modelled by harmonic oscillators with some pairwise force (spring) constants, and thus a molecule is treated as an unbreakable entity.[35,39,57,58,135] In recent years, chemical reaction-capable force field, ReaxFF, has been developed to overcome this limitation and is able to deal with chemical reactions with sufficient training set of data (i.e., bond lengths, bond angles, reaction enthalpies, activation energies, etc.).[138–142]

3. Many classical simulations use a Lennard-Jones potential to describe a surface.[57,135,136] This model tends to maximize the numbers of neighbours around an almost saturated atom rather than to stabilize an atom which has fewer neighbours and is chemically more reactive (e.g., an adatom on the surface).[60] The latter binding mode is confirmed in both nanoparticle experiments[83,98,99,143] and quantum simulations.[60,144] For simulating surface chemistry, the disagreement of binding location arises when the surface has various distinct binding sites.

Whereas widely specialized force fields may be developed to limit the effect of the first limitation, the second limitation can be a fundamental issue in systems involving chemical reactions. For example, the experimental results indicate that cysteine and homocysteine adsorb on the Au(111) surface in a mixture of nonionic and zwitterionic forms (-NH_3^+ and -COO^-) as shown in Fig. 2.1, even in UHV conditions.[25,55,91,116] For the alkanethiol SAMs on a gold surface, the fate of the hydrogen of the thiol group remains a mystery.[9,44,145] A conventional assumption is that the hydrogen gas leaves the system during the formation of the monolayer (see Fig. 2.2).[10,146–156]

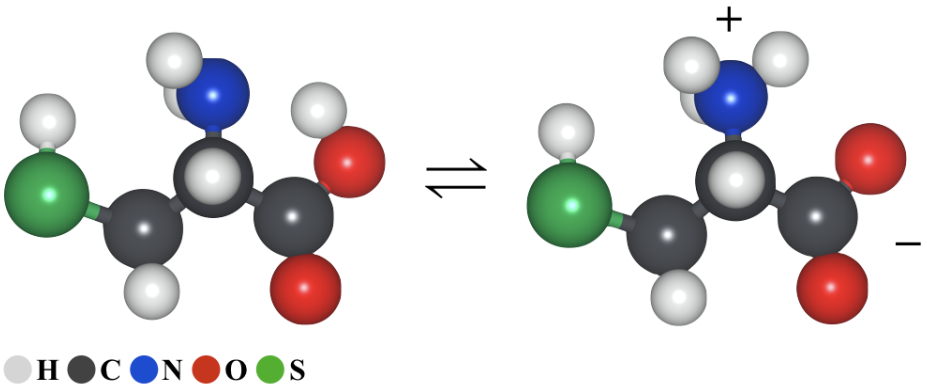

Figure 2.1: The zwitterionic (on the right) cysteine is formed from the nonionic cysteine (on the left) when the proton on the carboxylic acid group (-COOH) transfers to the amino group ($-NH_2$). The formation of the zwitterionic cysteine was proposed to occur under higher surface coverage on Au(111) surface.[90,116,118]

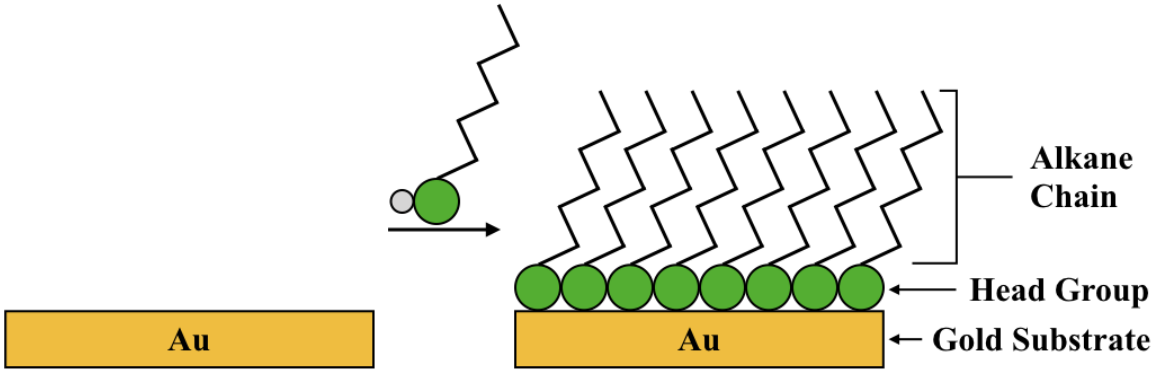

Figure 2.2: Schematic diagram of preparation of alkanethiolates SAM on a Au(111) substrate. The head group here is thiol/thiolate functional group.

Although the experimental work is still inconclusive, the proton transfer can be studied computationally with a proper method. Whereas classical MD may not able to follow these reactions computationally, quantum simulations hold real promise in modelling the formation of zwitterion of cysteine and homocysteine and the deprotonation of alkanethiol to alkanethiolate on a gold surface.[92,118,157–159]

Similar reasoning applies to the second area of emphasis in the current work: silicon oxide/nitride surface fabrication via ALD. Fig. 2.3 illustrates the incoming silicon precursor ($SiCl_4$) chemically reacts with the surface hydroxyl group (-OH) via a four-

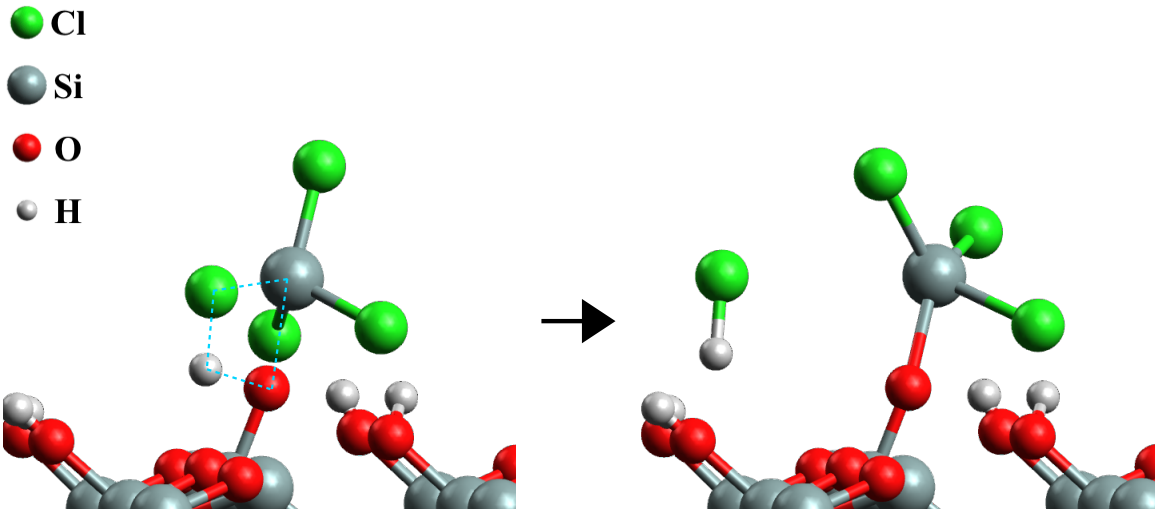

Figure 2.3: Schematic diagram of the silicon cycle using silicon tetrachloride as the precursor on a silicon oxide (SiO_2) surface. The silicon precursor and the hydroxyl group (Si-OH) on the surface form a four-membered ring. After the chemical reaction, the precursor binds to the silicon oxide surface, and HCl is the byproduct.

membered ring mechanism. After the reaction, the product (the precursor-surface complex) and the byproduct (HCl) are formed.[7,123,128,134] In order to adequately model the reaction mechanism of the ALD process and account for the electronic exchange driving the reaction, a quantum level method such as *ab initio* molecular dynamics (AIMD) is necessary.[7,126,130,134,160–162]

The challenges of classical MD with consideration of site reactivity (the third limitation) were discussed in a previous Paci group publication.[60] In that work, classical MD simulations identified the trough (shown in Fig. 2.4 (a)) as the binding site of the cysteine on the Au(110)-(1×2) surface. However, DFT optimizations showed stronger binding at the ridge sites,[60] (see Fig. 2.4 (b)) as also reported experimentally.[25,45,46,48,50,109] The two simulation methods produced vastly different binding configurations. The classical LJ potential tends to maximize the number of nearest neighbours, thus indicating the high coordination number sites as the most reactive. This is inconsistent with our own quantum calculations and literature regarding

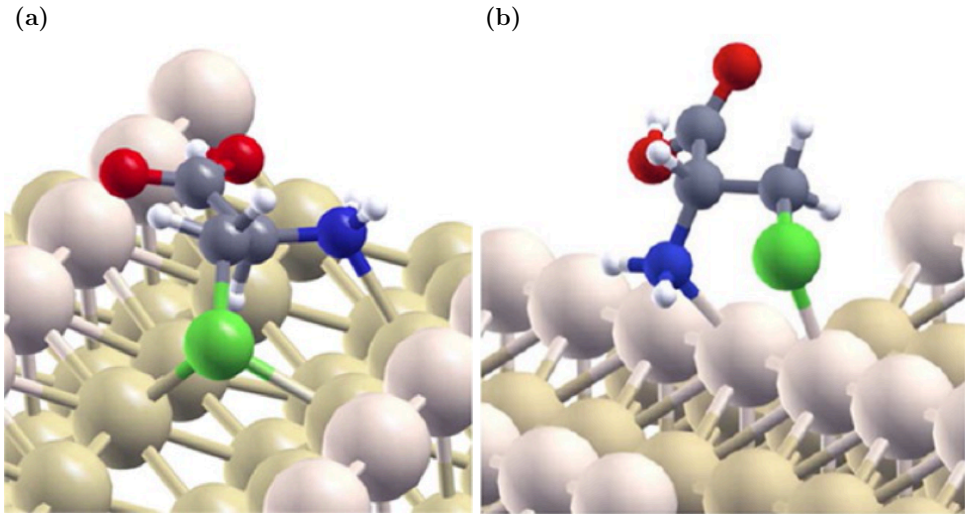

Figure 2.4: Optimized configurations using (a) classical MD sampling and (b) DFT optimization.[60]

nanoparticle reactivity.[10,102,143,144,163–166] While force field calculations are blind to site-specific reactivity, they are sufficient for Au(111) surface, where all the surface gold atoms are physically, chemically and reactively equivalent.

A quantum method is required to appropriately and adequately describe conformational changes of amino acids on a complex gold surface and chemical reactions of silicon precursors on a silicon oxide surface, so some of the basic aspects of DFT are discussed in the following sections and subsections:

- Density-Functional Method Approach
  - The total energy equations
  - Geometry optimization
  - Pseudo-atomic orbital basis set
  - Periodic boundary conditions
  - The binding energy equations

- Improvement and Corrections
    - Basis set superposition error and Couterpoise correction
    - Energy shift and orbital cutoffs
    - Van der Waals corrections
- Limitations of DFT method
- Conclusions

2.2 Density-functional method approach

DFT is arguably the most popular and widely used for modelling a relatively large and complex system with reasonable computing resources.[10,25,43,45,47,51,60,96,112–115,117,144,165–170] The computational cost of DFT method is relatively inexpensive comparing to the post-Hartree-Fock methods such as Møller-Plesset perturbation theory, configuration interaction and coupled cluster.[52,88,119,168,171]

According to the Born-Oppenheimer approximation, the total wavefunction can be separated into the nuclear and electronic wavefunctions. Ideally, both nuclear and electronic wavefunctions should be determined using quantum mechanical treatments. However, treating the nuclei quantum mechanically increases computational resources substantially. Computationally, further simplifications are made based on the proton-to-electron mass ratio which is 1836.15, and their motions that proton and other heavier nuclei move much slower than electrons. The wave property of nuclei also becomes less significant as mass increases, and thus the much heavier nuclei can be considered classical point particles. Consequently, treating the motion of the nuclei classically is a reasonable approximation.[172] In simulation, each of electrons in a system is subjected to a total potential from the fixed nuclei and other elec-

trons. At each snapshot, the total energy of the system is a function of the states of electrons and the positions of the nuclei. The majority of electronic calculations in this dissertation were performed using the SIESTA (Spanish Initiative for Electronic Simulations with Thousands of Atoms) 3.2 and 4.0 packages.[87,173] SIESTA is not only a program but also a method to compute electronic structure calculations efficiently by using the localized finite-range pseudo-atomic orbital basis set in a 3D real-space grid. For a system with N electrons, this approach turns a N^3-scaling DFT to an almost linear-scaling DFT, and is more suitable for modelling a relatively large system.[87,173–177] Electron wavefunctions are solved using the Kohn-Sham formalism[178] of density-functional theory (KS-DFT) in a self-consistent field (SCF) approach, shown in Fig. 2.6. In the simulation, since the nuclei are treated classically while the electrons are treated quantum mechanically, one drawback of this simplificaiton is that proton tunnelling is forbidden in the simulation.

2.2.1 The total energy equations

The general form of the total electronic energy in the KS formalism is expressed as:[179,180]

$$E_{\mathrm{KS,total}} = E_{\mathrm{T}} + E_{\mathrm{V}} + E_{\mathrm{J}} + E_{\mathrm{XC}} \tag{2.1}$$

where T, V, J and XC are the kinetic, potential, Coulombic and exchange-correlation energy terms respectively. The exchange-correlation energy term is solved by some approximations, and some common approximations are local-density approximation (LDA), generalized gradient approximation (GGA), meta-generalized gradient approximation (meta-GGA) and hybrid-generalized gradient approximation (hybrid-GGA). LDA only considers the density while GGA takes both the density and the gradient of the density into account. Meta-GGA takes the density, the gradient of the density and the Laplacian of the density (also called the kinetic energy density) in

the exchange-correlation functional.[168,179,181–183] Hybrid-GGA mixes some portions of exact exchange from Hartree-Fock theory with LDA and/or GGA.[182,184,185] The approximations, LDA, GGA, meta-GGA and hybrid-GGA are also known as the Jacob's Ladder, the first, second, third and fourth ladder respectively shown in Fig. 2.5.[1,168,181,186–190] Some functionals contain empirical parameters (for example,

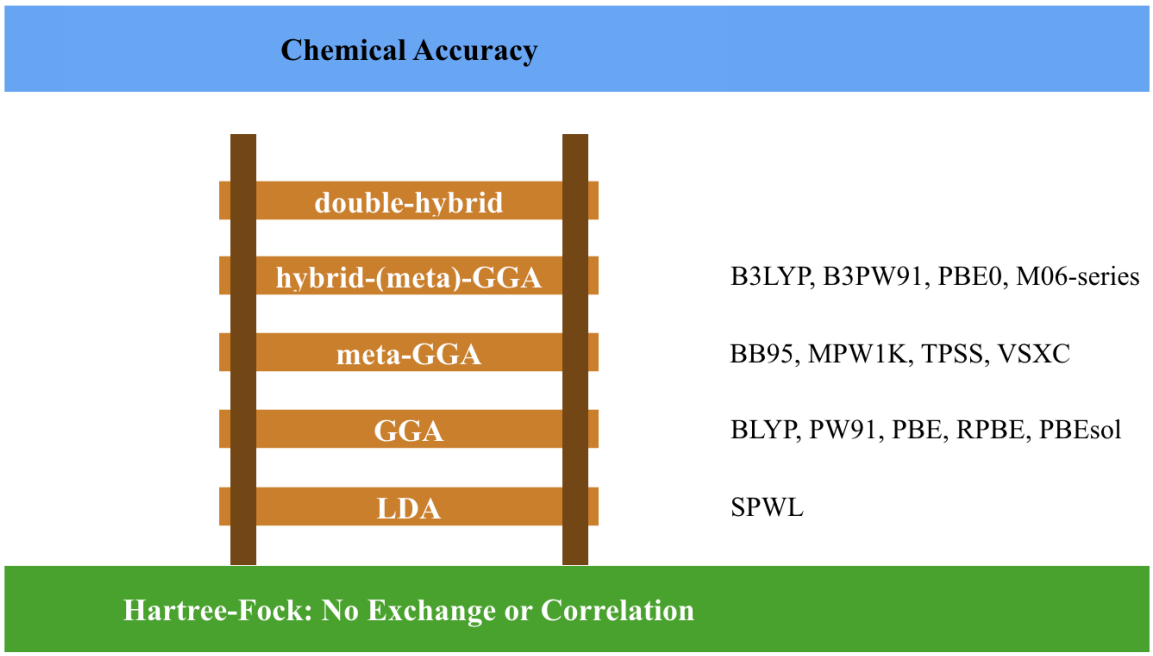

Figure 2.5: J. Perdew's metaphorical Jacob's ladder for the five generations (rungs) of DFT functionals. Theoretically speaking, the accuracy should be improved at a higher rung because it contains new physical content that is not included in lower rungs. Some of the common DFT functionals within each rung are indicated.[186,189,190]

B3LYP functional contains three empirical parameters) in order to fit some experimental or higher level method results. Based on the existence of an empirical parameter, the DFT functionals are divided into two groups:[180,182]

1. *pure* DFT functionals with no empirical parameters

2. *hybrid* DFT functionals with some empirical parameters

Most of the calculations presented here used the SIESTA simulation program with the PBE Hamiltonian, and the total energy is expressed as follows:

$$E_{\mathrm{KS,total}} = E_{\mathrm{ions}} + E_{\mathrm{na}} + DE_{\mathrm{na}} + E_{\mathrm{kin}} + E_{\mathrm{nl}} + DU_{\mathrm{scf}} + E_{\mathrm{xc}} + E_{\mathrm{molmec}} \tag{2.2}$$

where

$$\begin{aligned}
E_{\mathrm{ions}} &= -\sum_{I} U_I^{\mathrm{local}} \\
E_{\mathrm{na}} &= \sum_{I<J} \delta U_{IJ}^{\mathrm{local}}(R_{IJ}) + \frac{1}{2}\sum_{IJ} U_{IJ}^{\mathrm{NA}}(R_{IJ}) \\
DE_{\mathrm{na}} &= \int V^{\mathrm{NA}}(\vec{r})\delta\rho(\vec{r})d\vec{r} \\
E_{\mathrm{kin}} &= \sum_{\mu\nu} T_{\mu\nu}\rho_{\nu\mu} \\
E_{\mathrm{nl}} &= \sum_{\mu\nu} V_{\mu\nu}^{\mathrm{KB}}\rho_{\nu\mu} \\
DU_{\mathrm{scf}} &= \frac{1}{2}\int \delta V_{\mathrm{H}}(\vec{r})\delta\rho(\vec{r})d\vec{r} \\
E_{\mathrm{xc}} &= \int \mathcal{E}_{\mathrm{xc}}[\rho(\vec{r}), \nabla\rho(\vec{r})]d\vec{r}
\end{aligned} \tag{2.3}$$

Here, E_{ions} and E_{na} are the potential energies of single pseudo-atoms I, and the interaction of two pseudo-atoms I, J respectively. DE_{na} and E_{kin} are the electron-nuclear interaction and the kinetic energies. For the other three energy terms, E_{nl}, DU_{scf} and E_{xc} are the potential of electrons, the electron-electron interaction (solved in SCF iterations), and the electronic exchange-correlation (with GGA approximation), respectively. E_{molmec} is the molecular mechanics energy describing the van der Waals interaction empirically using Grimme's approximation (see subsection 2.3.3).[87,173] The electron density ρ is expressed in terms of the density matrix $D_{\mu\nu}$ and the basis func-

tions b_μ:[168,179,185,191–193]

$$\rho = \sum_{\mu\nu} D_{\mu\nu} b_\nu b_\mu \tag{2.4}$$

where $D_{\mu\nu}$ contains the coefficients $c_{\mu i}$ for the basis functions b_μ that construct the ith wavefunction in the linear combination fashion:[179]

$$D_{\mu\nu} = 2 \sum_{i}^{N/2} c_{i\mu} c_{i\nu} \tag{2.5}$$

$$\varphi_i = \sum_{\mu}^{n} c_{\mu i} b_\mu \tag{2.6}$$

2.2.2 Geometry optimization

A relatively stable structural configuration (called simply "configuration" in this dissertation) of a system can be obtained using geometry optimization, and the algorithm is shown in Fig. 2.6. Based on a provided initial configuration, a simulation software builds its potential and the molecular orbitals (MOs). The total energy equation of the electron wavefunction is solved and optimized in the SCF iteration while the nuclei are kept in fixed positions. The potential energy is then updated, and the nuclei relocate to new positions based on the trajectories of the steepest descent of the potential energy gradient. The algorithm continues until the total energy reaches a local minimum, and an optimized configuration is thus obtained. The optimization algorithm highly depends on the potential of the previous configuration (or the initial input configuration), an optimized output configuration may not necessarily be the most stable structure. Usually, many guessed configurations are computed and optimized. The configuration with the lowest total energy amount these optimized configurations is reported herein. An alternative method of obtaining a relatively

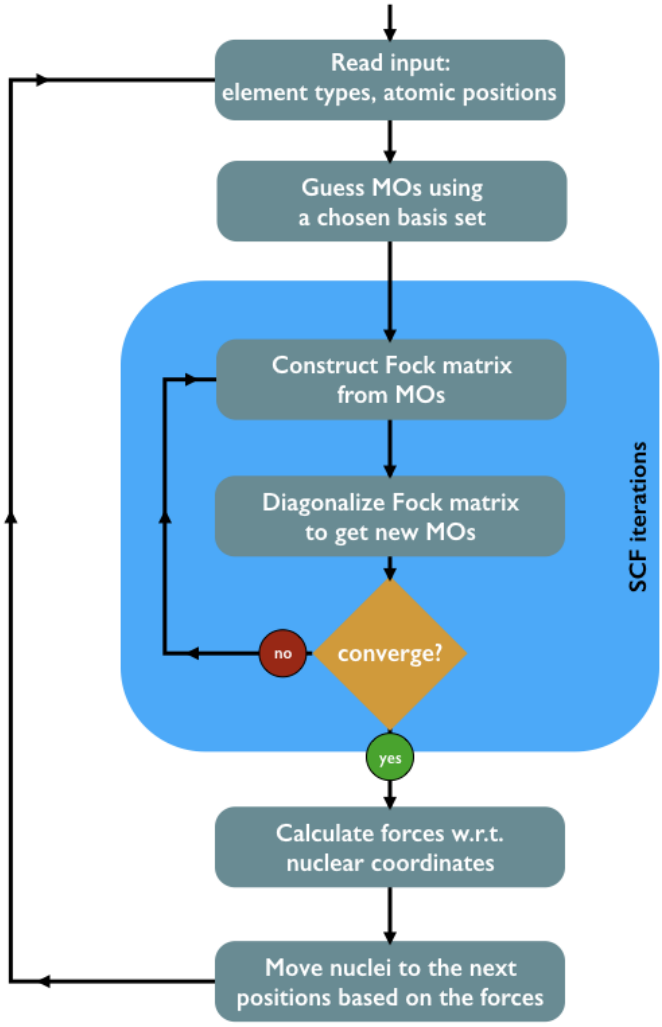

Figure 2.6: Schematic diagram of illustrating the simulation algorithm which can be geometry optimization or molecular dynamics.

stable structure is via AIMD. The simulation follows a similar process, but structural evolution is followed using Newton's equations of motion with inclusion of kinetic energy for the molecules (pseudo-atoms to be more specific) and temperature for the entire system. The consideration of thermal energy (heat) reduces trapping in local minima of the potential energy surface.[180,181]

2.2.3 Pseudo-atomic orbital basis set

SIESTA separates the electrons into two groups: core and valence electrons. The collection of the core electrons and the nucleus is called a pseudo-atom, and valence electrons are described using pseudo-atomic orbital (PAO) basis set.

The pseudo-atoms are numerically parametrized, verified and tabulated in the pseudopotential file in SIESTA. The construction follows the scheme of Troullier and Martins.[194] The pseudopotential files were downloaded from the SIESTA website and tested in the group. For heavy elements (i.e., gold atom), the accuracy of the pseudopotentials can be improved by involving relativistic corrections, but these are not captured in the available pseudopotentials. Further optimization of the pseudopotentials is not in the scope of this study. The strategy of using numerical pseudo-potentials significantly increases the simulation speed in SIESTA. For example, a gold atom consists of 68 electrons in the full-shelled core and 11 valence electrons. The 68 electrons are pre-tabulated in the pseudopotential file, and the computation only needs to compute the 11 valence electrons in the simulation.

Valence electrons are described using PAOs with a polarized triple-ζ (TZP) basis set. Only valence electrons are considered in the self-consistent field (SCF) cycles.[87,173,177] The triple-ζ indicates that the angular momentum is split into three channels based on the split-valence method. In the method, a contracted orbital is described by the first-ζ basis orbitals using a linear combination of Gaussian functions. The fitness of the first-ζ function is determined either variationally or by fitting numerical atomic eigenfunctions. The slowest-decaying orbital is described by the second-ζ basis orbital using one of the Gaussian functions which is split from the contracted orbital. The third-ζ is generated using a similar recipe by splitting more Gaussian functions from the contracted orbital. Polarization is described by one Gaussian function. Further polarization functions were found to have a minimal

effect on total energies and lattice constants.[173] Here, we benchmarked the binding energies of methylthiol- and methylthiolate-Au_{20} complexes using polarized double-ζ (DZP) and TZP basis sets without counterpoise (CP) and van der Waals (vdW) correction shown in Table 2.1 (BE(TZP) vs BE(DZP)), and found that the binding energies differ insignificantly (less than 0.1 eV) regardless of the basis sets and the binding sites. TZP is used for all the calculations using SIESTA according to standard literature usage.[55,60,112,117,144]

Table 2.1: Binding energies of MeSH and MeS–Au_{20} complexes on the binding sites with various neighbours using various simulation settings.

CNs[1]	BE(TZP,CP*,vdW)[2]	BE(TZP,CP)	BE(TZP)	BE(DZP,CP)	BE(DZP)
3	−0.97	−0.82	−0.91	−0.79	−0.84
4	−1.07	−0.79	−0.95	−0.81	−0.88
5	−0.63	−0.38	−0.52	−0.37	−0.44
6	−1.20	−0.87	−0.99	−0.88	−0.97
7	−0.84	−0.57	−0.72	−0.58	−0.69
8	−0.71	−0.40	−0.53	−0.36	−0.47
9	−0.51	−0.18	−0.35	−0.21	−0.32
(3,7)	−0.51		−0.33		−0.27
(7,6)	−0.89		−0.65		−0.63
(6,8)	−0.93		−0.71		−0.64
(8,4)	−0.70		−0.45		−0.39

[1]The rows with single CN (m) and double CNs (m,n) correspond to MeSH–Au_{20} binding complexes via single-coordinate bond and MeS–Au_{20} binding complexes via double-coordinate bond respectively.
[2]The asterisk indicates that the binding energies are CP corrected only for the non-dissociative adsorption with single CN value. The BEs are in eV units.

The PAOs are localized, centered at the nuclei and strictly set to zero beyond a specified cutoff radius. The SIESTA approach is to neglect the overlap matrix elements if two nuclei are far apart and their PAO basis functions do not overlap. This approach reduces simulation time significantly at large N, and the numbers of basis set functions used.[173,177,195] The accuracy of the PAO basis set can be checked by examining the orbital cutoff (discuss in subsection 2.3.2).[93,112,173]

Some of the work presented in Chapter 5 uses the Gaussian 09 program.[196] The program treats the electrons in a similar fashion. The core electrons are described by six gaussian functions in a linear combination way, and the valence electrons are split into three angular momentum channels with three, one and one gaussian functions (Gaussian basis set notation, 6-311G). Both diffuse (+) and polarization (d,p) functions are also included in the calculations, and the Gaussian basis set notation is 6-311+G(d,p).

2.2.4 Periodic boundary conditions

Wavefunctions are solved with the appropriate periodicities between the primary simulating box and its adjacent ones. In this dissertation, three periodic boundary conditions (PBCs) are used: gas, bulk and surface (slab). The gas-type calculation requires a sufficiently large primary simulation box so that any *interactions* or orbital overlapping between the simulating system (in the primary box) and its images (in the adjacent boxes) are prevented. Additionally, the lengths and the shape of the box must stay unchanged and undistorted. For the bulk-type calculation, a crystal structure obtained from the Crystallography Open Database (COD) website and the dimensions of the simulation box both undergo geometry optimization since the optimized lattice lengths depend on DFT functionals. All atoms are allowed to move freely during the optimization in the gas- and bulk-type calculations. The surface-type calculation is processed after its bulk-type optimization. The desired size of a surface (slab) is cut with appropriate PBC from the bulk. The normal vector of the slab is orientated along the z-axis due to convention, and the box length along the z-axis is enlarged by 10X of a system size. Because surface reconstruction is considered in the simulation, we allow the top two layers to move freely for future calculations and keep the bottom layer (the third layer) fixed in position at all times.

Our previous benchmarking study showed that the minimum size of a slab should consist of three layers.[55,60]

2.2.5 The binding energy equations

Reporting and comparing the total energy directly from the simulation output file is meaningless because energy does not have a defined reference. The more relevant data is the energy difference between the reactants and the products. The binding energy of non-dissociative adsorption (physisorption) is calculated as the energy difference of the binding process:

$$\Delta E_{\text{binding}} = E^{\text{complex}}_{\text{complex}} - \left(E^{\text{surface}}_{\text{surface}} + E^{\text{adsorbate}}_{\text{adsorbate}}\right) \tag{2.7}$$

In equation (2.7) and elsewhere in the thesis, subscripts indicate the specific system for which the total energy is calculated, and superscripts indicate the basis set use. The binding energy value is affected by an inconsistency in the simulation settings known as the basis set superposition error (discuss in subsection 2.3.1). The binding energy of dissociative adsorption (chemisorption) is calculated using equation (2.8):

$$\Delta E_{\text{binding}} = (E^{\text{complex}}_{\text{complex}} + \frac{1}{2}E^{H}_{H_2}) - \left(E^{\text{surface}}_{\text{surface}} + E^{\text{adsorbate}}_{\text{adsorbate}}\right) \tag{2.8}$$

2.3 Improvement and Corrections

Using the DF method and the PAO with finite orbital cutoff basis set has the advantage of efficiently simulating a relatively large system. However, the PAO approach suffers a basis set inconsistency when binding energy is computed,[112,144,197,198] and DFT is known to describe vdW interaction inadequately.[187,190,199–201] In order to improve the accuracy of our simulation results, some corrections are applied.

2.3.1 Basis set superposition error and counterpoise method

The practice of using localized short-range PAOs can be computationally efficient but often yields unrealistic and overestimated binding energies. In contrast, results computed using the plane-wave (PW) basis set are more often in good agreement with the experimental values, but can require a prohibitively large basis set.[93,112,195] The basis set superposition error (BSSE) is due to the availability of a larger set of basis set functions in a binding complex than in the separate systems, leading to an over-minimization of the variational energy in the complex. The inconsistent size of the PAO basis set in the binding energy calculation in equation (2.7) is the primary cause for the BSSE: the basis set indicated by the superscripts should be identical. The BSSE is equivalent to an artificial attractive interaction between the adsorbates and the surface, overestimating the binding energy. Although the artificial attraction could partially compensate (or overcompensate) for the lack of vdW attractive interaction, the error cancellation can be vastly dependent on the system.[112,144,197,198] There are two approaches to handle the BSSE problem:

1. To partially remove it by using the counterpoise (CP) method

2. To minimize it by enlarging the orbital cutoff (see section 2.3.2)

For a physisorption system, the CP correction is one way to estimate and partially remove the BSSE from the total binding energy. The basis set inconsistency is corrected by introducing a deformation term which is the energy difference between the final and the initial configuration with their basis sets.[197,198] The binding energy

with the CP correction is:

$$\begin{aligned}
\Delta E_{\text{binding}}^{\text{CP}} &= E_{\text{complex,f}}^{\text{complex}} - \left(E_{\text{surf,f}}^{\text{complex}} + E_{\text{ads,f}}^{\text{complex}}\right) + \Delta E_{\text{def,surf}} + \Delta E_{\text{def,ads}} \\
\Delta E_{\text{def,surf}} &= E_{\text{surf,f}}^{\text{surf}} - E_{\text{surf,i}}^{\text{surf}} \\
\Delta E_{\text{def,ads}} &= E_{\text{ads,f}}^{\text{ads}} - E_{\text{ads,i}}^{\text{ads}}
\end{aligned} \tag{2.9}$$

where def means deformation and the i and f indicate the initial and final configurations respectively. The first three terms on the right-hand side of the first equation in (2.9) are similar to the binding energy equation (2.7) except for their basis set use and the configurations. The deformation energies represents the energy differences between the initial isolated configurations and the final configurations in the complex form, with only account for the incomplete basis set.

An alternative representation is to preserve the original binding energy definition (as in eqn. (2.7)) and treat the inconsistency simply as the error, and the CP correction is to remove the sum of all BSSE terms from the binding energy.[144]

$$\begin{aligned}
\Delta E_{\text{binding}}^{\text{CP}} &= \Delta E_{\text{binding}} - (\Delta E_{\text{BSSE,surf}} + \Delta E_{\text{BSSE,ads}}) \\
\Delta E_{\text{BSSE,surf}} &= E_{\text{surf,f}}^{\text{complex}} - E_{\text{surf,f}}^{\text{surf}} \\
\Delta E_{\text{BSSE,ads}} &= E_{\text{ads,f}}^{\text{complex}} - E_{\text{ads,f}}^{\text{ads}}
\end{aligned} \tag{2.10}$$

The attractive artificial interaction due to the inconsistency overestimates the binding energy, so the ΔE_{BSSE} is a negative value. The CP correction is not perfect; it tends to overestimate the BSSE value and thus over-correct the binding energy in the case of dispersion interaction.[1,112,144,191,202] The next subsection 2.3.2 focuses on minimizing the value of the BSSE.

Using equation (2.10) to evaluate the binding energy with CP correction of a

two-body interaction (e.g., a monomer on a substrate, surface, cluster or another molecule) requires seven total energy terms. For a three-body interaction (i.e., dimer on a substrate), the number of total energy terms goes to ten:

$$\Delta E^{\mathrm{CP}}_{\mathrm{binding}} = \Delta E_{\mathrm{binding}} - \Delta E_{\mathrm{BSSE,surf}} - \Delta E_{\mathrm{BSSE,ads\ 1}} - \Delta E_{\mathrm{BSSE,ads\ 2}} \tag{2.11}$$

where

$$\begin{aligned}
\Delta E_{\mathrm{binding}} &= E^{\mathrm{complex}}_{\mathrm{complex,f}} - \left(E^{\mathrm{surf}}_{\mathrm{surf,i}} + E^{\mathrm{ads\ 1}}_{\mathrm{ads\ 1,i}} + E^{\mathrm{ads\ 2}}_{\mathrm{ads\ 2,i}}\right) \\
\Delta E_{\mathrm{BSSE,surf}} &= E^{\mathrm{complex}}_{\mathrm{surf,f}} - E^{\mathrm{surf}}_{\mathrm{surf,f}} \\
\Delta E_{\mathrm{BSSE,ads\ 1}} &= E^{\mathrm{complex}}_{\mathrm{ads\ 1,f}} - E^{\mathrm{ads\ 1}}_{\mathrm{ads\ 1,f}} \\
\Delta E_{\mathrm{BSSE,ads\ 2}} &= E^{\mathrm{complex}}_{\mathrm{ads\ 2,f}} - E^{\mathrm{ads\ 2}}_{\mathrm{ads\ 2,f}}
\end{aligned} \tag{2.12}$$

For chemisorbed systems, estimating the BSSE using counterpoise method is problematic because the fragmentation of the final optimized complex is more arbitrary than for physisorption.[197,198] Before finding a more reasonable method or a workaround counterpoise method for the dissociative adsorption, the BSSE remains. Although the CP correction does not apply to the dissociative adsorption in this thesis, we aim to minimize the BSSE by enlarging the orbital cutoff (discuss in subsection 2.3.2).

2.3.2 Energy shift and PAO cutoff

In benchmarking calculations, we found large instabilities in both binding energies and BSSEs when using SIESTA default settings, DZP basis set with small PAO cutoff radii. Some calculations even show that BSSE values are comparable to binding

energies.[60,144] One way to minimizing BSSE is to increase the size of the basis set from DZP to TZP; however, the improvement observed in this case was insignificant based on our previous benchmarking data. An alternative approach is to increase confinement radii for the PAOs.[60,93,144] By extending the cutoff radius of the first ζ pseudo-orbital of the carbon atom from 4.1 Å to 6.1 Å (see Fig. 2.7), a converged

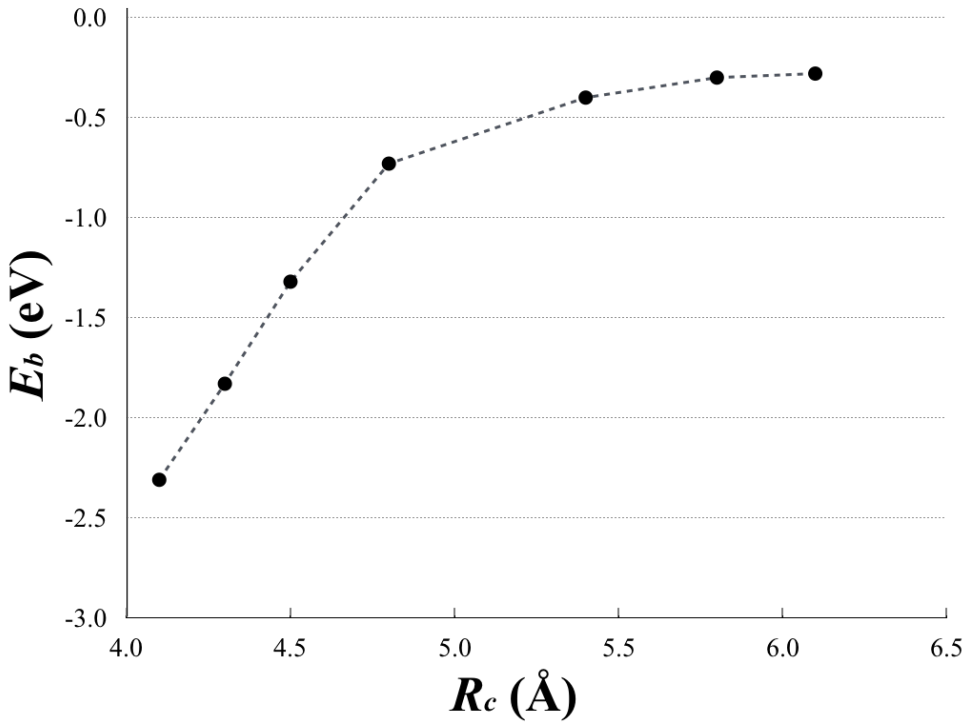

Figure 2.7: Cutoff radius dependence of the binding energy. Data is presented for the cutoff radius of the first ζ pseudo-orbital of the carbon atom; cutoff radii of other pseudo-orbitals present a similar impact on binding energy.

value of the binding energy in this particular case (a cysteine molecule on the Au(110)-missing row surface) is obtained around -0.3 eV. SIESTA uses energy shift rather than a more conventional orbital cutoff, and the equivalent energy shift value of 6 Å (in Fig. 2.8) is 1 mRy.[60,93,112,144] Because of CP correction overestimates the BSSE energy and thus over-corrects the binding energy, decreasing the BSSE value improves the confidence level of our simulation settings and the accuracy of the results.

Table 2.1 shows that the BSSE values are reduced to less than 0.2 eV. The table also illustrates that the binding energies between DZP and TZP now only differ by less than 0.1 eV with the extended cutoff radius, and the differences become insignificant as CP correction is applied. Increasing the PAO cutoffs also change the adsorbed configuration. In our previous study,[60] the chemisorbed geometries of the *L*-cysteine monomer on the Au(110)-(1×2) missing row surface (see Fig. 2.8) with two orbital

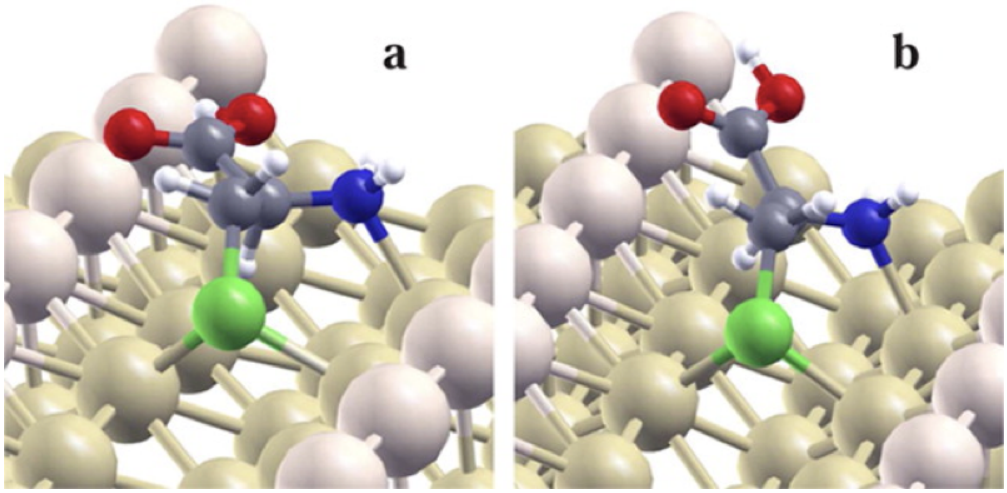

Figure 2.8: Optimized chemisorbed geometries of protonated cysteine on Au(110)-(1×2) missing row surface with two orbital cutoff R_c values for the first ζ pseudo-orbitals of the carbon atom: **a**. 4.1 Å and **b**. 5.8 Å. A shorter orbital cutoff value resulted a shorter distance between the carboxylic group and the surface.[60]

cutoffs (4.1 Å and 5.8 Å) present the over-bound structure of the carboxylic group on the surface for the shorter orbital cutoff.[60]

2.3.3 Van der Waals corrections

Even though vdW forces are weak at the individual atom and molecule level, they play a fundamental role in the binding event because overall vdW contributes to energy in anisotropic fashion.[2,105,112,190,193,203,204] The binding strength depends greatly on the relative orientations of any two interacting bodies.[112] Despite the importance of the in-

teractions, DFT is known to describe vdW interactions inadequately.[187,190,199–201] The absence of vdW awareness in simulations generally underestimates the binding energy and forms less correct binding configuration.[205–209] For example, GGA, without vdW correction, underestimates the binding strengths of two graphene sheets and carbon nanotubes, and predicts the stable structures to be unbound, which the experimental results show otherwise. Therefore, many early papers that studied aromatic-based materials used LDA to obtain more accurate results in terms of the binding energies and configurations as experimental observations.[187,199,200,208,210,211] However, the accuracy comes from a cancellation of errors rather than a more appropriate description of the electron density.[190,199–201,207,208] One significant error cancellation is that LDA overestimates the medium-range vdW while neglecting the long-range vdW, and the two errors happen to cancel out for some physical properties.[190] In recent years, many corrections and adjustments have been developed to incorporate medium and long-range vdW in GGA, and the overall performance has been improved.[2,47,112,193,212–214]

Empirical D2 and TS formalism: One of the popular recipes is the empirical Grimme-type medium range two-body pairwise vdW correction (D2).[2,193,212–214] The dispersive interaction is paired between any two atoms within some specified effective ranges, and the interatomic potential is described empirically by a C_6R^{-6} term as part of the LJ potential:[212,213]

$$E_{\text{disp}}^{\text{D2}} = -s_6 \cdot \frac{1}{2} \sum_{i,j=1}^{N} \frac{C_6^{ij}}{R_{ij}^6} \cdot f_{\text{dmp}}(R_{ij}) \tag{2.13}$$

The dispersion coefficient C_6^{ij} and vdW distance R_{ij} between atoms i and j are computed by using the following equations:[213]

$$\begin{aligned} C_6^{ij} &= \sqrt{C_6^i \cdot C_6^j} \\ R_{ij} &= R_i + R_j \end{aligned} \tag{2.14}$$

The s_6 and $f_{\mathrm{dmp}}(R_{ij})$ are the global functional-specific scaling factor and the Fermi-type damping function respectively.[193,212,213] The 1/2 is to correct for double-counting. Dispersion coefficients, C_6 and van der Waals radii, R_6 for H, C, N, O and S were taken from the original Grimme paper,[213] and those for Au from Liu *et al.* with surface screening correction (Tkatchenko-Scheffler method).[1,215] Most of the elements are parameterized distinctively. However, the *d*-block elements in the same row are parametrized identically for simplicity reason,[213] and the accuracy of the dispersive interaction may be improved by re-parameterizing these *d*-block elements distinctively.

Here, we benchmarked some simulation settings on the complex of a methylthiol on a designed 20-atom gold cluster and examined the effectiveness of the TS formalism to the binding energies and configurations. We found that the total binding energies are enhanced significantly by the vdW-TS correction and dominated by the vdW contribution even for the smallest hydrocarbon group (-CH_3) as illustrated in Fig. 2.9 (f). In terms of the configurations (see Fig. 2.9), the vdW-TS correction shortens the bond lengths and widens the polar angles; however, the changes are insignificant.

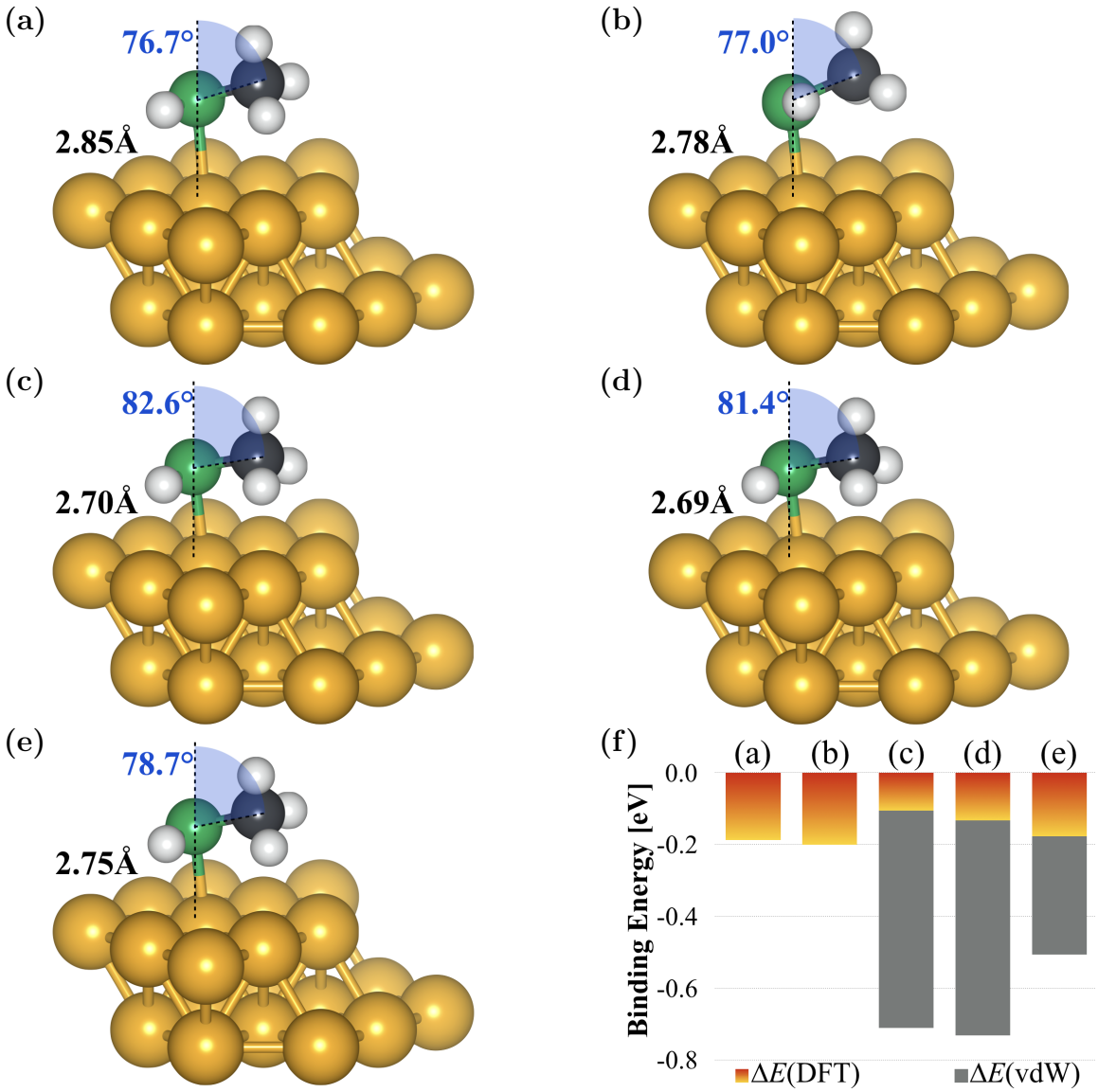

Figure 2.9: Benchmark the simulation settings: panels (a) and (b) are DZP and TZP without vdW correction; panels (c) and (d) are DZP and TZP plus vdW correction with scaling factor $s_6 = 1.66$; panel (e) is TZP plus vdW correction with scaling factor $s_6 = 1$. The bond lengths (S–Au) and angles are reported. Panel (f) presents the binding energies.

The global scaling factor s_6 is a functional-specific scaling parameter, and SIESTA default setting is $s_6 = 1.66$. However, this particular default value caused the overall vdW binding energies to be overestimated when we benchmarked a cysteine monomer on Au(111) surface. The value s_6 has been adjusted from 2006 to

2016 by Grimme *et al.* and Tkatchenko *et al.*, and the latest suggested value is $s_6 = 1$ for the PBE functional.[1,2,193,213,214] We, here, also examined the effect of s_6 on binding energies in SIESTA. Fig. 2.10 shows three typical binding modes of cysteine on Au(111): the zwitterionic form with binding mode of S–Au in panel (a), the nonionic form with binding mode of thiol–Au via a covalent bond in panel (b), and the nonionic form with binding mode of amine–Au physisorbed on the surface in panel (c). Despite different s_6 values (1.0 and 1.66), the structural differences of the optimized configurations are insignificant. The bond lengths are reduced less than 0.1 Å with the larger s_6 value. However, the binding energies for the vdW interaction (shown as the gray part of the binding energies in Fig. 2.10 (d)) are reduced by almost two-fold. The alteration of the vdW binding strengths also causes a small reduction of the binding energies of the covalent type interaction (the orange-red part of the binding energies). Table 2.2 shows that the binding energies which are computed using unity global scaling factor are in better agreement with the reference results that were computed using the same method (PBE-D2) and the hybrid-functional (B3PW91). One of the major advantages of vdW-TS correction is that it improves the overall accuracy of binding energies without demanding more computing resources due to its empirical nature. Therefore, the correction is ideal and suitable for simulating a relatively large system.[212,213]

The three-body (D3) formalism is the improved version of the D2 by introducing an extra D3 dispersive energy term to the total energy. In theory, the performance may be improved by adding more terms.[214] The performance of D3 is beyond the scope of this dissertation, thus it is not benchmarked and used here. More details about the D3 approach are available in Grimme's papers in 2010 and 2016.[193,214] Other than the Grimme-type and Tkatchenko-Scheffler-type pairwise dis-

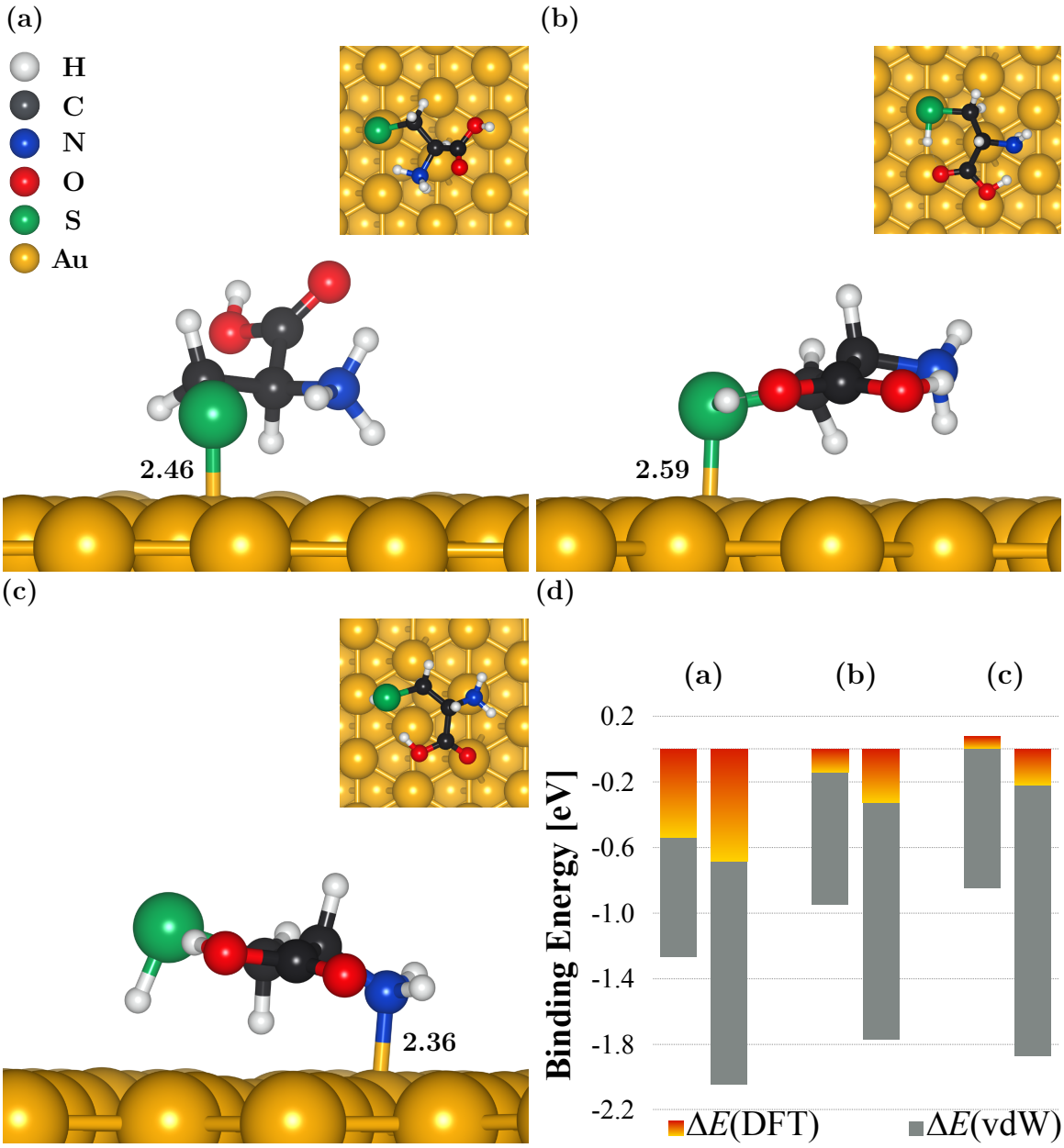

Figure 2.10: Comparing the values of global scaling factor s_6 with the SIESTA default value ($s_6 = 1.66$) and with the suggested value by Tkatchenko ($s_6 = 1.00$).[1,2] Panels (a), (b) and (c) show the zwitterionic form of cysteine with the binding mode of S–Au, the nonionic forms with the binding modes of thiol–Au and amine–Au, respectively. In panel (d), the binding energies are presented in pair with ($s_6 = 1.00$) on the left side and ($s_6 = 1.66$) on the right.

Table 2.2: Binding energies (BEs) of zwitterionic, chemisorbed and physisorbed cysteine monomer and dimer on a Au(111) surface with our latest simulation setting - DFT-TS/GGA/PBE with unity global scaling, TZP with 1 mRy energy shift. The BEs for the dimer systems on the surface are reported per dimer, not per monomer.

chirality	BE(zwit.)[1]	BE(chem.)	BE(phys.)	functional	year	ref.
L	-1.3		$-0.8 \sim -1.0$	PBE-TS	2018	this work
		$-0.46 \sim -0.81$	-0.26	PW91	2003	[47]
		$-0.71 \sim -1.05$	$-1.08 \sim -1.13$	B3PW91	2007	[216]
			-0.27	RPBE	2012	[51]
	-0.97		$-0.44 \sim -0.60$	PW91	2013	[54]
	-1.38		$-0.68 \sim -0.91$	PBE-D2	2013	[54]
D	-0.72		$-0.36 \sim -0.57$	PW91	2013	[54]
			-0.4	PBE	2014	[55]
	-1.12		$-0.52 \sim -0.95$	PBE-D2	2013	[54]
LL	$-1.3 \sim -1.4$			PBE-TS	2018	this work
			$-1.2 \sim -2.1$	PW91	2004	[109]
			-1.36	PW91	2013	[54]
			-1.92	PBE-D2	2013	[54]
DD			-1.38	PW91	2013	[54]
			-1.46	PBE-D2	2013	[54]

[1]The energies are in eV units.

persion corrections (D2 and TS) , the exchange-dipole moment (XDM) method by Becke and Johnson is also widely used for treating the dispersive interaction in an additive manner.[193] However, the SIESTA package (ver. 4.0) does not yet support it.

Beyond D2 and D3 approach: Other than the empirical approach to adjust the missing medium- and long-range vdW interaction problem of DFT, a more advanced approach is to include the non-local density contribution in the functional of the correlation term in the DFT self-consistent framework. This vdW-inclusive approach is called vdW-DF.[2,112,193,217–219] Since vdW-DF is not used in this dissertation, more (SIESTA relevant) details can be found in SIESTA manual.[220]

In conclusion, all the methods for including the vdW interaction are more or less system-specific. The choice for using a particular method depends on the size (the number of atoms) of a simulating system, the amount of benchmark required, the robustness and flexibility of a method and so on. The Grimme-type and Tkatchenko-Scheffler-type pairwise correction methods are by far the most robust and flexible methods with almost no additional computing resources required. However, the pairwise method could not distinguish the different chemical environments of the same element. For example, the carbon atom in single-, double- and triple-bond has the same dispersion coefficient, C_6. Even though one could make the carbon distinguishable by re-parameterizing the coefficients, the benchmarking may take time, and the resulting coefficients may be less transferable. In contrast, the higher-ladder functionals and the vdW-DF functionals are less user-flexible on modifying parameters; however, the methods are more self-consistent. In this study, we chose to use the vdW-TS correction because it is resource-friendly and produces satisfying accuracy in the DFT framework level. The resources would be used to increase the size and complexity of the simulating system.

2.4 Limitations of the DFT method

Zero-temperature DFT: Geometry optimization is done by moving on a path in the configurational space along the steepest decent. However, it does not necessarily mean the outcome ends at the global minimum. Most likely, a configuration is obtained at a local minimum. AIMD method is an elegant workaround. By supplying some thermal energy (heat) in the simulation, a less stable configuration could overcome the low potential barriers and eventually land on the more stable state. However, AIMD has a large computational cost. An alternative approach is to use

classical MD until the simulated system reaches the thermal equilibrium state, and then choose some stable configurations to feed into the DFT calculation. In this study, our strategy is to provide a broad set of input configurations which could be generated systematically by some chosen parameters (distances, angles, etc.), constructed manually based on the chemical intuition, or some previous results. AIMD simulations were only run on a few stable configurations for sampling the evolution of conformations by a given temperature.

Computational costs: Although many improvements have been made to lower the computational costs, the DFT method is still not computationally cheap when a simulating system is structurally complex with many degrees of freedom and consisting of many atoms, valence electrons and PAOs. Generally, optimizing a structurally complex system often requires more numbers of geometry optimization steps and therefore requires more calculation time (see Table 2.3). Since the calculation times

Table 2.3: Computational costs for various simulating systems in this thesis.

Systems[1]	e^{-2}	Node (CPU)[3]	Time[4]	Steps[5]	Time/Step
MeSH–Au_{20}	234	1 (32)	05:16:23	396	00:48
Me_2S–Au_{20}	240	1 (32)	02:30:25	188	00:48
$MeNH_2$–Au_{20}	234	1 (32)	03:21:57	275	00:44
cys. monomer	1890	4 (32)	07:59:57	195	02:28
homocys. monomer	1896	3 (48)	13:29:10	524	01:33
met. monomer	1902	4 (32)	04:58:56	210	01:25
cys. dimer	1932	6 (32)	11:23:53	503	01:22
homocys. dimer	1944	6 (32)	21:04:11	820	01:33
met. dimer	1956	6 (32)	22:35:51	875	01:33

[1]The systems are adsorbates on Au_{20} cluster and amino acids (cysteine, homocysteine and methionine) on Au(111) surface.
[2]Total numbers of valence electrons.
[3]Numbers of nodes used and numbers of CPUs per node.
[4]The calculation time in hh:mm:ss format.
[5]Numbers of geometry optimization steps.

per step (Time/Step) are relatively consistent with similar computational settings,

our strategy of shortening calculation time is to pre-optimize a system (or parts of an entire system) using a classical force field method before running quantum calculation. This strategy works effectively when the classical force field prediction agrees with the quantum prediction and less effective otherwise. A more realistic surface model often requires more atoms (and thus more electrons) especially involving noble metals. For example, a 20-atom gold cluster Au_{20} and a three-layer Au(111) surface used in this dissertation have 220 and 1848 valence electrons, respectively. Although requesting more CPUs may help to shorten the calculation time, this act may backfire and increase the queue time, so the total time (queue and calculation time) is not reduced. From our benchmarking results shown in Table 2.3, 3 to 4 nodes work efficiently for 2000-electron calculations. Additionally, freezing some atoms helps to reduce some calculation time, and this strategy is used for all the surface calculations.

2.5 Conclusions

In this dissertation, most of the simulation results were computed by SIESTA packages 3.2 or 4.0 using KS-DFT formalism, and the KS exchange-correlation energy term was approximated by GGA with *pure* PBE functional. The empirical Tkatchenko-Scheffler-type pairwise (TS) method was used to sufficiently correct the medium-range vdW energy term. The global scaling factor s_6 was readjusted to unity based on our benchmarking results and literature suggestions. A localized finite-range PAO basis set with the TZP was used. The orbital cutoffs were readjusted and extended (equivalent to 1 mRy) to minimize the BSSE values. The CP correction was applied to non-dissociative (physical) adsorption. In Chapter 5, most of the gas-phase calculations were computed by the Gaussian-09 program. Similar simulation settings were used, DFT/GGA/PBE with Gaussian basis set, 6-311+G(d,p).

Chapter 3

Coordination Numbers and Binding Reactivities

3.1 Introduction

In the present work, we aim to examine, in a systematic fashion, the dependence of the molecule-surface interactions pertinent to sulfur-containing AAs on surface site coordination. Thiol-substituted AAs may involve in surface bonding via thiol, amino and carboxylic groups. In neutral form, cysteine, homocysteine and methionine have been observed to interact with the surface via the thiol and amino groups, while carboxylic groups are often involved in hydrogen bonding.[45,48,50,55,60,221] Cysteine and homocysteine can establish covalent thiolate bonds with the substrate, upon undergoing homolytic fission of the mercapto group. On weakly-binding facets, the mercapto group can survive, interacting through dispersive forces with the gold atoms. The methyl-thioether group in methionine does not undergo fission. Thus, methionine has been observed to interact weakly with Au(111) at room temperature, with some studies suggesting that the sulfur atom may be impeded by the bulky methyl group

and is not involved in the binding.[159,222] Amino groups in all three molecules have also been observed to physisorb on the various metal surfaces via the lone pair. In extended systems, lateral interactions can be established via vdW forces and through hydrogen bonding of carboxylic groups, or amino group – carboxylic group.

With an end goal of developing a coordination-dependent description of amino acid-surface interactions, we focus, in the current work, on the surface-binding groups. To this end, molecular backbones are replaced by methyl groups (a methyl-capping method), so lone-pair, charge-group surface interactions, and the overall backbone-surface interaction are removed. Thus, four molecular forms, methyl-thiol (MeSH), methyl-thiolate (MeS-), dimethyl sulfide (Me_2S) and methyl-amine ($MeNH_2$) were studied in their interaction with a substrate. We designed a 20-atom Au cluster as the substrate, with gold atom sites spanning an array of coordination numbers $N(i)$, with $i = 3$–9, and investigated the binding behavior of single molecules on the cluster.

The adsorption of methyl-thiol, and other thiols, at Au substrates, has been the focus of a large number of studies, given its broad relevance in spectroscopy, sensing, nanotechnology and biophysics. Many reviews have been written in the last two decades on the topic of thiol adsorption on gold flat surfaces and clusters,[223–235] and on that of amino acid-gold binding.[24,25,236–242] The primary objective is to investigate the effects of the binding strengths in terms of the direct bindings (S–Au and N–Au) and the vdW interaction due to the coordination numbers of the binding sites, local facets and their nearest neighbours. We find that despite the limited size of the adsorbates, dispersive interactions play a crucial role in determining preferred adsorption sites. The strongest adsorption occurred at relatively unsaturated sites, but also provided sufficient neighbouring surface atoms available to interact dispersively to the molecular backbone.

3.2 Methodology

Configurational sampling. Here, we perform a systematic scan of possible initial structures by sampling the configurational space through four variables, as illustrated in Fig. 3.1: the distance from the adsorbate headgroup to a gold binding site d, the polar angle θ (the angle between the principal axis of the adsorbate and the axis normal to the binding surface), the azimuthal angle ϕ (describing the in-plane orientation of the projection of the adsorbate principal axis), and the relative location of the headgroup with respect to the substrate atoms, labelled from **a** to **j** in Fig. 3.1 (a). Two

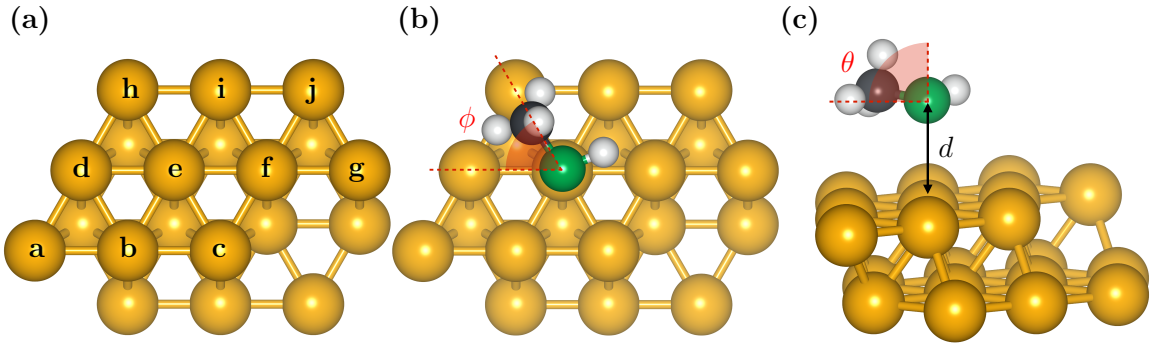

Figure 3.1: Cluster geometry and configurational variables sampled. In (a), the site nomenclature is given in letters. In (b) and (c), d is the sulfur-gold distance, θ is the polar angle (90 ° in each initial configuration), and ϕ is the azimuthal angle.

initial molecule-surface distances were used for sulfur-containing adsorbates (4.3 and 4.5 Å) and additional 4.1 Å was used for methyl-amine, equilibrating to an average S–Au distance of 2.5 Å for sulfur-containing compounds, and to an N–Au distance of 2.3 Å for methyl-amine. From another set of benchmarking calculations, we sampled four polar angels ($\theta = 0°, 30°, 60°$ and $90°$), and both the $60°$ and $90°$ resulted in same configurations of the complexes with lower binding energies from the results of another two polar angles. Therefore, we decided to use ($\theta = 90°$) to be the only polar angle. The in-plane angle ϕ was sampled in 12 increments of $30°$. Initial headgroup locations were considered at both bridge and atop sites. On the Au_{20} cluster, ten atop

sites and 18 bridge sites were considered for each molecule. Overall, 672 initial structures were considered for each of MeSH, MeS and Me_2S, and 1008 initial structures for $MeNH_2$. After the first set of calculations, additional calculations were performed for low-coordinated binding sites, to ensure proper sampling of the configurational space. A fraction of the most stable optimized configurations, their binding energies and bond lengths for the different binding sites are discussed in the Results section.

The small Au cluster was designed as a cut from an ideal Au fcc lattice. The cluster was built to exhibit a variety of kink, edge, adatom, and surface binding sites, with a broad array of coordination numbers (CNs). The CN refers to the numbers of gold-atom neighbours around a particular gold atom. For example, a CN(9) binding site (a central atom on a (111) surface and referring to site (e) of the Au_{20} cluster) has nine gold atoms around the central gold atom. In order to preserve the designed CNs, the cluster was held unoptimized in the geometry optimization calculations presented here. This approximation neglects the significant relaxation effect of the adsorbate on substrate geometry, but was necessary in order to avoid reorganization of the cluster to a more spherical shape. Such reorganization would preclude the study of the site coordination dependence of adsorption energies and structures, which is the subject of the present work. On the Au_{20} cluster, only the 10 gold binding sites on the top layer were studied (labeled a – j in Fig. 3.1 (a)).

Density-functional theory (DFT) methodology. Calculations were performed using the GGA-based PBE functional[243] with and without dispersion corrections, in the SIESTA 3.2 package.[87,173] Core electrons were described in terms of the core pseudopotentials constructed in the scheme of Troullier and Martins[194] with relativistic corrections for the gold atoms. Valence electrons were described using PAOs with a TZP basis set. The PAOs in SIESTA are strictly localized and fall to zero outside a given cutoff radius by specifying a value of energy shift. Previous

calculations by our group and others[60,93] suggested 1 mRy energy shift (equivalent to 6 Å for the cutoff radius of the carbon PAO with the smallest ζ).

A Grimme-type med-range vdW correction was included in the PBE-D2 calculations[213] with the global scaling factor ($s_6 = 1$). Dispersion coefficients C_6^i and vdW radii R_i for H, C, N and S were taken from the original Grimme paper,[213] and those for Au, from Liu *et al.*.[1] To understand the impact of the dispersive correction on the observed adsorption behaviour, a series of binding energies obtained using *pure* PBE without the vdW correction were also calculated, and the results were almost identical to the red-orange portion (differed by -0.04 maximum) of the binding energies provided in Fig. 3.2. As illustrated in the figure, binding energies obtained using the *pure* PBE functional (the red-orange portion) were weaker and much more homogeneous across the various binding sites than the results obtained using the PBE-D2 method. In conclusion, the dispersion correction enhanced non-dissociative physisorption (MeSH, Me_2S and $MeNH_2$) binding energies by 0.1 eV to 0.5 eV, and moderately increased chemisorption (MeS-) energies by 0.1 eV to 0.3 eV.

Non-dissociative adsorption. The binding energy in non-dissociative adsorption was calculated as the enthalpy of the binding process. For unbound systems, the BSSE was estimated using CP correction method.[197,198] The CP correction is to remove the sum of all BSSE terms from the binding energy using equation (2.10).

Dissociative adsorption. Calculated binding energies for the dissociative adsorption took into account the release of hydrogen as H_2 using equation (2.8). CP corrections were not applied for the dissociative adsorption case, as considering the complex in the molecular (gold+adsorbate) basis set is appropriate in the context of chemical bonding of the two.

3.3 Results and Discussion

We examined the binding behaviour of methyl thiol, in both dissociated and undissociated forms, at the various sites of the Au_{20} cluster, and then the binding behaviour of dimethyl sulfide with stronger dispersive interaction with the cluster. Finally, the interaction of methyl amine at the cluster was examined.

3.3.1 Dissociative adsorption: the methyl-thiolate form

Despite the small size of the molecular backbones considered in this study, the dispersive interactions of the methyl group had a strong impact on binding site preferences and the binding strengths of the covalent bond (S–Au) and of the overall vdW interaction (Me – Au). As illustrated by the binding data in Fig. 3.2 (a), adsorption energies did not follow a direct, monotonous relationship with the degree of unsaturation of the gold atoms at the binding sites. Instead, a convolution and interplay of site reactivity and vdW attraction was found to determine the preference of methyl-thiolate to one or another binding site. Generally speaking, overall dispersive interactions were strongest when the methyl group can be most effectively accommodated by Au atoms in either the top layer or in the bottom layer. As a result, the kink site (**cf**) shows the strongest adsorption (see Fig. 3.2) with the most stable configuration shown in Fig. 3.3 (**cf**). At edge sites, strong methyl–Au dispersive interactions could be established with the top layer as seen for the (**bc**) adsorption site, or strong sulfur–Au covalent interaction could be established when the sulfur and the binding gold atoms were along the same plane (sites **dh**, **hi** and **ij**). On the other hand, strongly unsaturated tip sites with fewer neighbouring gold atoms available for vdW binding (sites **ab**, **ad**, **fg** and **gj**) adsorbed weakly.

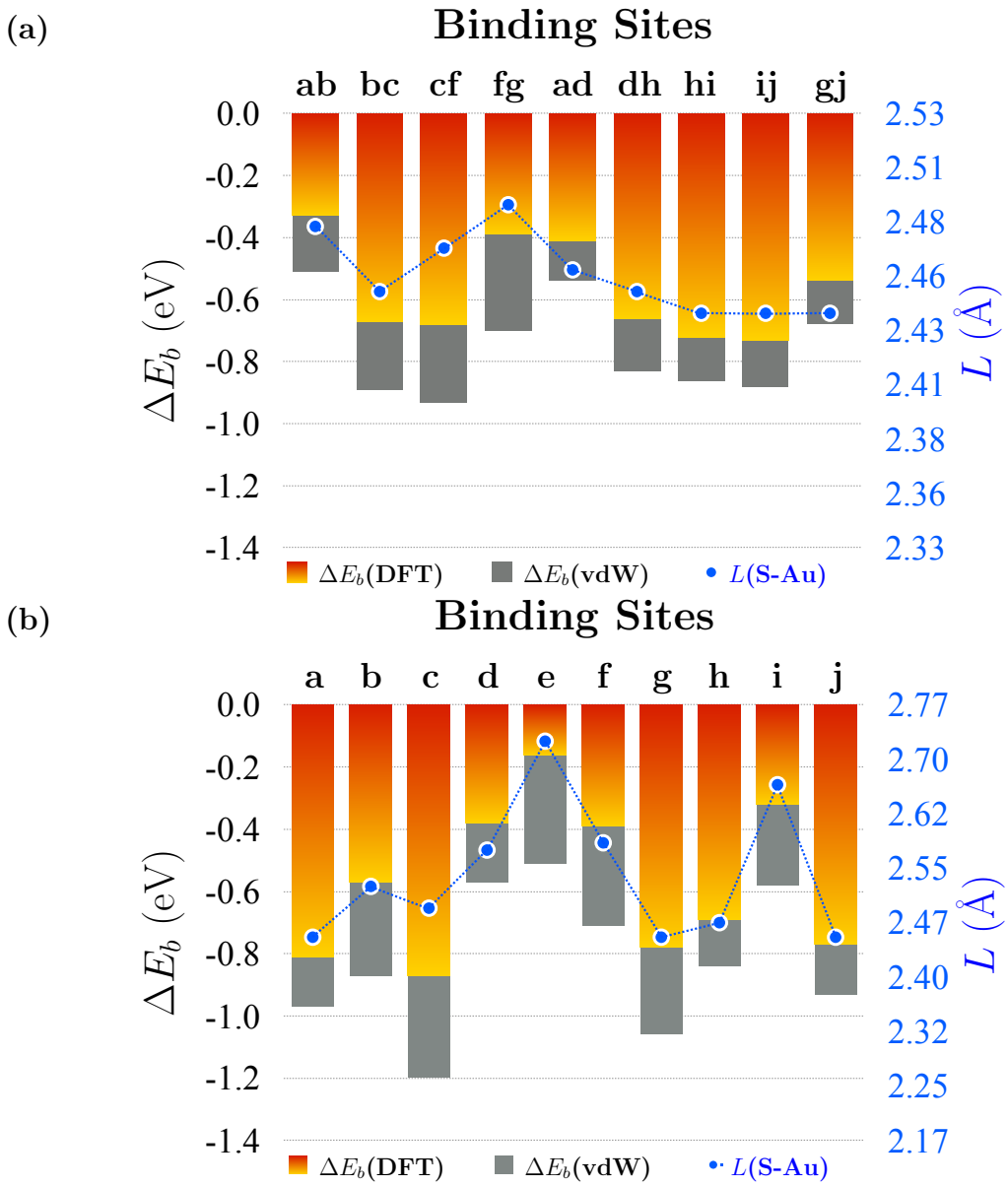

Figure 3.2: Binding energies and relevant distances for MeS dissociative adsorption on the Au_{20} cluster in panel (a) and MeSH non-dissociative adsorption in panel (b). The binding sites nomenclature of the Au atoms are as indicated in Fig. 3.1 (a). Corresponding stable configurations are displayed in Fig. 3.3 for MeS and in Fig. 3.5 and 3.6 for MeSH. The binding energies ΔE_b are calculated by Eqn. (2.8) and (2.9) for MeS and MeSH and represented in columns on the left-side scale. The grey portion of the columns is an estimate of dispersive interactions calculated by applying Eqn. (2.8) to the D2 portion of the binding energies (reported by SIESTA as Emolmec, E_{MM}). Corresponding S–Au bond lengths (averaged over the two Au sites for MeS–Au_{20}) are represented in blue circles, with the scale on the right-hand side.

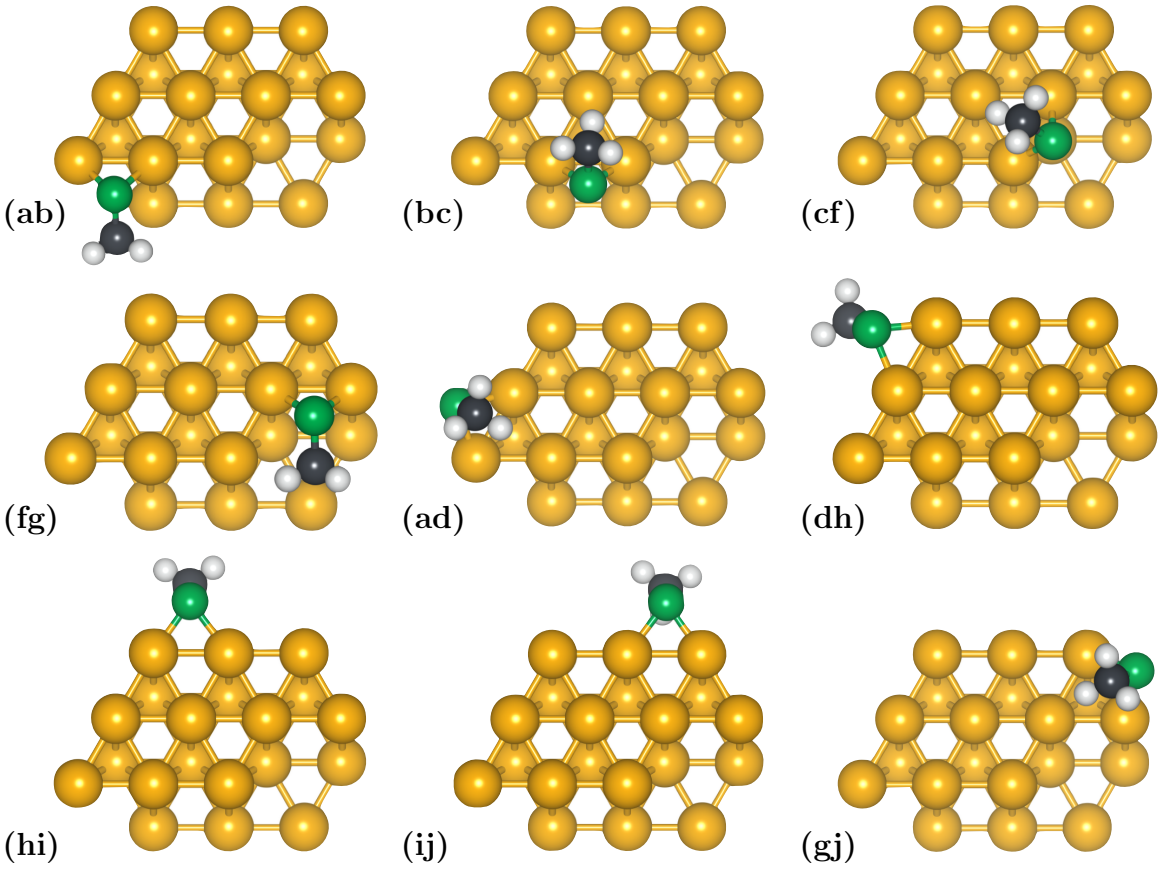

Figure 3.3: The most stable MeS–Au cluster binding configurations for various binding sites on the model Au_{20} cluster. Binding site atoms are indicated in the figure.

The kink site, cf: The strongest binding arose at the relatively well-coordinated kink site, **cf**, with the methyl group either pointed upward position and interacting with the top layer of the cluster (see Fig. 3.4 (**cf1**)), or pointed aligned in an equatorial position and interacting with the bottom layer of the cluster (**cf2**). Total binding energies of the two conformations were the same within the DFT precision as shown in Table 3.1. Coordination numbers at site **cf** were relatively high (6 and 8), with 5 to 7 neighbouring atoms (depending on the orientation of the methyl group) located at less than 5 Å of the centre of the methyl group and available for dispersive interactions.

The low-CN sites, ab, ad, fg and gj: In contrast, binding configurations related to the low-coordinated tip sites **a** and **g**, can only interact dispersively to 3 to

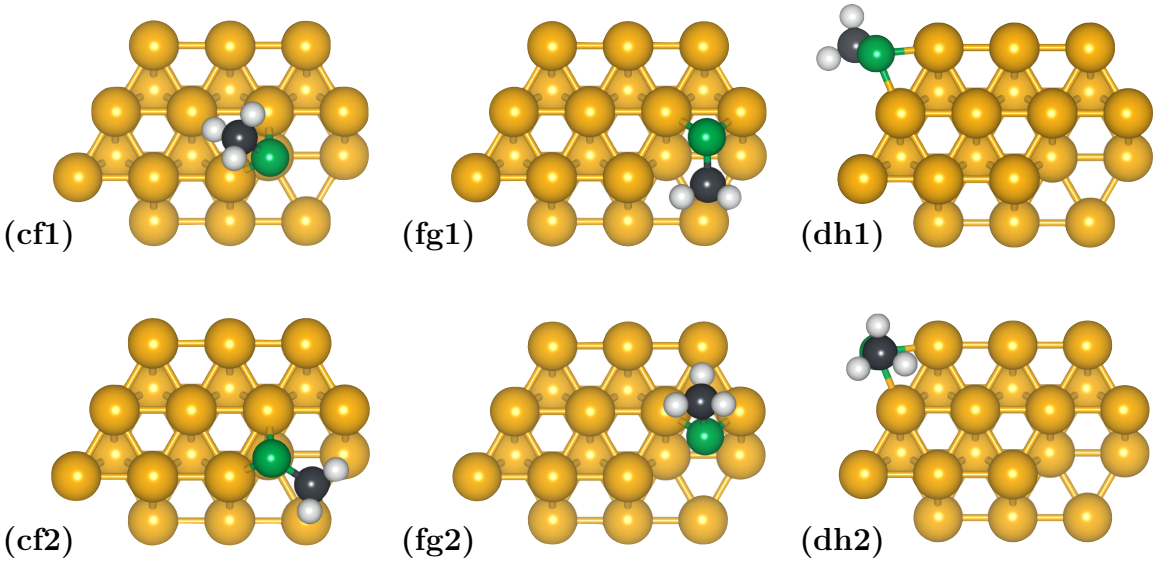

Figure 3.4: The most stable (top panels) and a higher energy (bottom panels) binding configurations for binding sites, **cf**, **fg** and **dh**. Their binding energies and the numbers of neighbours were displayed in Table 3.1.

4 neighbouring gold atoms within 5 Å of the carbon atom, and show weak dispersive and overall binding energies (see Table 3.1 and Fig. 3.4 (**fg2**)). In the present case, lower in-surface coordination does not equate higher reactivity, in the sense of stronger binding to adsorbates. The importance of the dispersive interactions of the methyl group in establishing binding site preference is illustrated by the strong correlation between the overall binding energy (E_b in Table 3.1) and the additional dispersive interaction of the PBE-D2 formalism (E_{MM} in Table 3.1) in this case.

Binding configurations via double-coordinate bond at bridge site: Regardless of binding site, the thiol group adsorbed to the Au_{20} cluster in a two-bond, off-bridge configuration, and this binding configuration was also suggested by others.[235,244,245] In general, Au–S bond lengths were between 2.4 and 2.5 Å (see Table 3.1), with the sulfur atom generally located roughly along one of the gold lattice planes that intersect the two layers. The relative location of the thiolate group was determined to a great degree by the optimization of the methyl group interactions.

Table 3.1: Binding energies and relevant distances for MeS–Au adsorption.

Sites[1]	CN (Au)	E_b (eV)[2]	(d_1,d_2) (Å)[3]	$N_{\text{neigh.}}$[4]	$d_{\text{C-Au;avg}}$ (Å)[5]	E_{MM} (eV)[6]
ab	3,7	−0.51	(2.45,2.52)	4	3.85	−0.18
bc	7,6	−0.89	(2.46,2.45)	5	3.92	−0.22
cf1	6,8	−0.93	(2.45,2.49)	5	3.93	−0.25
cf2	6,8	−0.92	(2.42,2.50)	7	3.90	−0.31
fg1	8,4	−0.70	(2.54,2.44)	7	3.88	−0.31
fg2	8,4	−0.64	(2.53,2.46)	4	3.81	−0.21
ad	3,6	−0.55	(2.43,2.49)	3	3.70	−0.13
dh1	6,4	−0.83	(2.48,2.42)	4	3.80	−0.17
dh2	6,4	−0.81	(2.47,2.42)	3	3.88	−0.13
hi	4,5	−0.86	(2.41,2.46)	4	3.94	−0.14
ij	5,4	−0.87	(2.48,2.41)	4	3.87	−0.15
gj	4,4	−0.68	(2.41,2.47)	4	3.94	−0.14

[1]The indices of the gold atoms are as indicated in Fig. 3.1 (a). Several equilibrated structures are indicated for some of the binding sites, in decreasing order of their binding energies.
[2]Binding energy calculated by Eq. (2.8) in Chapter 2.
[3]Distances from the sulfur atom to the two Au binding sites.
[4]Number of neighbouring atoms (at less than 5 Å from the methyl group) available for dispersive interactions. This number includes the two Au atoms bond to the sulfur.
[5]Average distance from the carbon atom to the neighbouring Au atoms.
[6]The Molecular Mechanics energy as reported by SIESTA, describing overall dispersive interactions.

The orientations of the methyl group: Binding energies did not significantly depend on the orientation (upward or downward orientations shown in Fig. 3.4) for a given binding site (see Table 3.1). For example, at the strongly binding **cf** kink site, a configuration with the methyl group pointing away from the kink and interacting with the top layer of surface atoms, experienced only a 0.06 eV penalty in dispersive energy. It should be specified that, although multiple distinct low-energy configurations were found for each site, the full methyl group desorption (an upright configuration of the methyl group while the thiol end is still bound) carried an energetic cost of 0.6 to 0.9 eV. The Molecular Mechanical binding energy of the methyl group per gold atom was about -0.1 eV. The relationship between the number of neighbours and the

E_{MM} illustrates the additive property of the D2 formalism. This was consistent with experimental and computational reports of methane adsorption on gold surfaces.[246,247]

3.3.2 Non-dissociative adsorption: the methylthiol form

Binding to the substrate via single-coordinate bond at atop site: Depending on adsorption conditions, many thiols maintain their mercapto group undissociated, particularly on less reactive surfaces.[110,116] The thiol group then interacted to the gold substrate through a single surface atom.[55] We examined here the behaviour of complexes of undissociated methylthiol and our Au_{20} cluster, and found that the single-bond configuration provided significantly more orientational freedom to the adsorbate, as illustrated in Fig. 3.5 and 3.6. This in turn allowed both the methyl

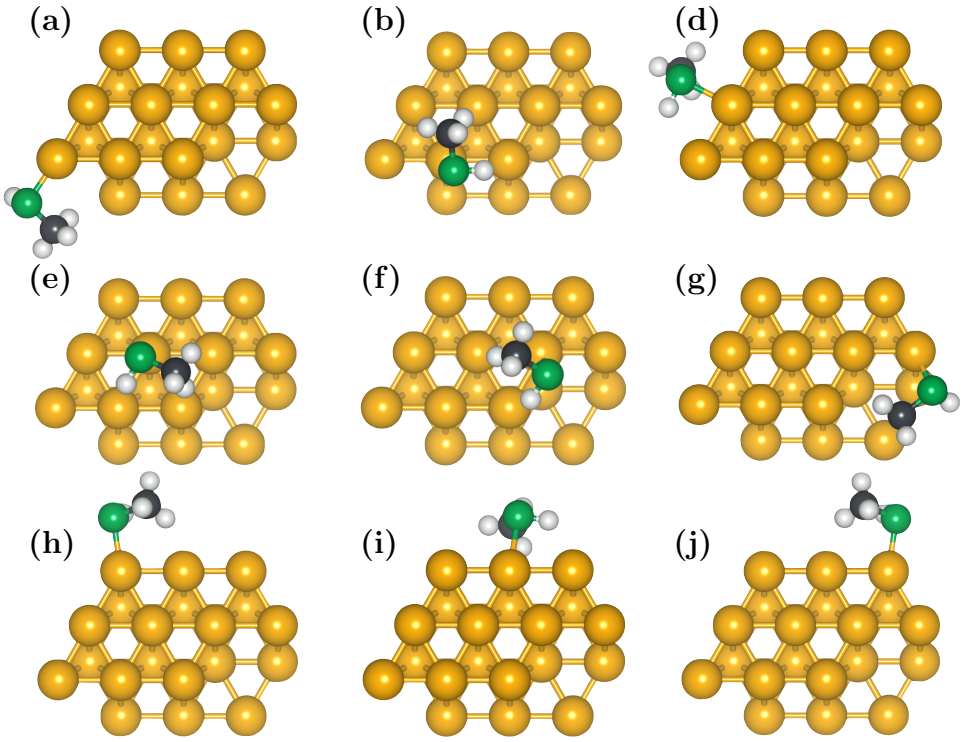

Figure 3.5: Representative minimum energy structures for the non-dissociative adsorption of MeSH at various binding sites on the Au_{20} cluster. The panel labels also represented the binding site. The binding configurations associated with the kink site **c** were shown in Fig. 3.6.

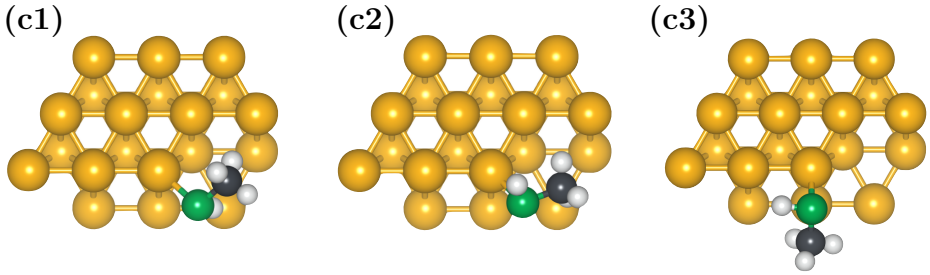

Figure 3.6: Three binding configurations for the non-dissociative adsorption of MeSH at the kink site **c** on the Au_{20} cluster. The panel labels represented the binding site and their binding energies and bond lengths were shown in Table 3.2.

group and the mercapto hydrogen to approach the surface closely, resulting in overall stronger dispersive interactions relative to the thiolate case (see E_{MM} in Table 3.1 and Table 3.2).

Table 3.2: Binding energies and relevant distances for MeSH–Au adsorption.

Site[1]	CN (Au)	E_b (eV)[2]	d (Å)	$N_{\mathrm{neigh.}}$	$d_{\mathrm{C\text{-}Au;avg}}$ (Å)	E_{MM} (eV)
a	3	−0.97	2.45	4	4.06	−0.16
b	7	−0.87	2.52	6	4.09	−0.30
c1	6	−1.20	2.49	6	4.03	−0.33
c2	6	−1.03	2.50	7	3.95	−0.31
c3	6	−0.86	2.52	5	4.06	−0.25
d	6	−0.58	2.59	5	4.00	−0.25
e	9	−0.51	2.73	5	4.00	−0.34
f	8	−0.71	2.58	5	3.98	−0.31
g	4	−1.07	2.46	6	3.85	−0.28
h	4	−0.84	2.48	2	3.52	−0.15
i	5	−0.63	2.61	6	4.19	−0.25
j	4	−0.93	2.45	2	3.50	−0.16

[1]If not otherwise specified, headings are the same as in Table 3.1.
[2]Binding energy calculated by Eq. (2.10) in Chapter 2.

Maximizing the binding energies by balancing the chemisorption and the dispersion: The case of thiol (non-dissociative) adsorption is a clear example of the duality of thiol group-methyl group binding in these systems. The weaker thiol-gold bond, with single coordination, was more free to move in response to favourable methyl binding conditions. This was apparent in a disconnect between the dispersive

added energy (E_{MM}) and the binding energy trends, which had been well correlated in the case of thiolate adsorption. As shown in Fig. 3.2 (b), systems where dispersive forces were relatively strong can be overall more weakly bound when compared to systems where dispersive interactions are relatively weak: for example, binding at atoms **h** and **i** where the dispersive and binding energies were negatively correlated. On the other hand, strong dispersive forces in the **i**-bound thiol were due primarily to methyl-surface interactions, as the relatively long bond length indicated that the thiol group had moved away from the surface. Similar observations can be made for binding at sites **d**, **e** and **f**, with strong overall dispersive forces but relatively long binding distances. The strongest bonds were formed when both of the groups can be satisfied (at sites **c** and **g**, for example).

3.3.3 A stronger dispersive interaction: the dimethyl sulfide

Similar to methylthiol binding geometries, dimethyl sulfide (DMS) chemisorbed single-coordinately to the atop sites of the Au_{20} cluster, establishing stronger dispersive interaction because of the extra methyl group. Due to the size of the Au cluster, only three binding sites (**c**, **e** and **f**) provided overall maximum surrounding gold neighbours for the methyl groups (see $N_{\mathrm{neigh.}}$ values in Table 3.3 with corresponding configurations shown in Fig. 3.7 and 3.8).

For other sites, either only one of the methyl group maximized its neighbours (i.e. sites **a** and **g**) or the two methyl groups equally shared the neighbours (i.e. sites **d**, **h**, **i** and **j**). However, the stronger binding energies were not entirely coming from the dispersion; both the chemisorption and the dispersion were the contributors. As the dispersive interaction increased, the bond lengths of S–Au for the Me_2S–Au_{20} complexes were shortened up to 0.04 Å than to the S–Au of MeSH–Au_{20} (see Table 3.3 and 3.2) leading to the stronger chemisorption contributions. In general, the total

Table 3.3: Binding energies and relevant distances for Me_2S–Au adsorption.

Site[1]	CN (Au)	E_b (eV)[2]	d (Å)	$N_{\text{neigh.}}$	$d_{\text{C-Au;avg}}$ (Å)	E_{MM} (eV)
a	3	−1.15	2.45	3,4	(3.86, 4.06)	−0.24
b	7	−1.05	2.50	3,6	(3.83, 4.06)	−0.38
c1	6	−1.26	2.47	4,7	(3.94, 3.95)	−0.42
c2	6	−1.17	2.48	5,6	(4.14, 4.25)	−0.36
c3	6	−1.05	2.49	3,5	(3.85, 4.13)	−0.34
d	6	−0.76	2.54	2,4	(3.51, 3.92)	−0.29
e	9	−0.70	2.69	5,6	(3.95, 4.07)	−0.46
f	8	−0.89	2.54	4,6	(3.81, 4.06)	−0.45
g	4	−1.27	2.44	3,6	(3.93, 3.88)	−0.34
h	4	−1.05	2.46	2,4	(3.49, 4.11)	−0.25
i	5	−0.80	2.55	2,4	(3.51, 4.16)	−0.27
j	4	−1.14	2.43	2,4	(3.48, 4.10)	−0.25

[1]If not otherwise specified, headings are the same as in Table 3.1.
[2]Binding energy calculated by Eq. (2.10) in Chapter 2.

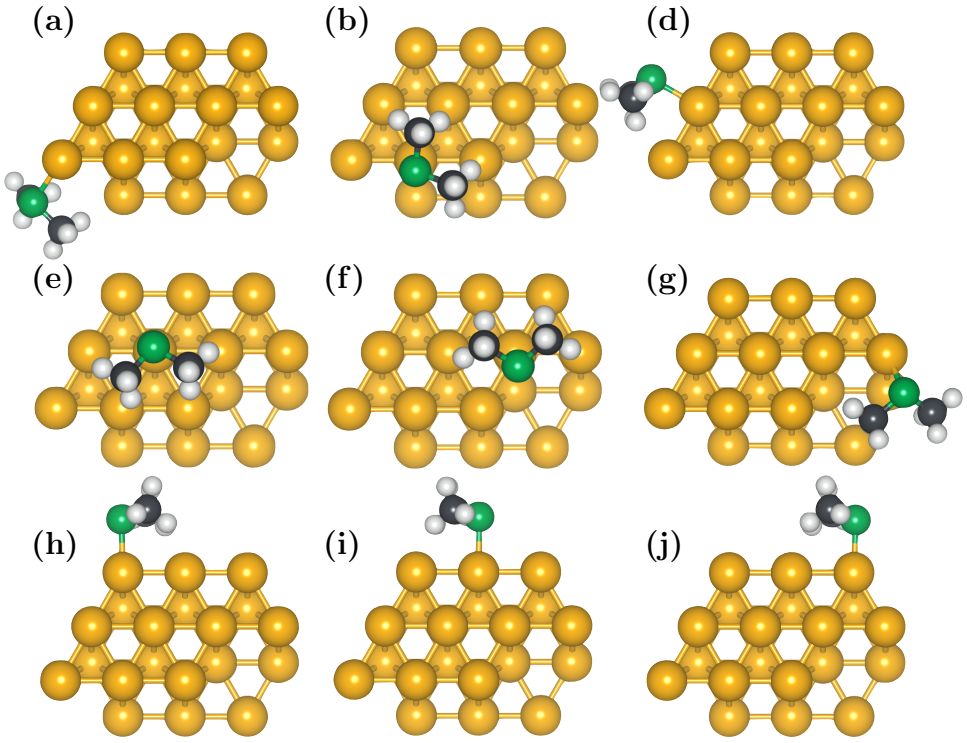

Figure 3.7: Representative minimum energy structures for the adsorption of Me_2S at various binding sites on the Au_{20} cluster. The panel labels also represented the binding site. The binding configurations associated with the kink site **c** were shown in Fig. 3.8.

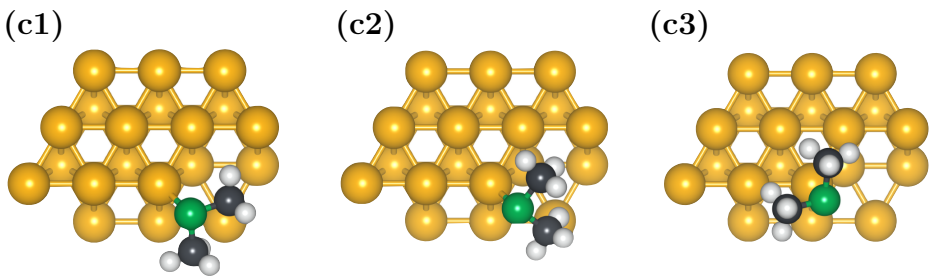

Figure 3.8: Three binding configurations for the adsorption of Me_2S at the kink site **c** on the Au_{20} cluster. The panel labels represented the binding site and their binding energies and bond lengths were shown in Table 3.3.

binding energies of the DMS on Au_{20} complexes were stronger by ∼0.2 eV than the binding energies of the methylthiol–Au_{20} complexes as shown in Fig. 3.9 and Table 3.3.

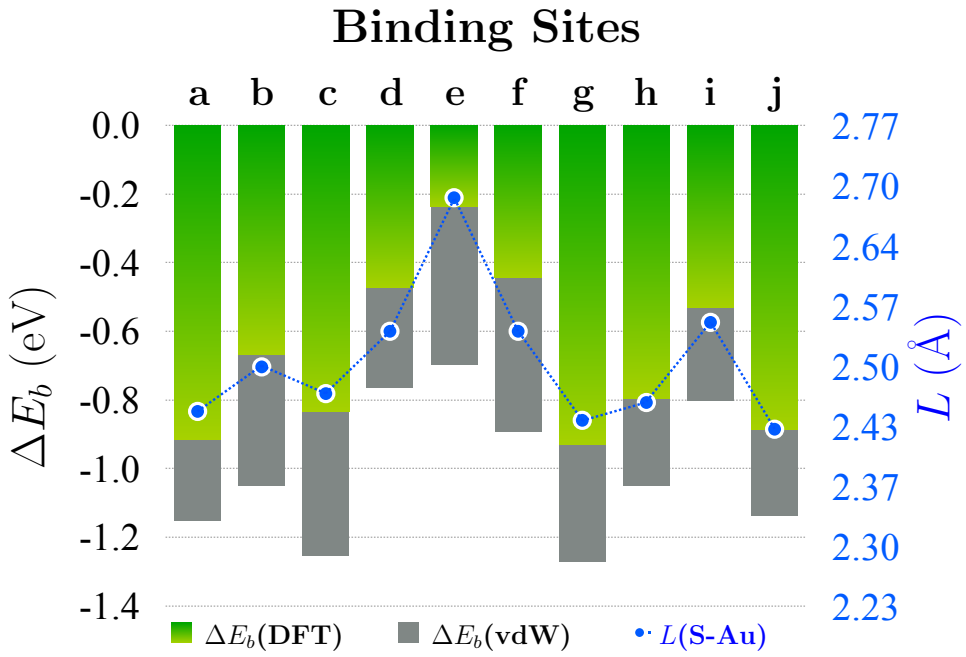

Figure 3.9: Binding energy contributions and bond lengths of Me_2S on the Au_{20} cluster via physisorption with strong dispersion. The green coloured part of the energy is treated as the "chemical bond" energy in the complex. If not otherwise specified, the figure description is the same as in Fig. 3.2 (b).

Effect of dispersive interactions: Fig. 3.8 shows three distinct binding configurations of DMS at the kink site **c**. Dispersive interactions were maximized when one of the methyl sat inside the kink, and another one interacted to the bottom layer as shown in **c1**. Configuration **c2** achieved the same total number of neighbours as **c1**, but had longer methyl-gold distances and a weaker overall binding energy. The number of neighbours reached maximum ($N_{\text{neigh.}} = 11$) only at two binding sites, **c** and **e** with similar E_{MM} values.

3.3.4 A lone-pair to metal interaction: the methylamine

Methylamine physisorbed on gold binding sites via a single-coordinate dative bond due to the lone-pair on the nitrogen.[248–251] Similar binding motifs were encountered previously for *N*-heterocyclic carbene on metallic surface.[16–20] The single-coordinate dative bond provides significant orientational freedom, as illustrated in Fig. 3.10 and 3.11, and the binding strengths of this particular dative bond were remarkably strong as shown in Fig. 3.12. Comparing the binding energies of the methylamine–Au_{20} complexes with the methylthiol-Au_{20} complexes shown in Fig. 3.12 and 3.2 (b) respectively, the differences were insignificant, despite shorter the bond lengths for N–Au than for S–Au. Due to the presence of the more electronegative N centre of methylamine, the stronger binding strengths at low coordinate sites such as **a**, **g** and **j** (see Table 3.4) are reflected in terms of their binding energies. For the binding configurations of the methylamine–Au_{20} complexes on the kink site **c**, three distinct orientations of the methyl group are shown in Fig. 3.11: above the kink with a tilt angle (**c1**), away from the kink equatorially (**c2**), and upward along the normal direction (**c3**). Unlike the thiols discussed above, the methyl group of the methylamine showed no orientational preferences in terms of the binding energies, dispersion energies (E_{MM}) and N–Au distances (see Table 3.4: **c1**, **c2** and **c3**).

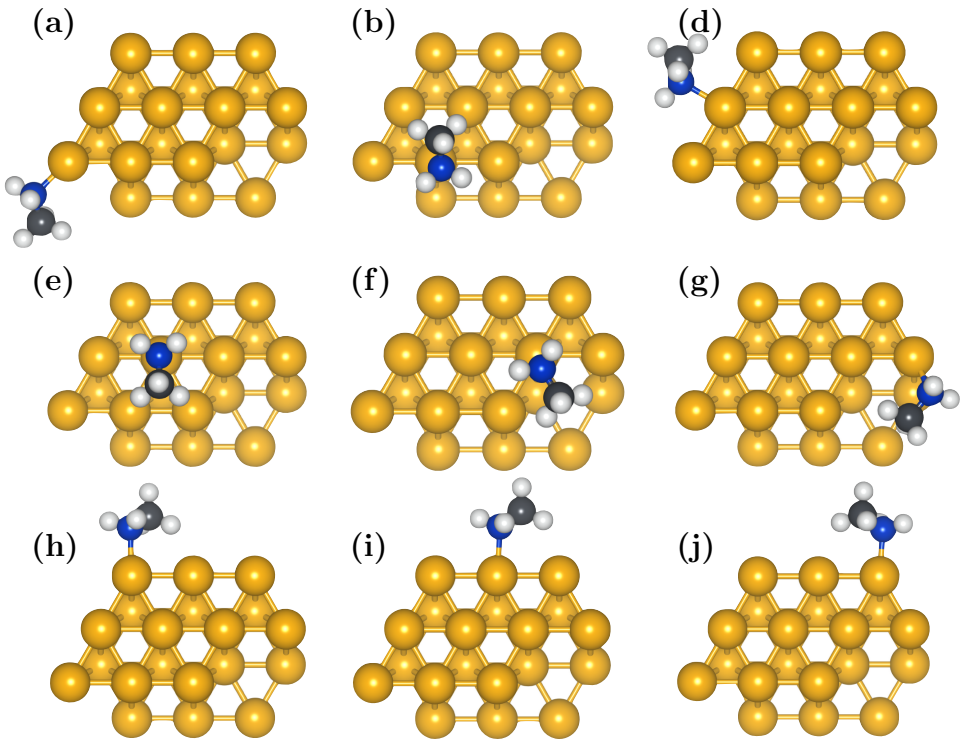

Figure 3.10: Representative minimum energy structures for the adsorption of $MeNH_2$ at various binding sites on the Au_{20} cluster. The panel labels also represented the binding site. The binding configurations associated with the kink site **c** were shown in Fig. 3.11.

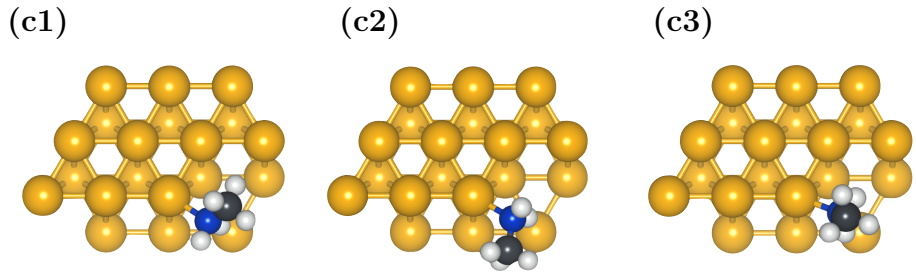

Figure 3.11: Three binding configurations for the adsorption of $MeNH_2$ at the kink site **c** on the Au_{20} cluster. The panel labels represented the binding site and their binding energies and bond lengths were shown in Table 3.4.

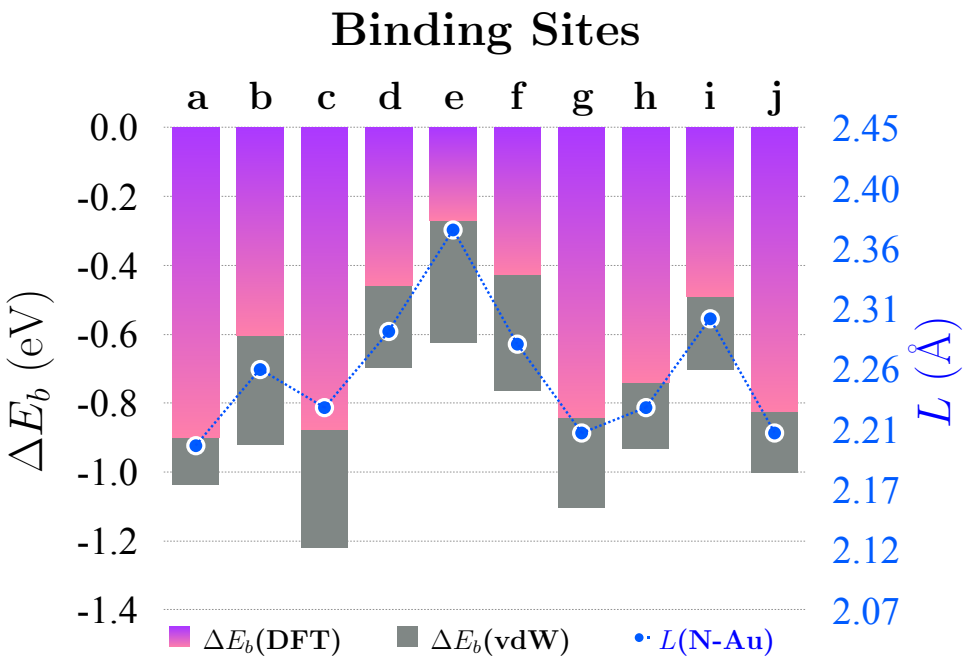

Figure 3.12: Binding energy contributions and bond lengths of $MeNH_2$ on the Au_{20} cluster via lone pair metal interaction. The violet-magenta coloured part of the energy is treated as the "physical bond" energy in the complex. If not otherwise specified, the figure description is the same as in Fig. 3.2 (b).

Table 3.4: Binding energies and relevant distances for $MeNH_2$–Au adsorption.

Site[1]	CN (Au)	E_b (eV)[2]	d (Å)	$N_{\text{neigh.}}$	$d_{\text{C-Au;avg}}$ (Å)	E_{MM} (eV)
a	3	−1.04	2.20	3	4.18	−0.14
b	7	−0.92	2.26	6	3.99	−0.32
c1	6	−1.22	2.23	6	4.03	−0.34
c2	6	−1.19	2.23	4	3.91	−0.32
c3	6	−1.18	2.24	5	4.28	−0.35
d	6	−0.70	2.29	5	4.04	−0.24
e	9	−0.63	2.37	5	3.83	−0.36
f	8	−0.77	2.28	5	4.02	−0.34
g	4	−1.10	2.21	6	3.97	−0.26
h	4	−0.93	2.23	3	3.80	−0.19
i	5	−0.70	2.30	2	3.37	−0.21
j	4	−1.00	2.21	2	3.40	−0.18

[1]If not otherwise specified, headings are the same as in Table 3.1.
[2]Binding energy calculated by Eq. (2.10) in Chapter 2.

3.4 Conclusions

In order to develop an understanding of thiol binding on complex-structured metal surfaces, we pursued an investigation of dissociative and non-dissociative adsorption at a model 20-atom Au cluster. The cluster model presented a series of distinct available binding sites, with coordination numbers between 3 and 9. To limit the set of competing interactions involved in the adsorption process, we examined MeSH–Au complexes over a broad region of their configurational space. The molecules bound preferentially to kink sites where provided a maximum number of neighbouring substrate atoms available for methyl group stabilization. We further examined Me_2S–Au complexes to gain some insights on maximizing the stabilization of two methyl groups, and found that both the kink sites and the flat surface provided enough neighbouring substrate atoms for two methyl groups. Other than the sulfur-containing molecules, methylamine was considered, as amine groups are known to contribute strongly to amino acid binding on metal surfaces. We found that, binding strengths of the coordinate dative bond can be as strong as a covalent bond, and that the orientation of the methyl group played less significant role in methylamine binding. By using Grimme-type medium range vdW correction, we found that dispersive interactions (mainly due to S–Au, SH–Au and CH_3–Au) provide a relatively significant contribution on binding strength ($14\% \sim 67\%$) and configuration even for the smallest hydrocarbon, a methyl group. Despite known issues with the empirical nature of dispersive corrections, their inclusion in calculations was essential in order to access reasonable binding structures, particularly for more weakly-bound molecule groups. In effect, a direct parallel between binding preference and the coordination of the adsorption site cannot be drawn without first examining the binding environment and backbone interactions, for even the simple molecules considered here.

Chapter 4

Amino Acids on Complex Gold Surfaces

4.1 Introduction

Cysteine, homocysteine and methionine have three lone-pair containing groups, that may involve the surface bonding or the intermolecular interaction: the thiol (or disulfide for methionine), amino and carboxylic groups. The generally accepted binding modes of cysteine and homocysteine on the Au(111) surface are that the thiol group physisorbed on the surface, and the mercapto group undergoes homolytic cleavage near the substrate and chemisorbs on the surface with the formation of a covalent S–Au bond and a H radical or molecular H_2.[43,45,52] Methionine only physisorbed on the surface because it does not have a mercapto group, and thus it has been observed to weakly bind to Au(111) at room temperature, with some studies suggesting that the sulfur atom is not involved in the binding.[236,238] The amino group could interact either with the surface via the single-coordinate bond or the carboxylic group intermolecularly via hydrogen-bonding.[252] Whether the adsorption involves the thiolate or

disulfide species remained unclear experimentally, recent first principle calculations generally support the thiolate-surface model.[47] In extended systems, lateral interactions can be established via vdW forces and through hydrogen bonding of the carboxylic or amino group. For example, the two carboxylic groups are often involved in intermolecular interaction via hydrogen bonding in dimerization.[45,48,50,55,60,221] The binding modes vary widely depending on the identity of the thiol/thiolate group, the involvement of the amino group, the ionic states of the thiol and amino groups, the reactivities of the binding sites of the gold surfaces, the environmental conditions (solution phase or in vacuum), the annealing temperature and surface coverage.[25,46–48,91,116,253] The thiyl radicals and the thiols even coexist for many surface coverage conditions. Temperature plays a significant role on the presence of the thiol, thiolate and dithiol species. As the temperature elevated, dithiol group undergoes dissociation and forms thiolate group.[111] Various cystine/cystine monolayer patterns have been observed experimentally on different gold surfaces.[47]

The molecular ionic state introduces an additional complicating factor on the surface self-assembly of AAs. Whether the molecule presents in cationic, nonionic, zwitterionic or anionic form depends on the presence of a solvent, surface coverage, the reactivity of the gold binding site and the nature of the probing experiment.[90,116,216,254–256] Based on XPS measurements on both Au(110) and Au(111), cysteine is mostly nonionic at low surface coverage and zwitterionic at high coverage, even in UHV conditions.[90,116,118] The ionic including nonionic states impact the patterns of the SAMs and the binding modes. Nonionic cysteine multimers form patterns on surfaces with strong binding modes, via thiol/thiolate and amino groups and with intermolecular interaction between carboxylic groups.[45,48,50,72,136,216,221,257] Depending on the surface coverage and the deposition temperatures, zwitterionic configurations exist in two forms: the conventional form with -NH_3^+ and -COO^- pair, and an uncon-

ventional form with -NH_3^+ and the thiolate anion pair.[118,253] The zwitterions interact with the surface and the adjacent adsorbate strongly through static Coulombic forces, and dominating the overall binding energy.

The binding strength between the adsorbate and the surface strongly correlates to the binding site reactivity and thus its saturation - neighbouring atoms of a binding site. Generally, a less saturated (fewer neighbours) binding site has higher reactivity and results in larger binding energy. Experimental and computational studies have established the distinct behavior of sulfur-containing AAs on various metal facets.[25,55,110,112] Previous studies showed that cysteine binds strongly on kink binding sites of (1×2) reconstructed Au(110) surfaces.[60] The phase behaviour of sulfur-containing AAs, and condensed-phase self-assembly patterns, also depends strongly on substrate geometry, because of the impact of the latter on adsorbate-surface interactions.[25,110] The role of adatoms in the strong binding of thiols on Au surfaces has become clearer in recent years. The reactivity of the Au(111) surface increases upon surface reconstruction to form the herringbone structure with unit cell of $(22\times\sqrt{3})$. An adatom model had been proposed to describe the reconstruction and the binding mode of thiolate self-assembly.[52,111,114,232,258,259] Experimentally, the involvement of gold adatoms in thiolate self-assembly can be observed as a staple pattern that methylthiolate (and phenylthiolate) dimers sandwich a gold adatom.[52,259] In simulations, a reactive gold adatom is ejected onto the Au(111) surface to mimic the binding mode of the stripe phase on the herringbone reconstructed Au(111) surface.[111]

Previous computational studies focused on the thiol, thiolate and dithiol adsorption of cysteine monomer and dimer at the Au(111) surface[144] and at the Au(110) surfaces (with and without surface reconstruction)[60] using a *pure* DFT functional (PBE). With most of the input structures from stable (geometry optimized) gas-phase cysteine/cysteinyl conformers, the reported binding energies of the stable adsorbate-

surface complexes with the exothermic adsorption process were between −0.3 eV and −1.3 eV via both the thiol–Au and the amino–Au bonds.[55] However, the nature of the *pure* DFT approach can underestimate binding energies substantially (depending on the system) because it is unable to capture the medium and long-range vdW dispersion.[1,260,261] The dispersion can affect not only the binding strength but also the binding configuration, especially for a long hydrocarbon chain, a benzene group and a relative large delocalization structure.[252] In this study, we implemented the screened Tkatchenko and Scheffler (TS) vdW correction (similar to Grimme-type D2),[1,2,193,213–215] and partition the total binding energy into the binding energy that is approximated by the *pure* DFT method and that estimated by the *ad hoc* D2 formalism. This analysis method is applied to the monomers and dimers of the three AAs on the Au(111) surface with adatom defects.

4.2 Methodology

Zero-temperature density-functional method was used to optimize the configurations of the adsorbate-surface complexes. The optimized configurations strongly depend on their input geometries, because the method suffers from an inability to broadly sample configurational space. This limitation becomes more problematic for molecule-surface interactions as the complexity of the potential energy surface increases due to the overwhelming contribution of the surface.[262] Two approaches to a better sampling of the configuration space are available. One is to generate more input geometries either manually or by other programs and feed them into the zero-temperature DFT geometry optimization. We used this approach in our previous molecule-cluster study.[144] Most of the input geometries were generated systematically in the first trial of geometry optimization, followed by modification based on our in-

tuition as necessary. The main limitation of this approach is that hundreds of input geometries were needed in three sequential trials. Another approach is to provide thermal energy to the simulation using AIMD simulations or equivalent approaches. Unfortunately, currently AIMD is computationally unfeasible for large surface bound systems. We thus generated a large set of input geometries for the geometry optimization in the first trial. Optimized configurations from the first trial were further refined and used in two more sequential trials of geometry optimization.

4.2.1 Models

Two gold slabs, Au(111) and Au(111) with one adatom, with PBCs, were used in this study. The Au(111) slab consisted of three layers with 56 gold atoms per layer. The atoms on the top two layers were allowed to move freely without any constraints to account for any surface reconstruction due to the adsorbates. The bottom (the third) layer was fixed in position to ensure the overall structure remain undistorted. A pre-optimized and then fixed [20.59, 20.34, 100.00] Å simulation box was used to ensure the periodicity of the lattice in the xy plane and minimize image cell interaction in the z direction.

One gold adatom was introduced on top of the first layer to simulate adatom defects. Three relatively stable configurations were obtained with the adatom on the fcc, the hcp and the bridge site in descending stability. The trend was consistent with previous theoretical calculations.[250,263,264] Energy differences between the three locations were less than 0.1 eV in our calculations, below methodological errors. The total energy of the defected adatom at the fcc site will be used as the total energy reference in the binding energy calculations.

Three sulfur-containing AAs, cysteine, homocysteine and methionine were considered as a series of adsorbate, presented in Fig. 4.1. Cysteine and homo-

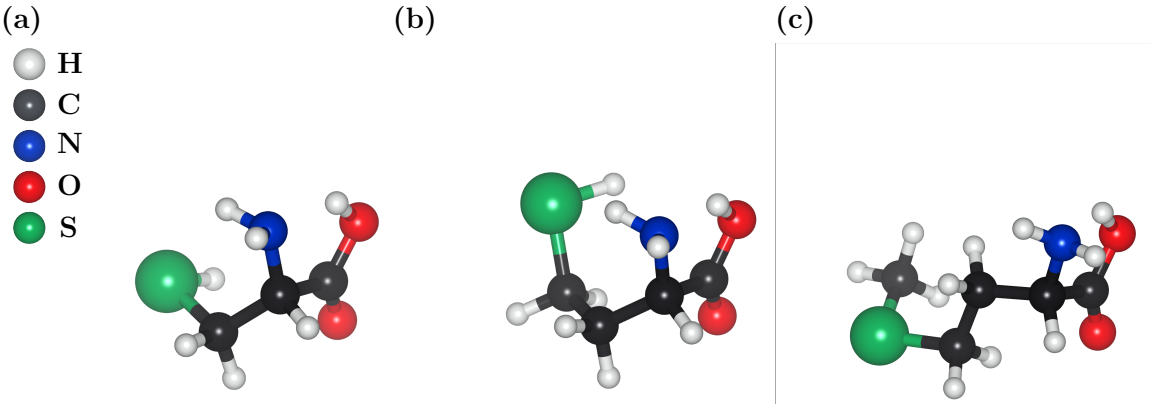

Figure 4.1: Amino acids investigated in this study: **(a)** *L*-cysteine, **(b)** *L*-homocysteine and **(c)** *L*-methionine.

cysteine were deposited on the gold surface in both the physisorbed R–SH (thiol or mercapto group) and the chemisorbed R–S (thiolate) forms, whereas only the physisorbed R–S–CH_3 (thioether) form exists for methionine. Zwitterionic states were also considered for cysteine and homocysteine.

4.2.2 Numerical details

DFT calculations were performed using the GGA-based PBE functional[265] with screened TS-vdW corrections,[2,213,215] in the SIESTA 4.0 package.[87,173] Core electrons were described through pseudopotentials constructed in the scheme of Troullier and Martins[194] with relativistic corrections for the gold atoms. Valence electrons were described using PAOs with a TZP basis set. The PAOs in SIESTA are strictly localized and fall to zero outside a given cut-off radius, chosen by specifying a value of energy shift. Previous calculations by our group and others[60,93,144] suggested 1 mRy energy shift (equivalent to 6 Å for the cut-off radius of the carbon PAO with the smallest ζ) is appropriate for binding energy calculation. Dispersion coefficients, C_6 and van der Waals radii, R_6 for H, C, N, O and S were taken from the original Grimme paper,[213] and those for Au from Liu *et al.* with surface screening correction (a vdW-

TS approach).[1,215] Benchmarking results by our group and others[1,2,193] suggested that unity ($s_6 = 1$) was suitable for the global scaling factor. Previous studies in our group showed that the inclusion of the dispersion corrections usually enhances binding energies by 0.1 eV to 0.5 eV in non-dissociative physisorption (MeSH, Me_2S and $MeNH_2$) and 0.1 eV to 0.3 eV in dissociative chemisorption (MeS-).[144] Binding energy was calculated using equation (2.10) with CP correction.

4.3 Results and Discussion

Binding modes and strengths of the three AAs on the surfaces are discussed below with respect to adsorption of monomers and dimers on ideal and defect surfaces. We examined the effects of backbone length, thiol group substitution, defect sites and presence of nearby adsorbates on the adsorption behaviour of these molecules.

4.3.1 Amino acid adsorption at the ideal Au(111) surface

The three sulfur-containing AAs (cysteine, homocysteine and methionine) exhibited two binding modes on the Au(111) surface: a nonionic (-SH and $-NH_2$) and an unconventional zwitterionic ($-S^-$ and $-NH_3^+$) mode.[118] In the nonionic binding mode, two functional groups, the mercapto group (sulfide for methionine) and the amino group normally interact with the surface via a single-coordinate covalent (S–Au) and a dative bond ($-NH_2$–Au). The two functional groups could also interact with the surface cooperatively with both groups binding to the surface at the same time. In the zwitterionic binding mode, the thiolate group can interact with the surface via a single- or double-coordinate bond, whereas the positively charged amino group ($-NH_3^+$) interacts with the surface via the static Coulombic forces.

Nonionic amino acid monomers on the Au(111) surface:

Cysteine and homocysteine adsorbed weakly on the Au(111) surface via the mercapto group (R–SH). As shown in Table 4.1, the binding energy contributions from *pure* (uncorrected) GGA/PBE method were minor or positive (non-bonding). Dispersive

Table 4.1: CP corrected binding energies and distances for adsorbed nonionic cysteine, homocysteine and methionine configurations on the Au(111) surface.

Binding mode[1]	$\Delta E_{b,\text{total}}$[2]	$\Delta E_{b,\text{DFT}}$[3]	$\Delta E_{b,\text{vdW}}$[4]	$d_{\text{S-Au}}$[5]	$d_{\text{N-Au}}$[6]	Config. Figure
S–Au, cys	−0.84	−0.04	−0.80	2.61	—	4.2 (a)
S–Au, cys	−0.71	+0.11	−0.82	2.61	—	4.2 (b)
N–Au, cys	−0.94	−0.02	−0.92	—	2.31	4.2 (c)
N–Au, cys	−0.78	+0.08	−0.86	—	2.36	4.2 (d)
S–Au, Hcys	−1.08	−0.22	−0.86	2.58	—	4.3 (a)
S–Au, Hcys	−1.00	−0.11	−0.89	2.57	—	4.3 (b)
N–Au, Hcys	−1.00	+0.05	−1.05	—	2.33	4.3 (c)
N–Au, Hcys	−0.73	+0.14	−0.87	—	2.33	4.3 (d)
S–Au, met	−1.44	−0.40	−1.04	2.55	—	4.4 (a)
S–Au, met	−1.25	−0.18	−1.07	2.56	—	4.4 (b)

[1]The binding mode via either thiol group (methyl sulfide for methionine) denoted as S–Au or amino group denoted as N–Au.
[2]Binding energy calculated by Eq. (2.10) with CP correction.
[3]Uncorrected DFT binding energy calculated by taking the difference between the total and the vdW binding energies.
[4]The Molecular Mechanics (vdW) binding energy calculated by Eq. (2.7).
[5]S–Au bond length.
[6]N–Au bond length.

corrections predominated the overall interaction between the three sulfur-containing AAs and the ideal Au(111) surface. Consequently, the overall binding strengths strongly correlated to the orientation and length of the molecular backbone. Methionine binding strength was stronger than homocysteine and finally cysteine. The sulfide group of the methionine had stronger dispersive interaction with the Au(111) surface than the mercapto group of the other AAs, shortening the S–Au bond length (see Table 4.1).

In our previous methylamine-gold-cluster study,[144] the amino group formed a dative bond between the lone-pair of the amino group and the Au(111) facet (Au(111) surface in a cluster form) with a moderate strength of roughly -0.6 eV, with equal contributions of ΔE_b(DFT) and ΔE_b(vdW). For the three sulfur-containing AAs on Au(111), no such bond strengths were observed. In contrast, the amino group showed positive ΔE_b(DFT) contributions for cysteine and homocysteine as shown in Table 4.1. Although the binding interaction via the dative bond was absent, an attractive overall interaction achieved through vdW backbone dispersion. No bound NH_2–surface configurations were found for methionine from geometry optimization. Stabilization of lowest energy configurations was achieved through intramolecular H-bonding between COOH – NH_2, shown in Figs. 4.2, 4.3 and 4.4 for cysteine, homocysteine and methionine respectively. No proton (H^+) transfer from -COOH to -NH_2 groups was observed in the zero-temperature DFT calculation.

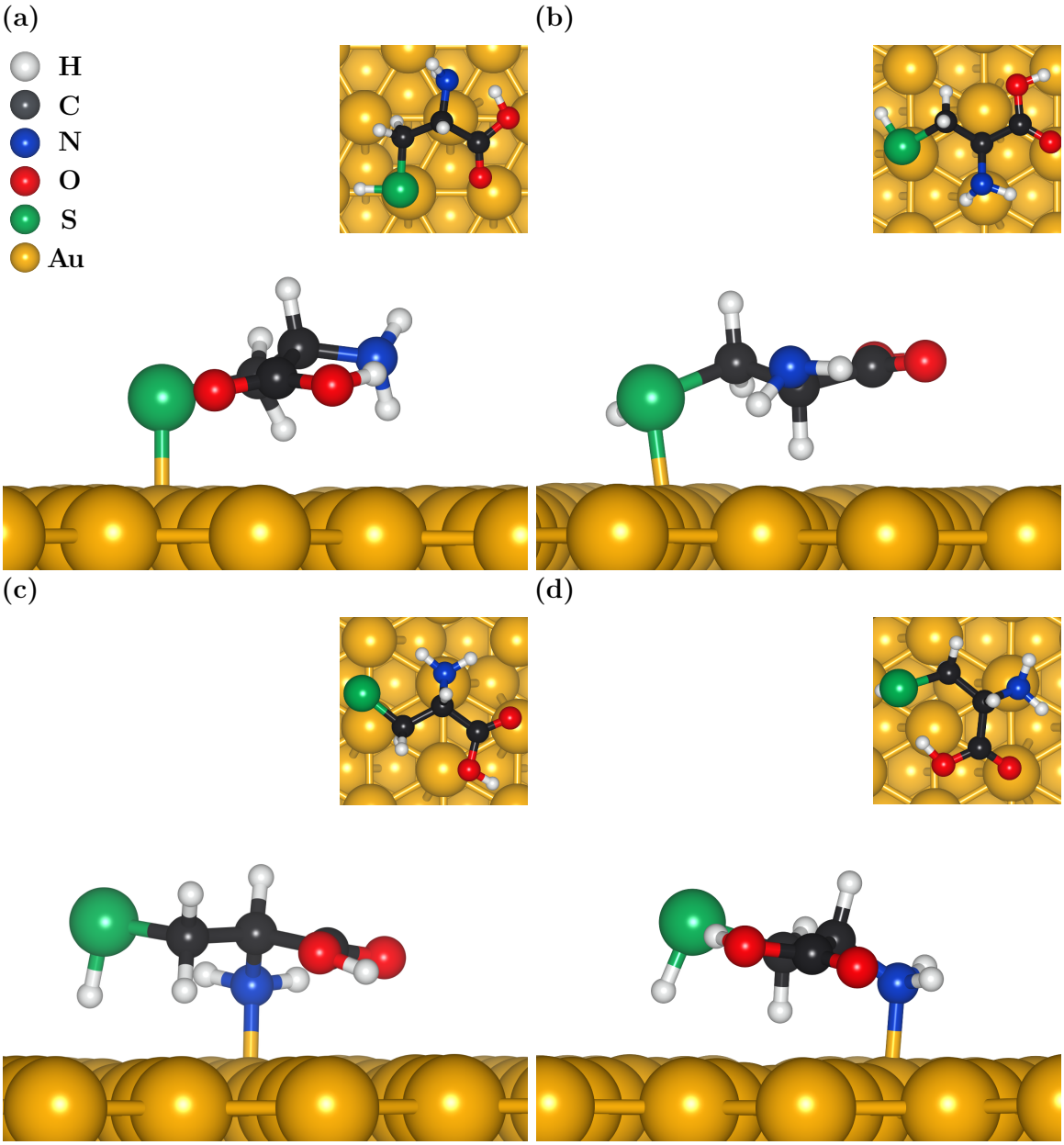

Figure 4.2: Configurations of nonionic cysteine monomer on Au(111) surface. The binding configurations of S–Au bound are displayed in panels **(a)** the most stable, and **(b)** less stable, and of N–Au bound in panels **(c)** the most stable, and **(d)** less stable. For each panel, a side view is displayed with the correspnding aerial view at the up-right corner.

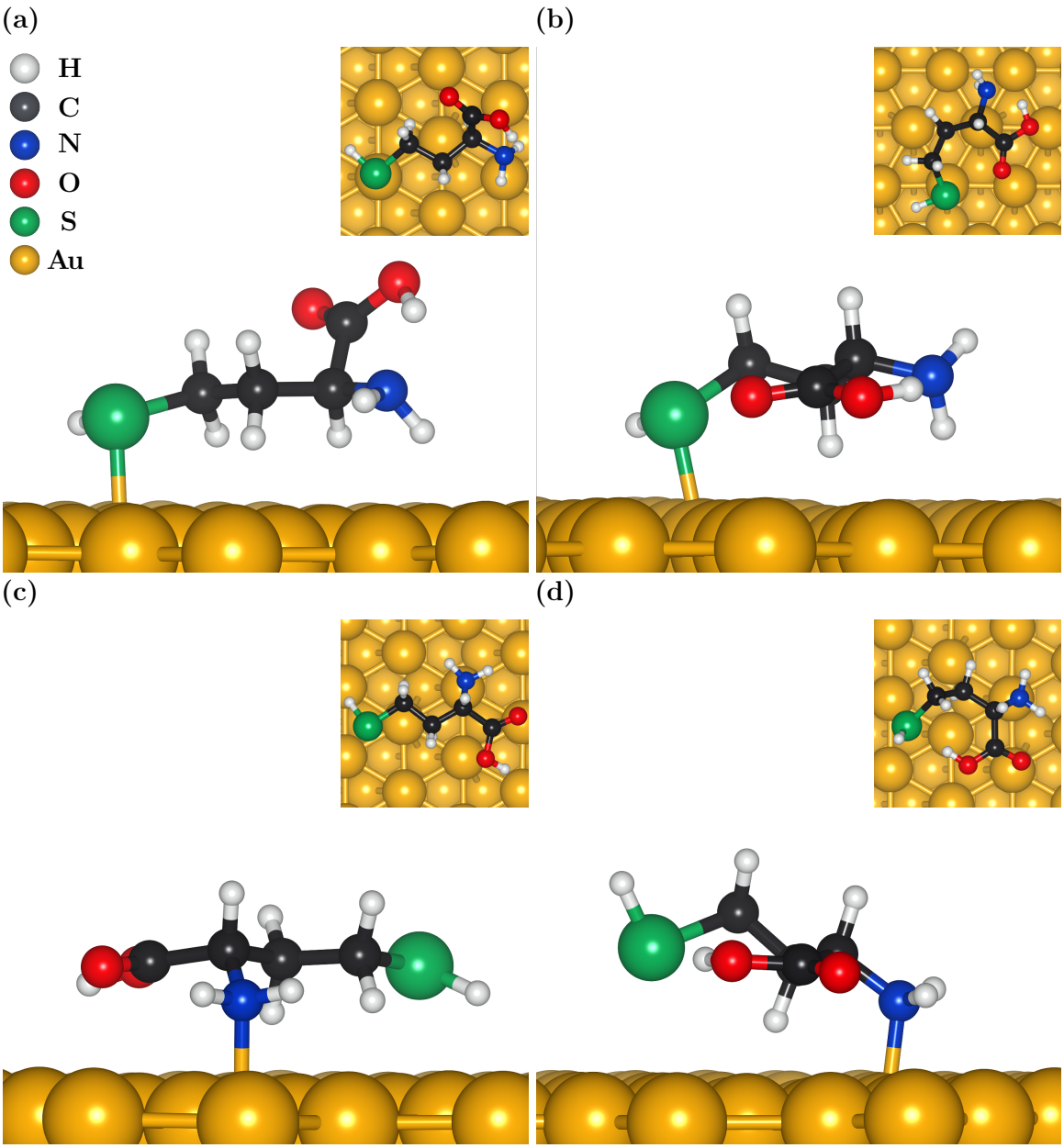

Figure 4.3: Configurations of nonionic homocysteine monomer on Au(111) surface. The panel layout is same as Fig. 4.2.

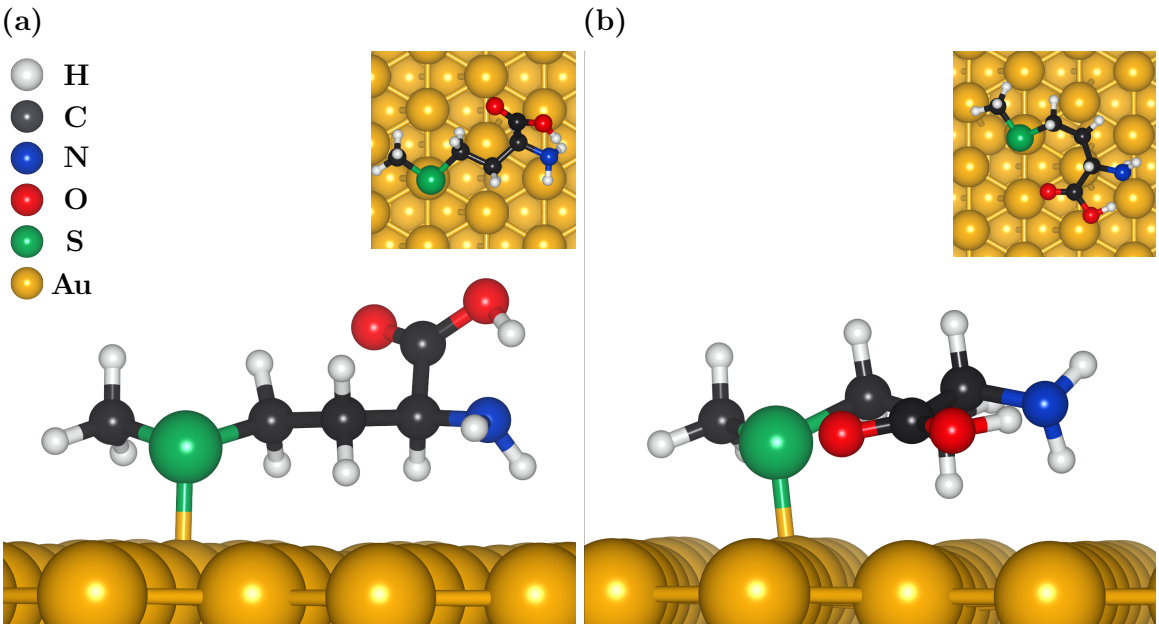

Figure 4.4: Configurations of nonionic methionine monomer on Au(111) surface. The panel layout is same as Fig. 4.2, except no N-Au bound configurations.

Cooperative binding modes for homocysteine and methionine on the Au(111) surface:

Both homocysteine and methionine were able to accommodate efficient binding of both the mercapto (sulfide for methionine) and the amino groups on the surface. This cooperative binding mode (via both S–Au and N–Au bound) was however unstable for cysteine. From cysteine N-bound configurations shown in Fig. 4.2 (c) and (d), the shorter bonding distance of the amino group to the surface causes strain in the hydrocarbon backbone. As a consequence, the mercapto group is lifted further away from the surface, destabilizing this cooperative binding mode. Since the cooperative binding required both the mercapto (sulfide) and the amino groups to interact with the surface, the preferred intramolecular interaction (COOH – NH_2) can not be established in those configurations, as shown in Fig. 4.5. Given the structural similarities of the most stable configurations for cooperative (Fig. 4.5 (a) and (b)) and S–Au bound binding modes (Fig. 4.3 and 4.4 (a)), binding energies for the co-

operative binding modes were slightly lower than the S–Au bound forms as shown in Table 4.2.

Table 4.2: CP corrected binding energies and distances for cooperatively adsorbed homocysteine and methionine on Au(111) surface.

Binding mode[1]	$\Delta E_{b,\mathrm{total}}$	$\Delta E_{b,\mathrm{DFT}}$	$\Delta E_{b,\mathrm{vdW}}$	$d_{\mathrm{S\text{-}Au}}$	$d_{\mathrm{N\text{-}Au}}$	Config. Figure
(S,N)–Au, Hcys	−1.19	−0.29	−0.90	2.63	2.32	4.5 (a)
(S,N)–Au, met	−1.54	−0.47	−1.07	2.58	2.32	4.5 (b)
(S,N)–Au, met	−1.29	−0.26	−1.03	2.55	2.33	4.5 (c)
(S,N)–Au, met	−1.02	+0.08	−1.10	2.62	2.34	4.5 (d)

[1]If not otherwise specified, headings are the same as in Table 4.1.

The most stable cooperative binding mode required an upright orientation of the -COOH group. A surface-parallel orientation of the -COOH group shown in Fig. 4.5 (d) resulted positive ΔE_b(DFT) contribution (see Table 4.2), and the stability of this configuration entirely came from dispersive interaction.

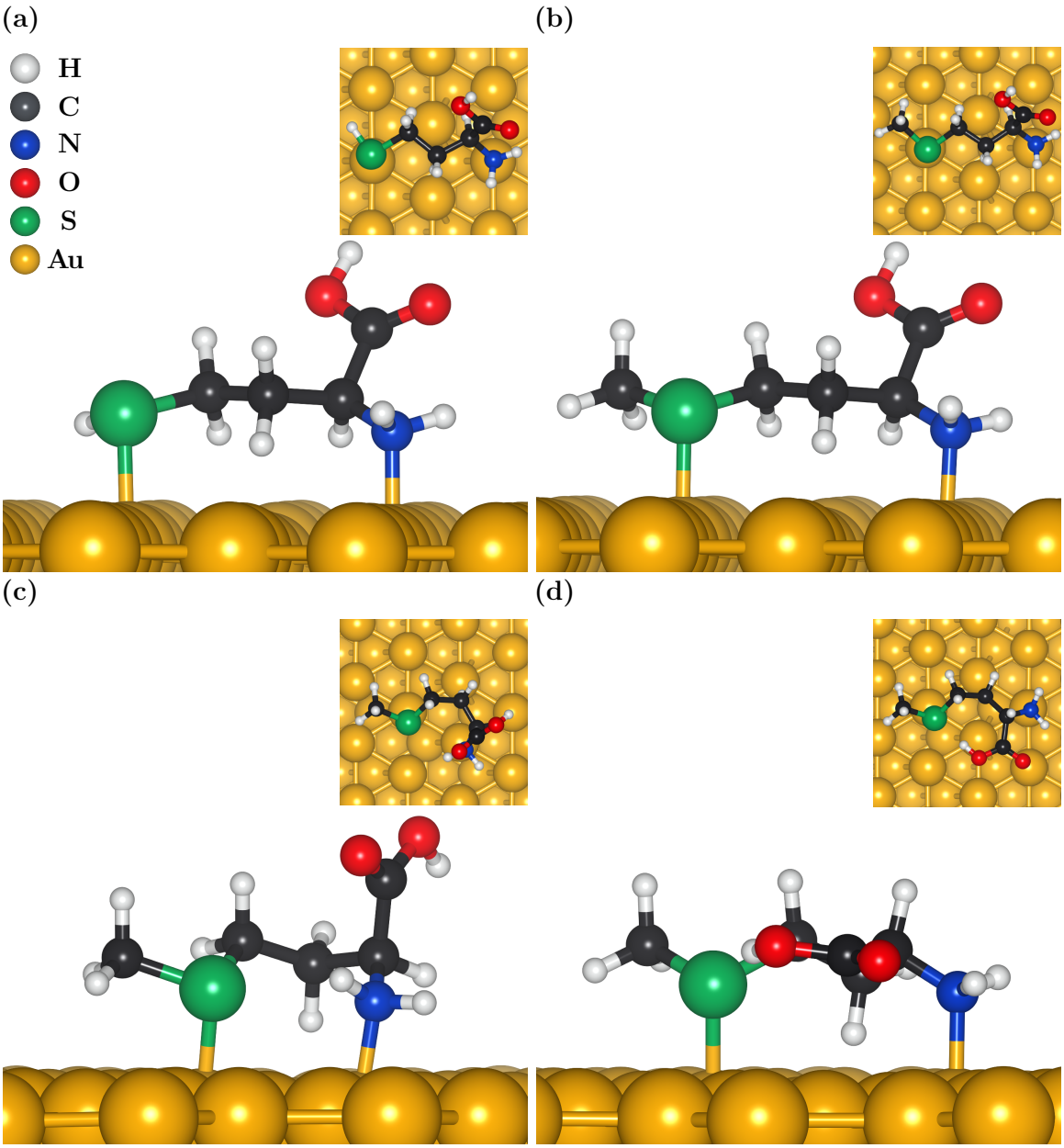

Figure 4.5: Cooperative binding configurations of (a) homocysteine and (b) the most stable methionine monomer on Au(111) surface. The less stable methionine binding configurations in panels (c) and (d).

Unconventional zwitterionic forms of cysteine and homocysteine on the Au(111) surface:

Both conventional (with -NH_3^+ and -COO^- groups) and unconventional (with -NH_3^+ and -S^- groups) zwitterionic structures[118,121] were considered for cysteine and homocysteine monomers on the ideal Au(111) surface. Despite attempts with many input structures, conventional zwitterionic structures underwent proton transfer to reform the nonionic cysteine and homocysteine during the geometry optimization, and stable zwitterionic configurations were unable to obtain for the both AAs. Similar results have also been obtained previously in our group for the AAs on Au(110) surface.[60] Although the pK_a values of -COOH for cysteine and homocysteine (2.1 and 2.2) are significantly lower than the values of -SH (8.2 and 8.9),[266] some lower temperature experimental studies indicate that -SH group acts as the primary proton donor to the -NH_2 group.[118,119,253] Additionally, given XPS experimental evidence of -NH_3^+ and -S^- forms in adsorbed AAs,[90,116,121] we considered unconventional zwitterionic configurations where proton transfer occurred intramolecularly between the -SH and the -NH_2 groups. Two pathways were identified: direct proton transfer and indirect proton transfer. Proton moved directly from the -SH to the -NH_2 group as displayed in Fig. 4.6.

In the second pathway, the -COOH group was involved in mediating the proton transfer as shown in Fig. 4.7 for cysteine and 4.8 for homocysteine. The proton of the -SH group transferred to the -COOH group and triggered the proton of the -COOH group to transfer to the -NH_2 group. Although the vdW dispersive interaction still dominated, cysteine and homocysteine monomers bound relatively strongly on the Au(111) surface via both a single-coordinate S–Au covalent bond and the static Coulombic interaction (-NH_3^+) in unconventional zwitterionic configurations shown in Table 4.3. The more conventional double-coordinate S–Au binding motif was not

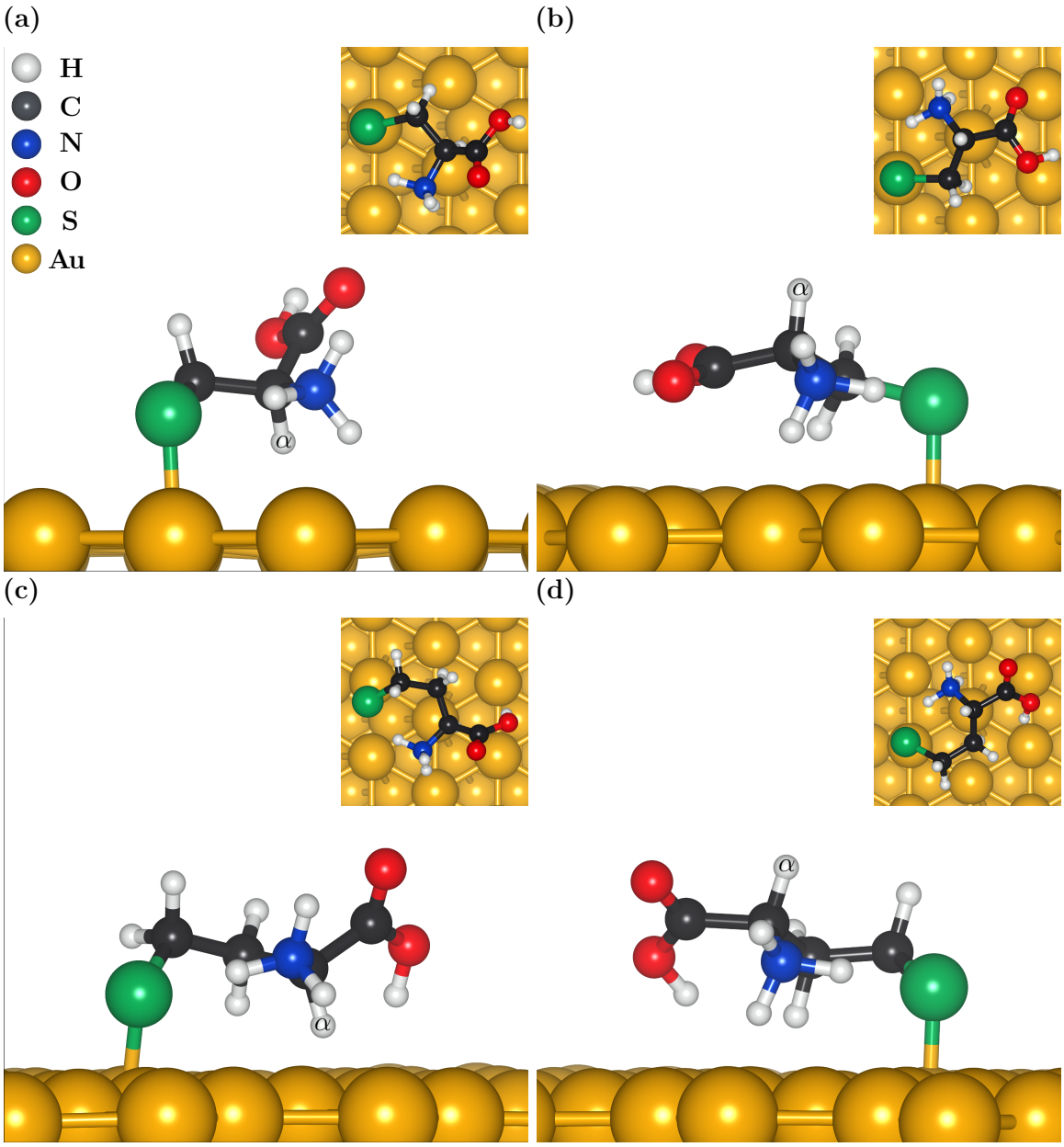

Figure 4.6: Zwitterionic cysteine and homocysteine on Au(111) surface via direct proton transfer. Zwitterionic cysteine was more stable when the H_α is pointing (a) toward the surface than (b) away from the surface. Whereas, zwitterionic homocysteine showed no preferences between the two forms (c) and (d). Energies are given in Table 4.3.

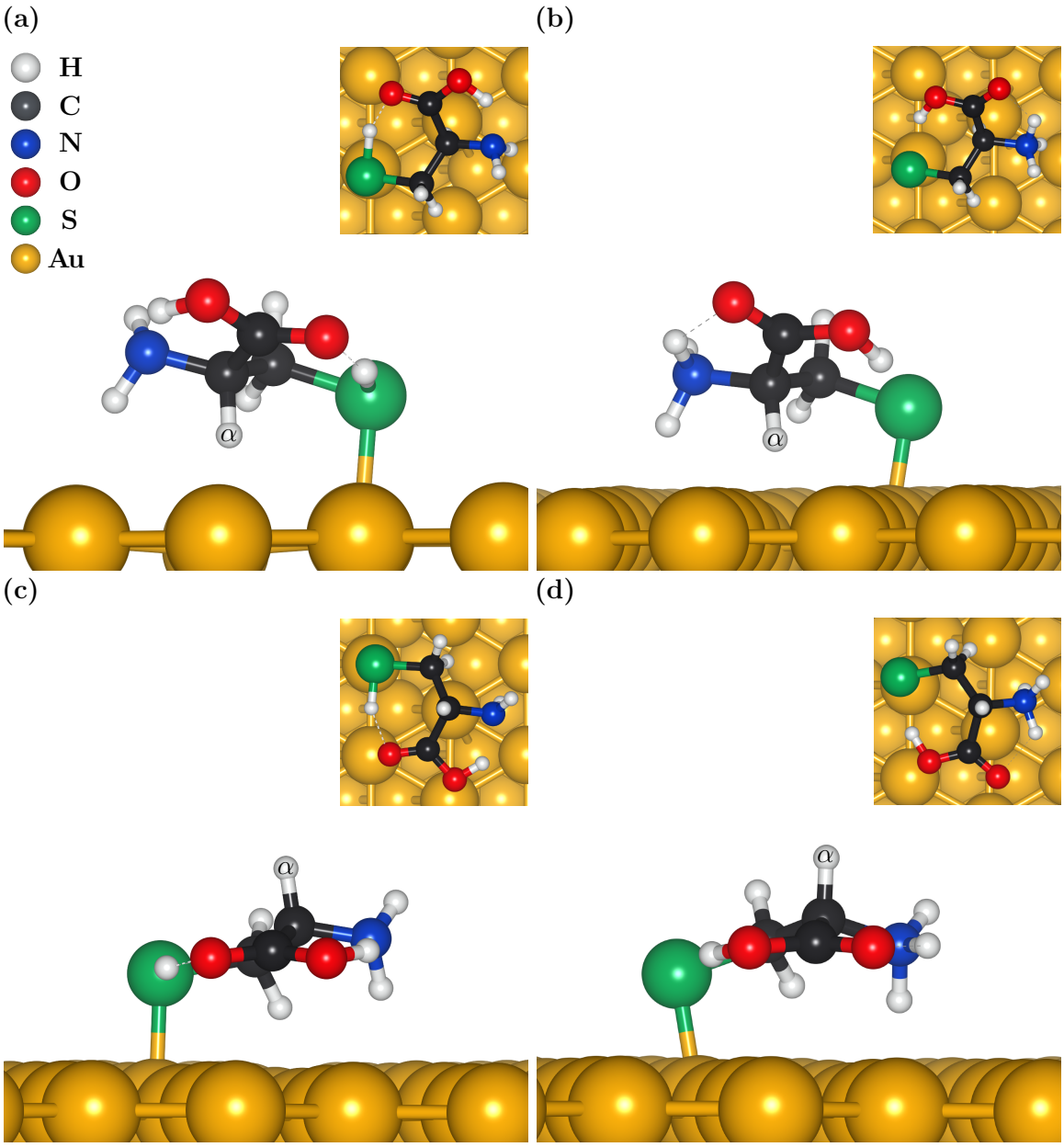

Figure 4.7: Zwitterionic cysteine monomer on Au(111) surface via indirect proton transfer. Panels (a) and (c) showed the configurations before the proton transfer and panels (b) and (d) after the transfer. The configurations with the H_α pointing toward and away from the surface were shown in the top and bottom two panels. The zwitterionic form with the H_α pointing toward the surface was the most stable cysteine binding mode. Energies are given in Table 4.3.

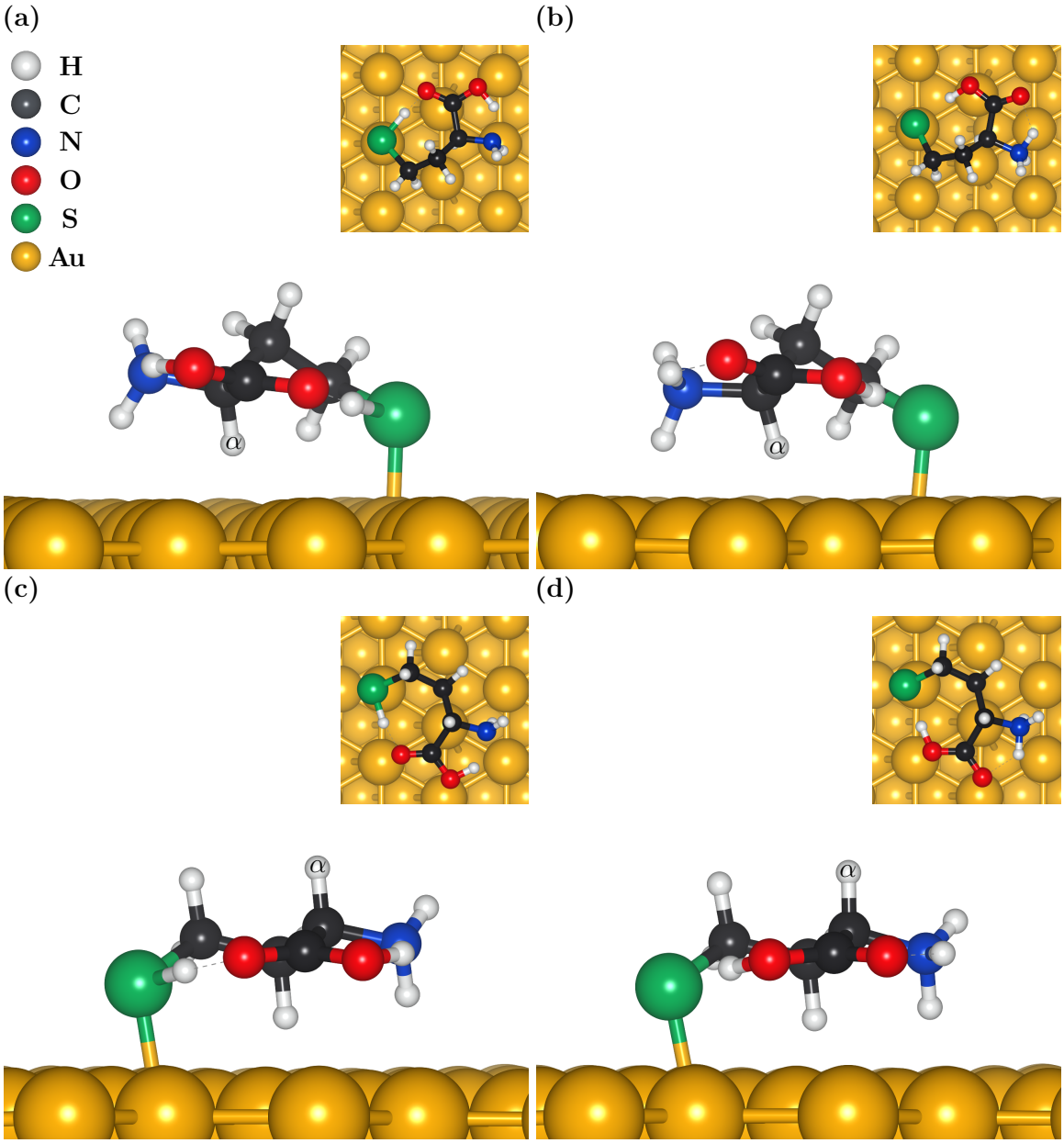

Figure 4.8: Zwitterionic homocysteine monomer on Au(111) surface via indirect proton transfer. The panel layout is same as Fig. 4.7. The zwitterionic form with the H_α pointing toward the surface was the most stable homocysteine binding mode.

Table 4.3: CP corrected binding energies and distances for adsorbed unconventional zwitterionic cysteine and homocysteine on Au(111) surface.

Transfer pathway[1]	$\Delta E_{b,\text{total}}$[2]	$\Delta E_{b,\text{DFT}}$	$\Delta E_{b,\text{vdW}}$	$d_{\text{S-Au}}$	H_α[3]	Config. Figure
direct, cys	−1.27	−0.54	−0.73	2.46	toward	4.6 (a)
direct, cys	−1.12	−0.27	−0.85	2.48	away	4.6 (b)
indirect, cys	−1.06	−0.37	−0.69	2.53	toward	4.7 (a)
indirect, cys	−1.27	−0.53	−0.74	2.47	toward	4.7 (b)
indirect, cys	−0.95	−0.15	−0.80	2.58	away	4.7 (c)
indirect, cys	−1.03	−0.18	−0.85	2.48	away	4.7 (d)
direct, Hcys	−1.23	−0.31	−0.92	2.46	toward	4.6 (c)
direct, Hcys	−1.30	−0.35	−0.95	2.46	away	4.6 (d)
indirect, Hcys	−1.29	−0.43	−0.86	2.51	toward	4.8 (a)
indirect, Hcys	−1.44	−0.55	−0.89	2.46	toward	4.8 (b)
indirect, Hcys	−1.20	−0.33	−0.87	2.52	away	4.8 (c)
indirect, Hcys	−1.23	−0.30	−0.93	2.47	away	4.8 (d)

[1]Proton transfer via either direct pathway (S–H→NH_2) or indirect pathway (S–H→COO–H→NH_2)
[2]If not otherwise specified, headings are the same as in Table 4.1
[3]The H_α points toward or away from the surface.

obtained from geometry optimization even when such structures were used as input geometries.

Despite strong binding strengths of the zwitterionic forms, direct proton transfer was inhibited by the unfavourable orientation of the nitrogen's lone-pair. For nonionic cysteine and homocysteine, low energy configurations were achieved through the involvement of the lone-pair in either H-bonding with the -COOH group, or interaction with the surface. Consequently, indirect proton transfer was preferred because the nonionic configurations met the criterion. AIMD approach can be employed to further elucidate the proton transfer mechanism. Unlike the nonionic forms which had no orientational preferences, unconventional zwitterionic cysteine and homocysteine preferred the H_α points toward the surface, as shown in Table 4.3.

4.3.2 Amino acid dimers in the gas phase

In the gas phase, four distinct intermolecular H-bonding motifs were considered: COOH – COOH, COOH – (NH_2,OH), (NH_2,OH) – (OH,NH_2), and partial charge, as shown in Fig. 4.9. Binding energies for these dimer configurations are presented in Table 4.4. From the table, the most stable configurations for all three AAs in

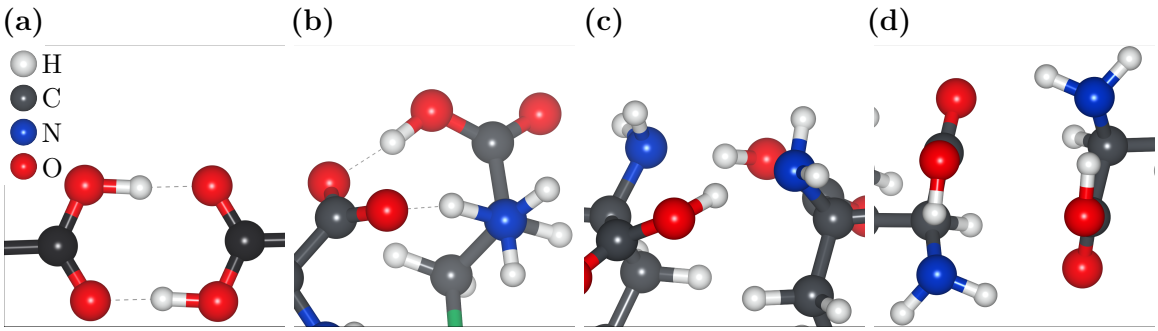

Figure 4.9: Four distinct intermolecular interactions are: (a) COOH – COOH, (b) COOH – (NH_2,OH), (c) (NH_2,OH) – (OH,NH_2) and (d) partial charge between two intramolecular pairs. Only the intermolecular interaction segments are displayed here. Table 4.4 shows the binding energies of the three AA dimers in the gas phase.

Table 4.4: CP corrected binding energies and the corresponding intermolecular interactions for cysteine, homocysteine and methionine dimers in the gas phase.

amino acids	Int.mol.[1]	$\Delta E_{b,\mathrm{Total}}$[2]	$\Delta E_{b,\mathrm{DFT}}$	$\Delta E_{b,\mathrm{vdW}}$
Cysteine	COOH–COOH	−0.56	−0.45	−0.11
	COOH–(NH_2,OH)	−0.43	−0.08	−0.35
	(NH_2,OH)–(OH,NH_2)	—	—	—
	partial charge	−0.15	+0.15	−0.30
Homocysteine	COOH–COOH	−0.39	−0.36	−0.03
	COOH–(NH_2,OH)	−0.26	−0.10	−0.16
	(NH_2,OH)–(OH,NH_2)	−0.30	+0.15	−0.45
	partial charge	−0.48	−0.26	−0.22
Methionine	COOH–COOH	−0.68	−0.55	−0.13
	COOH–(NH_2,OH)	−0.56	−0.23	−0.33
	(NH_2,OH)–(OH,NH_2)	−0.60	+0.08	−0.68
	partial charge	−0.75	−0.40	−0.35

[1]The intermolecular interaction pairs between two amino acids.
[2]Energies are calculated using the same equations as in Table 4.1

the gas phase presented two H-bonds between the carboxylic groups. Partial charge motifs were only slightly higher in energy for homocysteine and methionine dimers due to strong vdW contributions. Although stable conventional zwitterionic motifs were obtained via the COOH – (NH_2,OH) intermolecular interaction for all three AAs in the gas phase (see Fig. 4.9 (b)), their binding energies did not show strong DFT contributions. Unconventional zwitterionic forms were not stable in the absence of a surface. These four distinct binding motifs were then examined on the Au(111) and adatom surfaces.

4.3.3 Amino acid dimers on Au(111)

Two predominant binding motifs were established for AA dimers: the mercapto (or sulfide) groups covalently bind to the surface with intermolecular interaction via H-bonds,[45,51,55,60] and cystine, two cysteines bound covalently via a disulfide bond, interacted the surface via the disulfide group.[171,226,245,257] For the latter binding motif, interactions can be established intramolecularly with the backbone orientating upright, or intermolecularly with other adsorbates, cysteine or cystine. The upright orientation resulted in less stable adsorbate-surface binding interaction, so such binding motif was not shown and discussed here. Due to the surface size limitation, no trimer binding motifs were examined here as well. We examined and focused on the stable dimer binding motifs involving intermolecular interaction via H-bonds. Four distinct intermolecular binding motifs were discussed: COOH – COOH, COOH – (NH_2,OH), (NH_2,OH) – (OH,NH_2) and partial charge.

COOH – COOH interaction:

This intermolecular interaction resulted in relatively stable dimer configurations for all three AAs, as shown in Fig. 4.10 for cysteine and 4.11 for homocysteine and me-

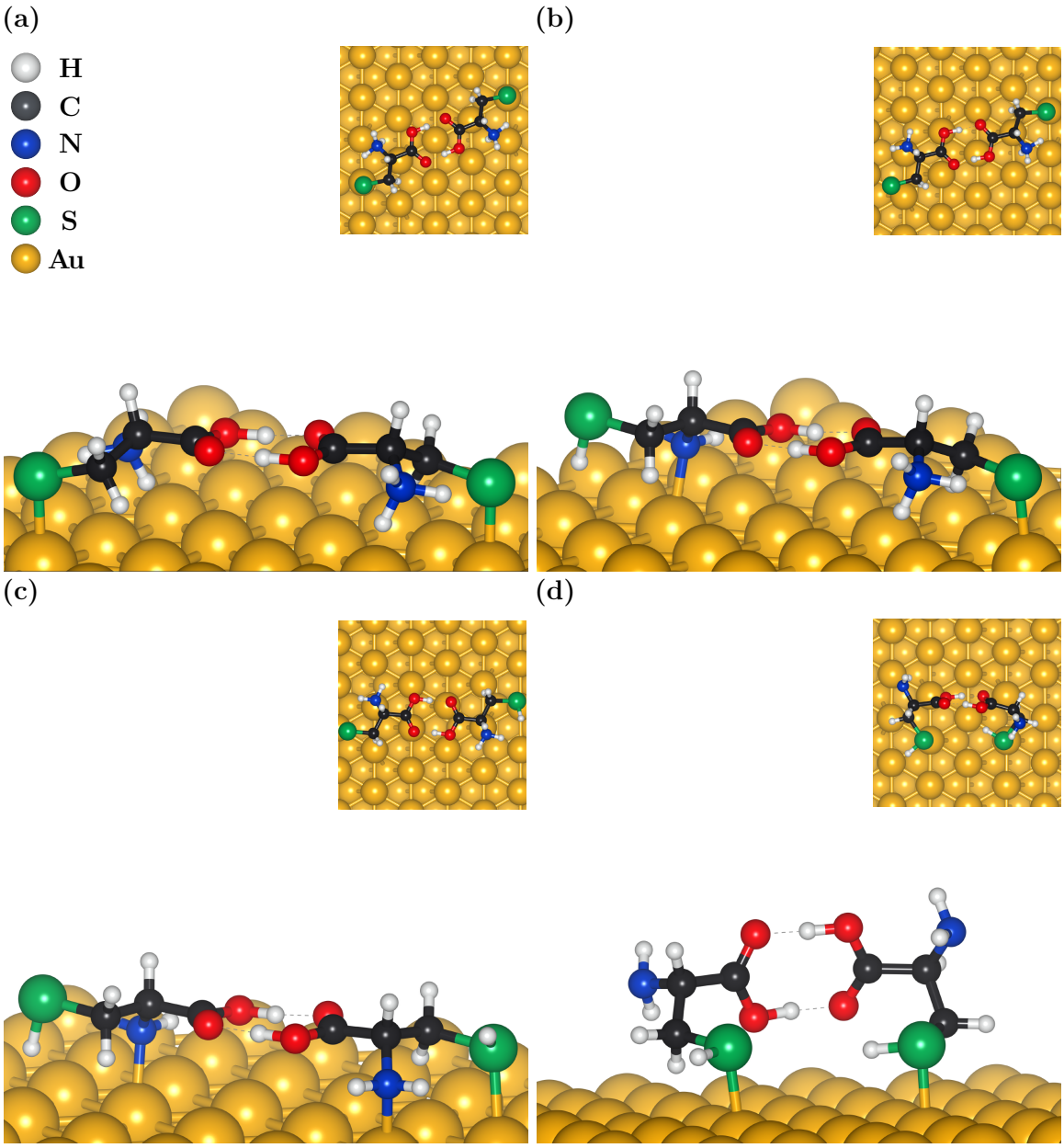

Figure 4.10: Configurations of cysteine dimer on the Au(111) surface with COOH–COOH intermolecular interaction. The most stable configuration is the zwitterionic form with 2 -NH_3^+ groups in panel (a), then with 1 -NH_3^+ group in panel (b). Panel (c) shows the cooperative binding mode, and (d) shows the upright configuration.

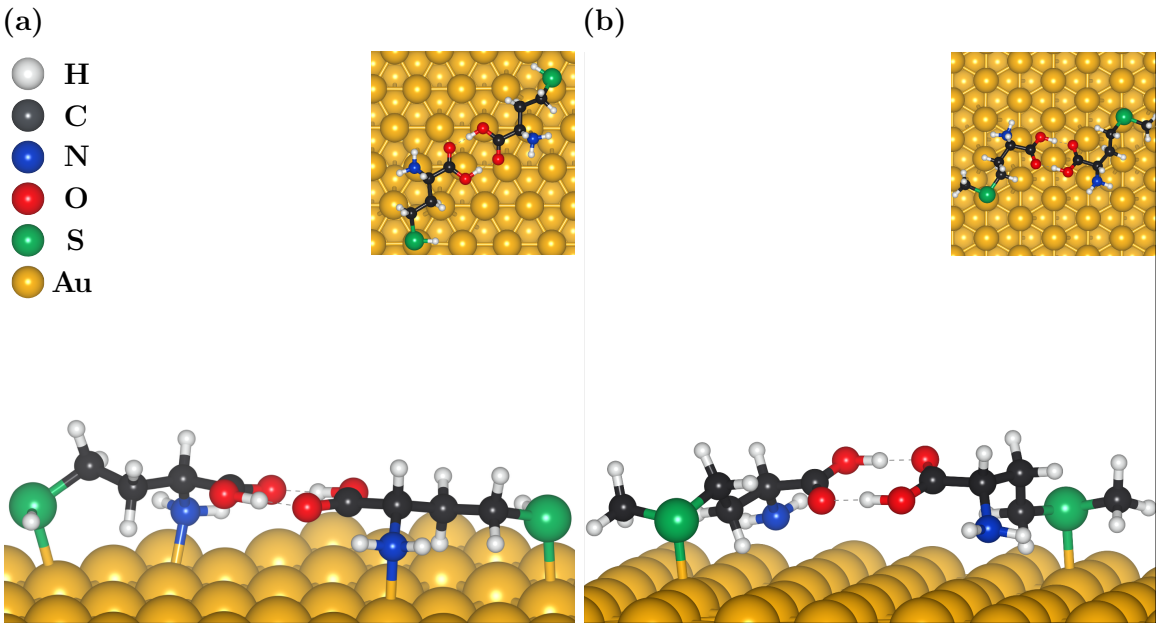

Figure 4.11: Configurations of (a) homocysteine and (b) methionine dimers on Au(111) surface with COOH–COOH intermolecular interaction. Panel (a) shows the cooperative binding mode, and (b) shows the binding mode via 2 S–Au bonds.

thionine. Because the -NH_2 groups no longer involved in intermolecular interaction via H-bonds, they can uptake protons from the -SH groups intramolecularly to form unconventional zwitterionic structures or can interact with the surface to form cooperative binding mode. The zwitterionic configurations were energetically more stable than the nonionic cooperative binding mode for cysteine dimers (see Table 4.5) due to the -NH_3^+ – surface interaction. The binding preference of the zwitterionic form mainly came from the DFT contribution, and the binding energy increment was about 0.1 eV per -NH_3^+ group. Therefore, the (unconventional) zwitterionic form with two -NH_3^+ groups resulted the most stable cysteine dimer configuration on the Au(111) surface. More work has to be done to determine if this binding preference trend is also followed by homocysteine since it can also undergo unconventional zwitterionic formation. For the nonionic flatten binding configurations, the binding energies of the vdW contribution increase by 0.1 eV with additional hydrocarbon backbone (-CH_2-

Table 4.5: CP corrected binding energies and distances for adsorbed cysteine, homocysteine and methionine dimers with COOH – COOH interaction on Au(111) surface.

AA	Binding mode[1]	$\Delta E_{b,\text{total}}$[2]	$\Delta E_{b,\text{DFT}}$	$\Delta E_{b,\text{vdW}}$	$d_{\text{S}_i\text{-Au}}$	$d_{\text{N}_i\text{-Au}}$	Figure
cys.	S–Au, NH_3^+–Au	−1.45	−0.60	−0.85	2.49	—	4.10 (a)
	S–Au, NH_3^+–Au				2.49	—	
	N–Au	−1.35	−0.46	−0.89	—	2.35	4.10 (b)
	S–Au, NH_3^+–Au				2.49	—	
	N–Au	−1.27	−0.39	−0.88	—	2.33	4.10 (c)
	S–Au, N–Au				2.74	2.32	
	S–Au	−0.95	−0.30	−0.65	2.65	—	4.10 (d)
	S–Au				2.61	—	
Hcys.	S–Au, N–Au	−1.40	−0.43	−0.97	2.62	2.36	4.11 (a)
	S–Au, N–Au				2.66	2.37	
met.	S–Au	−1.56	−0.43	−1.13	2.63	—	4.11 (b)
	S–Au				2.66	—	

[1]If not otherwise specified, headings are the same as in Table 4.1.
[2]Binding energies (total, DFT and vdW) are per monomer.

and -CH_3 for homocysteine and methionine) regardless if the cooperative binding mode was established or not. These binding energy increments (per -NH_3^+ and -CH_n) were consistent with the AA monomers on the Au(111) results. The upright orientation was the least stable configuration for the three AAs; an example of the cysteine dimer of such form was shown in Fig. 4.10 (d).

COOH – (NH_2,OH) interaction:

This intermolecular interaction via H-bonds led to conventional zwitterionic formation or nonionic dimer form. A conventional zwitterionic structure is formed when a proton of a -COOH group transfers to a -NH_2 group. Such zwitterionic formation was established intermolecularly when the dimer configurations orientated appropriately as shown in Fig. 4.12. The proton donating -COO^- and accepting -NH_3^+ groups sat flat on the surface, and the -COOH group was in an upright orientation with its proton pointing to the -COO^- group. In general, a zwitterionic form is relatively

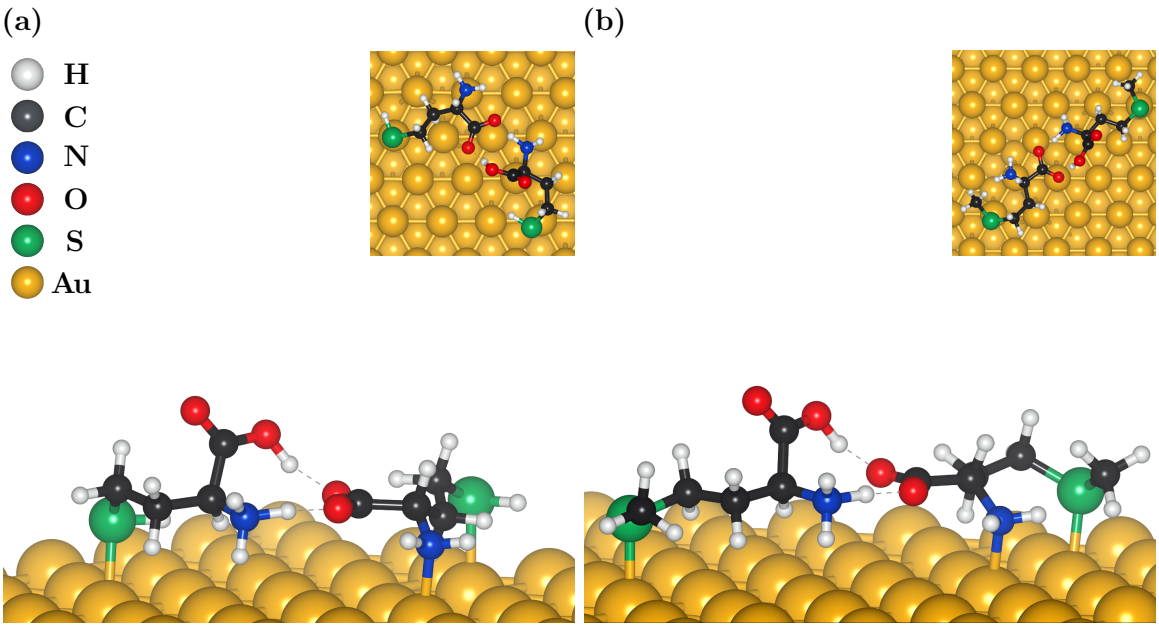

Figure 4.12: Configurations of zwitterionic (a) homocysteine and (b) methionine dimers on the Au(111) surface with COOH – (NH_2,OH) intermolecular interaction.

Table 4.6: CP corrected binding energies and distances for adsorbed cysteine, homocysteine and methionine dimers with COOH – (NH_2,OH) interaction on the Au(111) surface.

AA	Binding mode[1]	$\Delta E_{b,\text{total}}$	$\Delta E_{b,\text{DFT}}$	$\Delta E_{b,\text{vdW}}$	$d_{\text{S}_i\text{-Au}}$	$d_{\text{N}_i\text{-Au}}$	Figure
Hcys.	S–Au, NH_3^+–Au	−1.30	−0.39	−0.91	2.58	—	4.12 (a)
	S–Au, N–Au				2.63	2.33	
met.	S–Au, NH_3^+–Au	−1.66	−0.52	−1.14	2.56	—	4.12 (b)
	S–Au, N–Au				2.58	2.29	
cys.	S–Au, N–Au	−0.97	−0.19	−0.78	2.73	2.32	4.13 (a)
	S–Au				2.75	—	
met.	S–Au	−1.47	−0.33	−1.14	2.58	—	4.13 (b)
	S–Au				2.56	—	

[1]If not otherwise specified, headings are the same as in Table 4.5.

more stable because of the stronger -NH_3^+ – surface interaction, and this relation was established in the case of cysteine dimers via COOH – COOH intermolecular interaction. However, a zwitterionic form was not necessarily more stable than a cooperative binding form. For example, homocysteine dimer configuration with the conventional zwitterionic form (Fig. 4.12 (a)) was slightly less stable than the one

with the cooperative form (Fig. 4.11 (a)). Tables 4.6 and 4.5 showed that the zwitterionic form was 0.1 eV weaker than the cooperative form in terms of the binding energies (−1.30 eV and −1.40 eV respectively). Although this energy difference was arguably insignificant for a DFT-based calculation, the factor causing such binding energy reduction was shown clearly in their configurations. For the zwitterionic form, the 0.1 eV difference came from the vdW contribution due to a -COOH group in an upright orientation. Methionine cannot undergo proton transfer intramolecularly to form an unconventional zwitterionic structure due to the absence of the -SH group. The smallest zwitterionic structure for methionine was the dimer form involving intermolecular proton transfer from a -COOH group to a $-NH_2$ group, as shown in Fig. 4.12 (b). This zwitterionic formation resulted in the most stable methionine dimer configuration (see Table 4.6).

A stable zwitterionic form cannot be established when a dimer structure was not in the specific orientation. As a result, a dimer interacted intermolecularly via H-bonds and remained nonionic, as shown in Fig. 4.13. Their binding energies were generally weaker than the zwitterionic ones and were mainly due to the DFT distribution (see Table 4.6). For example, the nonionic methionine dimer form bounded weaker than its zwitterionic form (−1.47 eV and −1.66 eV in Table 4.6) even though they had significant structural similarities and mainly differed by the orientation of a -COOH group (one sat flat, and one was in an upright orientation).

(NH_2,OH) – (OH,NH_2) motif:

For this motif, no stable conventional zwitterionic forms (with one or two $-NH_3^+$ groups) were obtained from geometry optimization even though many structures were initially inputed as zwitterionic forms. Only nonionic *dimers* were stable, and Fig. 4.14 showed two configurations as examples. Although the *dimers* seemed to

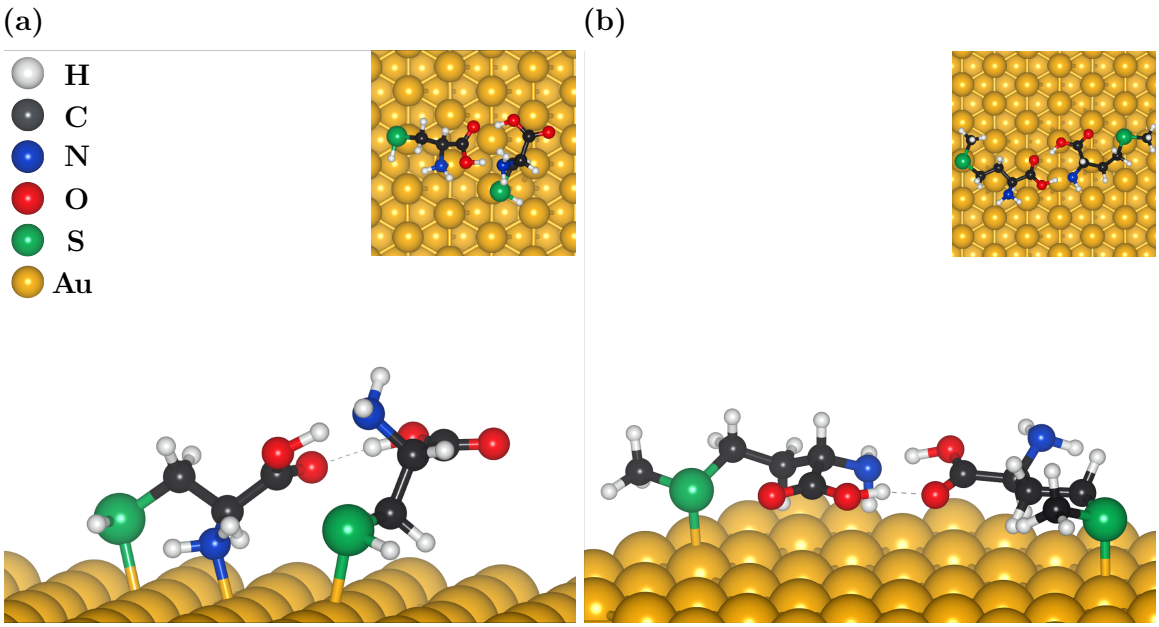

Figure 4.13: Configurations of nonionic (a) cysteine and (b) methionine dimers on the Au(111) surface with COOH – (NH_2,OH) intermolecular interaction.

interact via H-bonds intermolecularly with two -COOH groups in the tilted orientation, their binding energies showed otherwise. The binding energies indicated that the *dimers* were basically two non-interacting monomers (see Table 4.7).

Table 4.7: CP corrected binding energies and distances for adsorbed homocysteine and methionine *dimers* with (NH_2,OH) – (OH,NH_2) binding motif on Au(111) surface.

AA	Binding mode[1]	$\Delta E_{b,\text{total}}$	$\Delta E_{b,\text{DFT}}$	$\Delta E_{b,\text{vdW}}$	$d_{\text{S}_i\text{-Au}}$	$d_{\text{N}_i\text{-Au}}$	Figure
Hcys.	S–Au	−1.17	−0.23	−0.94	2.57	—	4.12 (a)
	S–Au				2.57	—	
met.	S–Au	−1.51	−0.36	−1.15	2.56	—	4.12 (b)
	S–Au				2.56	—	

[1]If not otherwise specified, headings are the same as in Table 4.5.

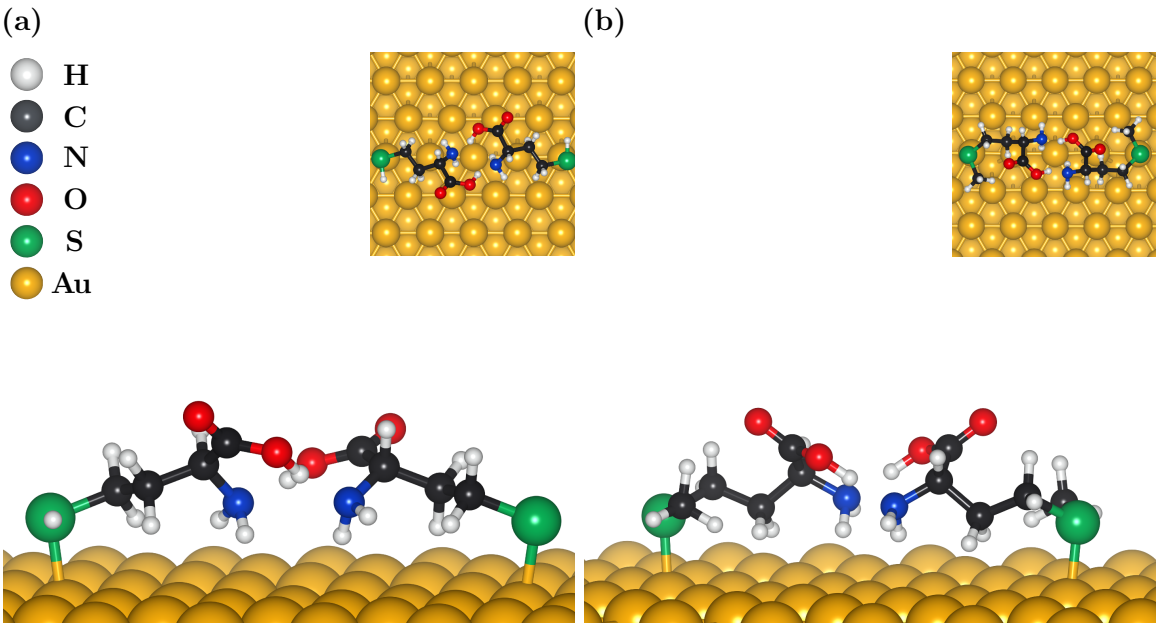

Figure 4.14: Configurations of (a) homocysteine and (b) methionine dimers on the Au(111) surface with (NH_2,OH) – (OH,NH_2) binding motif.

COO^- – (NH_3^+) and partial charge interactions:

A conventional zwitterionic formation can also occur between a -COOH and a -NH_2 group without involving the second -COOH group, as shown in Fig. 4.15 (a). This particular binding configuration was relatively stable with the presence of an unconventional and conventional zwitterionic form. The binding strength was similar to the dimer form that had one unconventional zwitterionic form with COOH – COOH intermolecular interaction (see Fig. 4.10 (b) and Table 4.5).

In the monomer subsections, we established that a nonionic monomer was stabilized by the intramolecular interaction between a -COOH and a -NH_2 group. This stabilization also created a partial charge pair, a slightly negatively charged -$O^{\delta+}$ and a positively charged -$N^{\delta+}$. The partial charge pair led to the intermolecular interaction of a dimer and formed stable homocysteine and methionine dimers in the gas phase (in Fig. 4.9 (d) and Table 4.4). On the Au(111) surface, this binding motif was relatively stable (see Table 4.8), and the upright orientation of the -COOH or

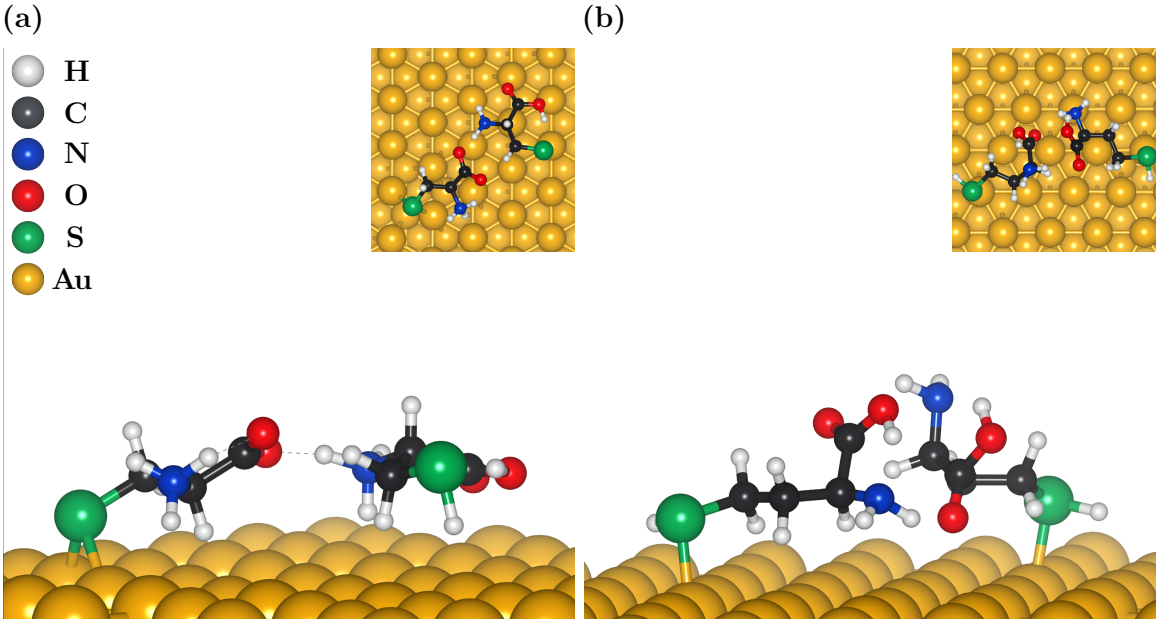

Figure 4.15: Configurations of (a) zwitterionic cysteine dimer and (b) nonionic homocysteine dimer interacting intermolecularly via partial charge on the Au(111) surface.

Table 4.8: CP corrected binding energies and distances for adsorbed zwitterionic cysteine dimer and nonionic homocysteine dimer with partial charge interaction on the Au(111) surface.

AA	Binding mode[1]	$\Delta E_{b,\text{total}}$	$\Delta E_{b,\text{DFT}}$	$\Delta E_{b,\text{vdW}}$	$d_{\text{S}_i\text{-Au}}$	$d_{\text{N}_i\text{-Au}}$	Figure
cys.	S–Au_2, NH_3^+–Au	−1.34	−0.49	−0.85	(2.57,2.52)	—	4.15 (a)
	NH_3^+–Au				—	—	
Hcys.	S–Au	−1.21	−0.30	−0.91	2.60	—	4.15 (b)
	S–Au				2.62	—	

[1]If not otherwise specified, headings are the same as in Table 4.5.

the -NH_2 groups (see Fig. 4.15 (b)) did not penalize more than 0.1 eV on both DFT and vdW contributions.

4.3.4 AA monomers on an adatom defect gold surface

The adatom defect surface model had a single gold atom sitting on top of the Au(111) surface with a coordination number 3 or 4 depending on whether the adatom located on the fcc, hcp or the bridge site respectively. Binding was strengthened when the adatom was involved in the binding events. Stabilizing the reactive adatom by forming a more stable adsorbate-adatom complexes resulted in more substantial binding energies. Moreover, the binding energy enhancement was only included in the uncorrected DFT method, $E_{b,\mathrm{DFT}}$, whereas the dispersive binding energy, $E_{b,\mathrm{vdW}}$ remained relatively unchanged.

Binding strengths on the adatom surface were unchanged when the adatom was far from the adsorption site. When binding events involved the adatom, either the mercapto and the amino group interacted with it forming three distinct binding modes: the unconventional zwitterionic structures (for cysteine and homocysteine), the nonionic cooperative binding and the nonionic single bindings.

The unconventional zwitterionic monomer forms of cysteine and homocysteine on the adatom surface:

Similar to the trend of the binding strengths of the AAs on the Au(111) surface, the unconventional zwitterionic structures formed one of the strongest binding interactions for cysteine and homocysteine on the adatom surface. The participation of the adatom enhanced the total binding energies of the adsorbed zwitterionic cysteine and homocysteine monomer for the direct proton transfer (see Table 4.9) by 0.5 eV (from -1.27 eV to -1.79 eV) and 0.7 eV (from -1.30 eV to -2.03 eV) with respect to the monomers on the Au(111) surface. For the indirect proton transfer, the enhancements were 0.5 eV (from -1.27 eV to -1.80 eV) for cysteine and 0.4 eV (from -1.44 eV to -1.79 eV) for homocysteine. Besides the total binding energy enhancements, the

Table 4.9: CP corrected binding energies and distances for adsorbed unconventional zwitterionic cysteine and homocysteine on the adatom surface.

Transfer pathway[1]	$\Delta E_{b,\text{total}}$	$\Delta E_{b,\text{DFT}}$	$\Delta E_{b,\text{vdW}}$	$d_{\text{S-ad}}$[2]	$d_{\text{S-Au}}$[3]	Config. Figure
direct, cys	−1.79	−1.02	−0.77	2.58	—	4.16 (a)
direct, cys	−1.58	−0.77	−0.81	2.47	2.59	4.16 (b)
indirect, cys	−1.80	−1.16	−0.64	2.37	—	4.17 (a)
indirect, cys	−1.59	−0.79	−0.80	2.39	—	4.17 (b)
direct, Hcys	−2.03	−1.33	−0.70	2.38	—	4.16 (c)
direct, Hcys	−1.59	−0.56	−1.02	2.44	2.56	4.16 (d)
indirect, Hcys	−1.79	−0.94	−0.85	2.38	—	4.17 (c)

[1]If not otherwise specified, headings are the same as in Table 4.3.
[2]The bond length between the sulfur and the adatom (abbreviated as ad).
[3]The bond length between the sulfur and a gold atom of the Au(111) surface.

adatom also allowed two stable binding modes via a single-coordinate S–adatom bond (see Fig. 4.16 (a) and (c), and Fig. 4.17) or via a double-coordinate Au–S–adatom bond (panels (b) and (d)). Binding energy contributions were distributed differently for the two binding modes, via a single- and a double-coordinate bond. For the binding mode via a double-coordinate bond involving the adatom and the surface, the vdW binding contributions dominated the total binding energies, as shown in Table 4.9. In contrast, the DFT binding energies were the dominant contributions for the binding modes via a single-coordinate bond involving only the adatom. The primary factor of the enhancement was accompanied by shorter S–adatom bond lengths, as shown in Table 4.9; the bonds were shortened by about 0.07 Å to 0.10 Å on average (compare to the average bond lengths of S–Au(111), 2.48 Å and 2.49 Å). Disregard of the adatom involvement and the binding modes, the vdW binding energies remained in similar contributions for the adsorbed zwitterionic AAs on the Au(111) and adatom surfaces.

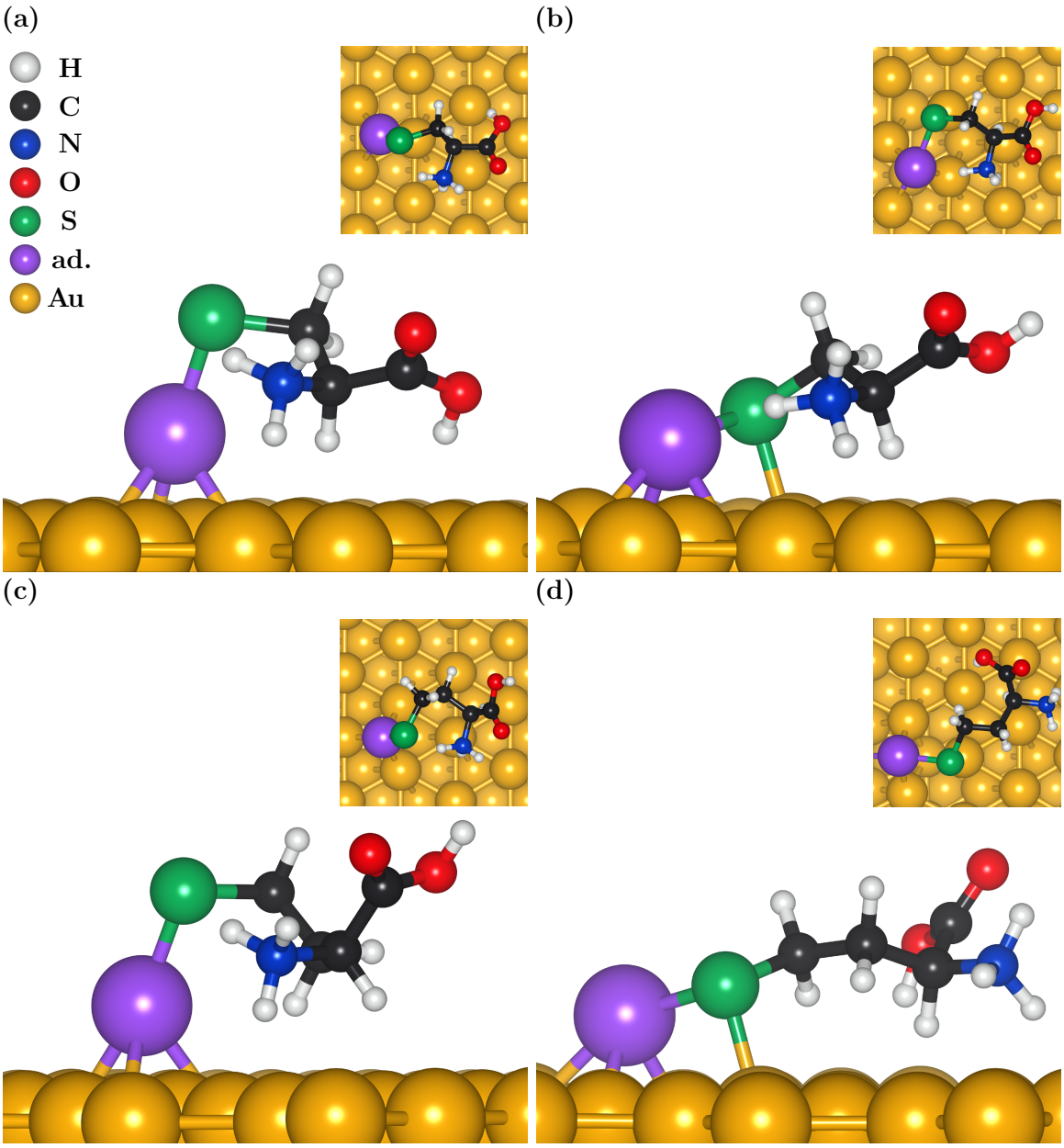

Figure 4.16: Configurations of the unconventional zwitterionic cysteine and homocysteine monomers on the adatom surface via direct proton transfer. Panels (a) and (c) show the binding modes of cysteine and homocysteine on the adatom via a single-coordinate bond, and panels (b) and (d) show the binding modes via a double-coordinate bond.

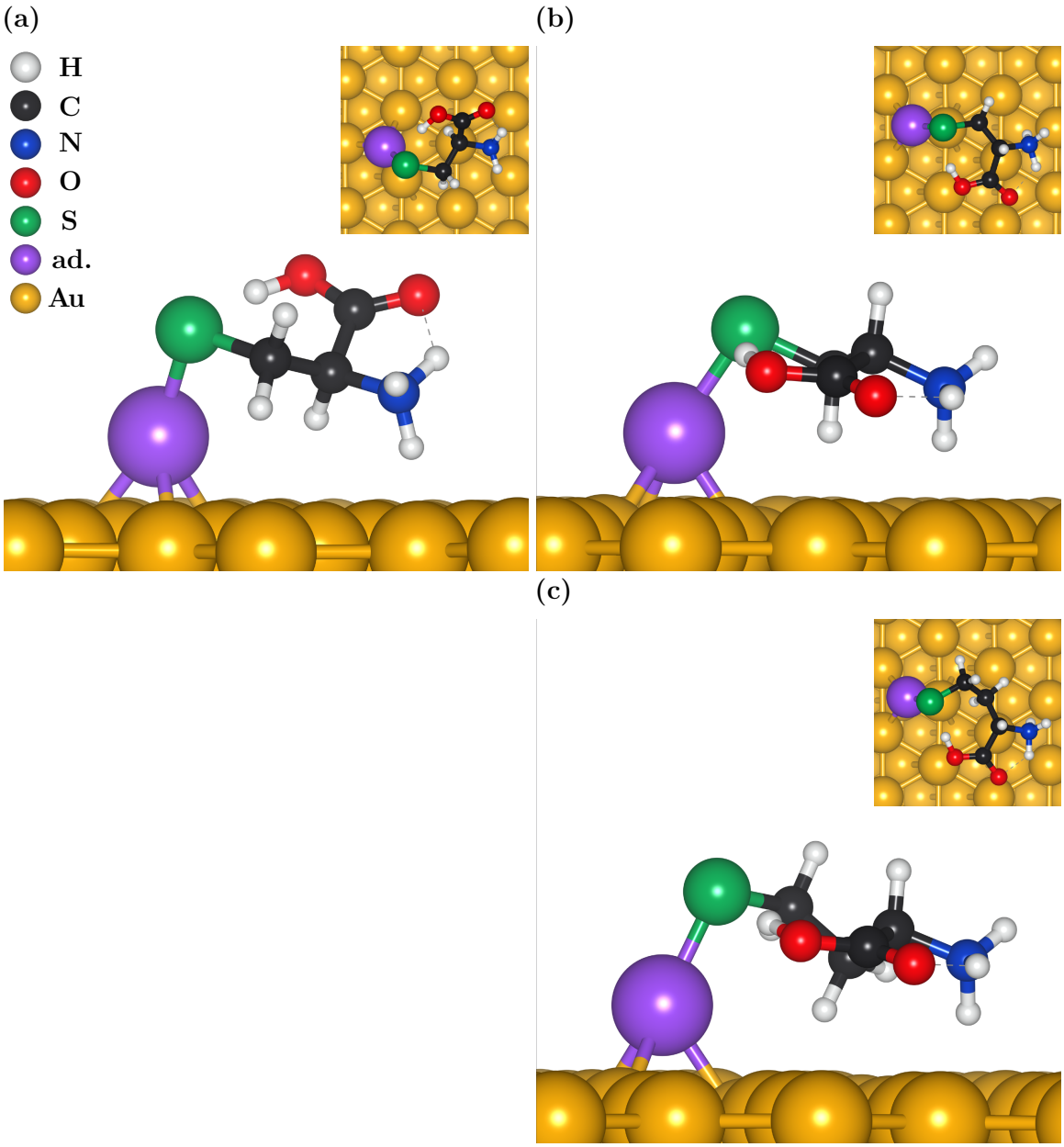

Figure 4.17: Configurations of the unconventional zwitterionic cysteine and homocysteine monomers on the adatom surface via indirect proton transfer. Panels (a) and (b) show the binding modes of cysteine on the adatom via a single-coordinate bond with the H_α pointing toward and away from the surface. Panel (c) shows that homocysteine binds to the adatom via a single-coordinate bond with the H_α pointing away from the surface.

Cooperative binding modes for the sulfur-containing amino acids on the adatom surface:

Two distinct cooperative binding modes had been optimized here: the S–adatom and N–surface and the N–adatom and S–surface cooperative bindings. Given the elevation of the adatom, the cooperative binding mode was achieved for the nonionic cysteine monomer. Whereas such a binding mode was not stable on the Au(111) surface due to the stress of the hydrocarbon backbone, as discussed in subsection 4.3.1. The binding modes of the mercapto (or sulfide) group binded to the adatom while the amino group interacted with the surface were displayed in the panels (a) of Figs. 4.18, 4.19 and 4.20 for cysteine, homocysteine and methionine respectively. Panel (b) in the same figures displayed that the amino group binded to the adatom while the mercapto (or sulfide) group interacted with the surface.

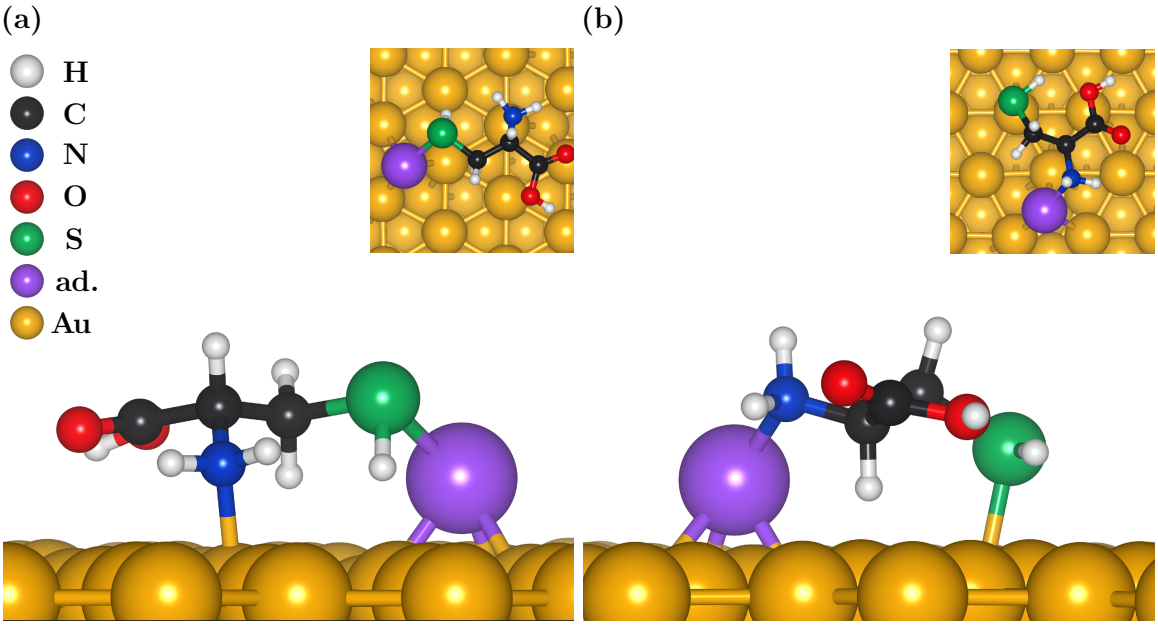

Figure 4.18: Cooperative binding mode of nonionic cysteine monomer with the mercapto group binding to the adatom in panel (a) and with the amino group binding to the adatom in panel (b).

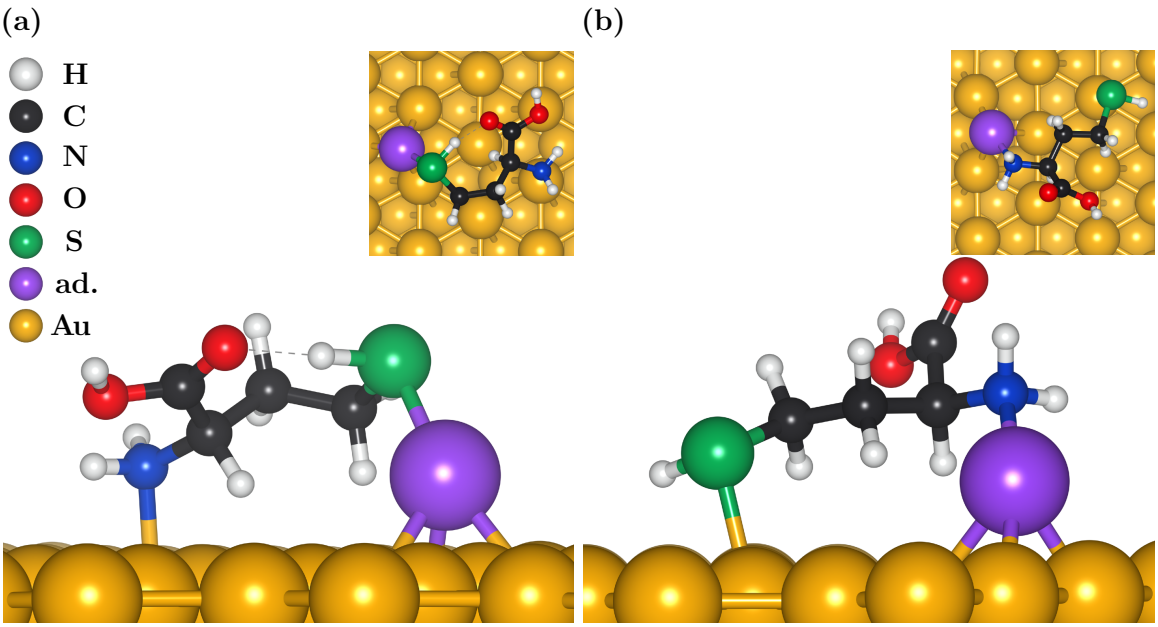

Figure 4.19: Cooperative binding mode of nonionic homocysteine monomer with the mercapto group binding to the adatom in panel (a) and with the amino group binding to the adatom in panel (b).

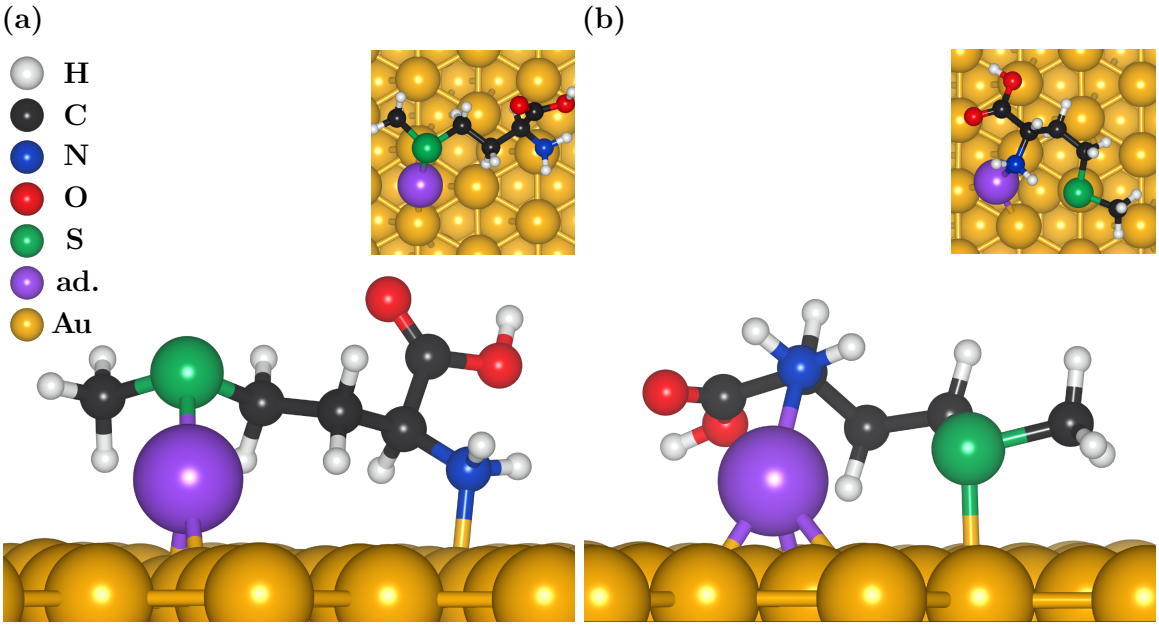

Figure 4.20: Cooperative binding mode of nonionic methionine monomer with the sulfide group binding to the adatom in panel (a) and with the amino group binding to the adatom in panel (b).

The binding strengths for the cooperative binding modes (see Table 4.10) were moderate and weaker than the zwitterionic binding modes due to the -NH_3^+ group's absence. The DFT binding energy contributions were altered while the vdW contributions remained unchanged for the two binding modes. Binding strengths of the

Table 4.10: CP corrected binding energies and distances for cooperatively adsorbed amino acids on the adatom surface.

Binding mode[1]	$\Delta E_{b,\text{total}}$	$\Delta E_{b,\text{DFT}}$	$\Delta E_{b,\text{vdW}}$	$d_{\text{S-surf}}$[2]	$d_{\text{N-surf}}$[3]	Config. Figure
S–ad, N–Au, cys	−1.32	−0.31	−1.01	2.52	2.37	4.18 (a)
N–ad, S–Au, cys	−1.25	−0.37	−0.88	2.62	2.45	4.18 (b)
S–ad, N–Au, Hcys	−1.51	−0.68	−0.83	2.45	2.38	4.19 (a)
N–ad, S–Au, Hcys	−1.51	−0.63	−0.88	2.65	2.23	4.19 (b)
S–ad, N–Au, met	−1.91	−0.83	−1.08	2.43	2.33	4.20 (a)
N–ad, S–Au, met	−1.87	−0.69	−1.18	2.64	2.22	4.20 (b)

[1]If not otherwise specified, headings are the same as in Table 4.1.
[2]The bond length between the sulfur and the adatom (abbreviated as ad) or the Au(111) surface (denoted as Au).
[3]The bond length between the nitrogen and the adatom (abbreviated as ad) or the Au(111) surface (denoted as Au).

vdW contributions were independent from the relative orientation of the carboxylic group to the surface, as shown in Table 4.10. Comparing the binding energies of homocysteine and methionine with the cooperative binding modes on the Au(111) and the adatom surface, the total binding energies were enhanced by 0.3 eV for homocysteine (−1.19 eV vs −1.51 eV) and 0.4 eV for methionine (−1.54 eV vs −1.91 eV).

Binding modes with single-coordinate bonds:

Since orientational preferences were not obvious for the binding modes with single-coordinate bonds, only the forms with the H_α pointing upward were presented in Figs. 4.21, 4.22 and 4.23 for cysteine, homocysteine and methionine respectively.

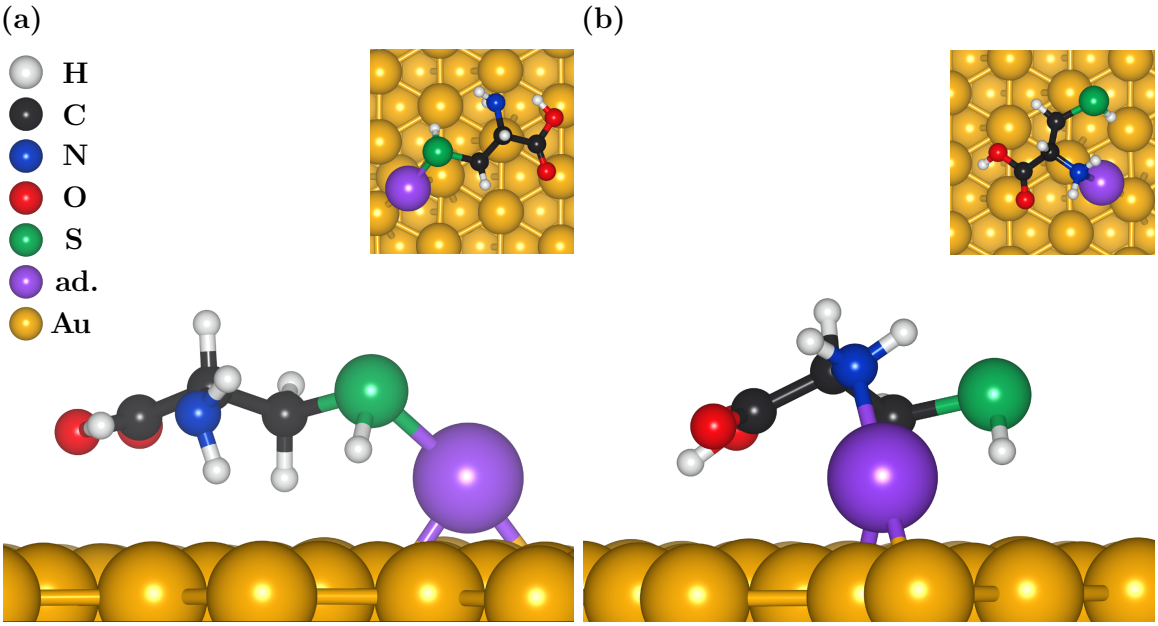

Figure 4.21: Configurations of nonionic cysteine on adatom surface via (a) S–adatom and (b) N–adatom single-coordinate bonds.

Similar to other two adatom involving binding modes, the adatom enhanced the binding strengths of the single-coordinate binding modes via the S–adatom and the N–adatom bonds, as shown in Table 4.11. The enhancement was mainly on the DFT contributions by more than 0.3 eV (−0.04 eV vs −0.35 eV for cysteine) while the dispersive binding energies remained in similar strengths as the amino acids binded on the Au(111) surface. In terms of binding strengths, the single-coordinate binding modes had similar total binding energies as the cooperative binding modes for the three AAs (compare Table 4.11 and 4.10).

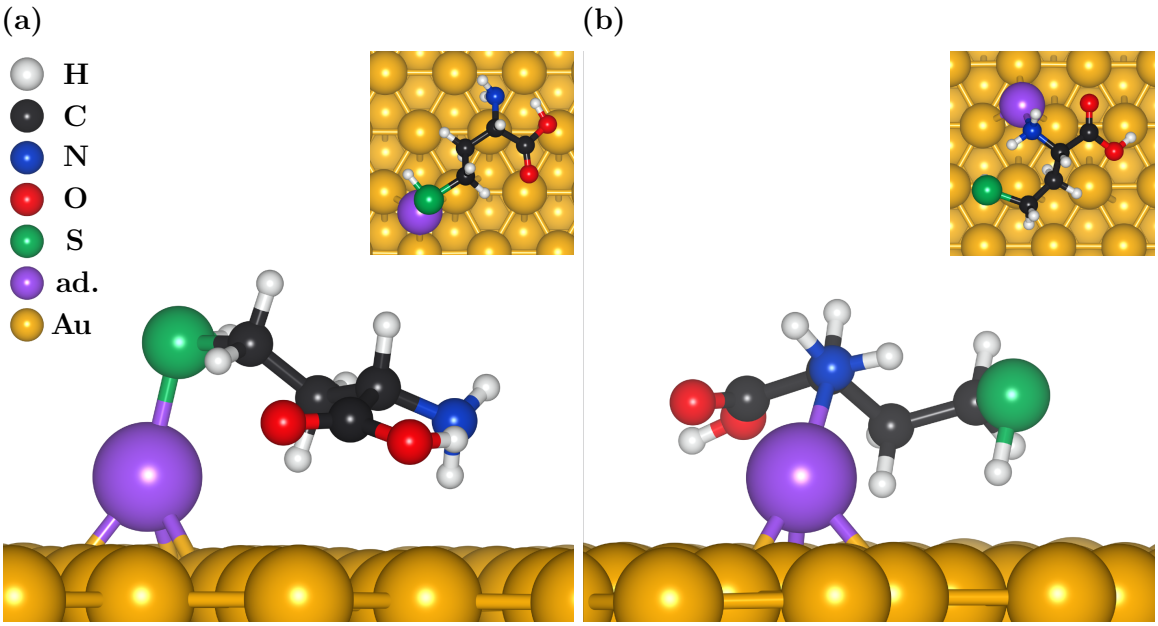

Figure 4.22: Configurations of nonionic homocysteine on adatom surface via (a) S–adatom and (b) N–adatom single-coordinate bonds.

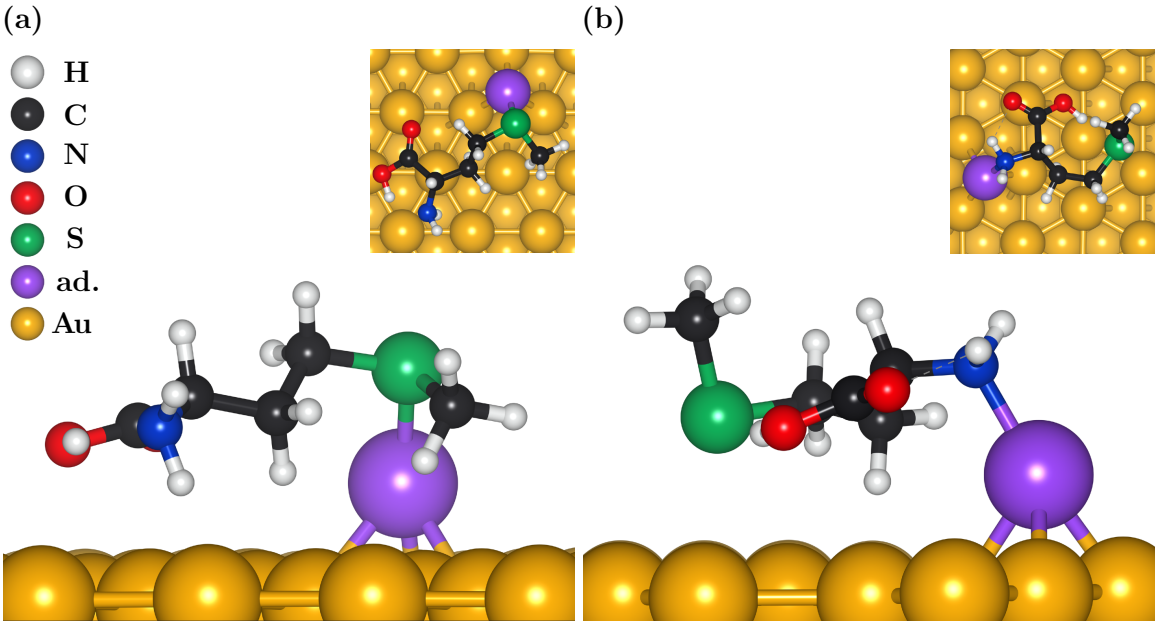

Figure 4.23: Configurations of nonionic methionine on adatom surface via (a) S–adatom and (b) N–adatom single-coordinate bonds.

Table 4.11: CP corrected binding energies and distances for adsorbed nonionic amino acids on the adatom surface.

Binding mode[1]	$\Delta E_{b,\text{total}}$	$\Delta E_{b,\text{DFT}}$	$\Delta E_{b,\text{vdW}}$	$d_{\text{S-ad}}$[2]	$d_{\text{N-ad}}$[3]	Config.	Figure
S–ad, cys	−1.24	−0.35	−0.89	2.48	—		4.21 (a)
N–ad, cys	−1.34	−0.40	−0.94	—	2.21		4.21 (b)
S–ad, Hcys	−1.41	−0.69	−0.72	2.43	—		4.22 (a)
N–ad, Hcys	−1.48	−0.55	−0.93	—	2.21		4.22 (b)
S–ad, met	−1.78	−0.78	−1.00	2.42	—		4.23 (a)
N–ad, met	−1.46	−0.45	−1.01	—	2.21		4.23 (b)

[1]If not otherwise specified, headings are the same as in Table 4.1.
[2]The bond length between the sulfur and the adatom (abbreviated as ad).
[3]The bond length between the nitrogen and the adatom (abbreviated as ad).

Binding energy for the S–adatom and the N–adatom binding modes were not significantly different for cysteine and homocysteine, as shown in Table 4.11. For methionine, the binding energy of the S–adatom binding mode was 0.3 eV stronger than the N–adatom mode, and the difference was all due to the DFT contribution. In terms of the configurations, the methyl group of the sulfide pointed upward away from the surface, an orientation which slightly lowered the dispersive binding strength.

4.4 Conclusion

In the present work, we investigated the binding behaviours, the binding strengths and the binding configurations of the three sulfur-containing amino acids, *L*-cysteine, *L*-homocysteine and *L*-methionine on the Au(111) with the implementation of the vdW dispersion using TS formalism. This implementation also provided a way to estimate the binding energies of the vdW dispersive interaction. We first pursued a molecular-level understanding of the effects of the surface adatom on the molecule-surface interaction, and then the effects of the intermolecular interaction in the dimer forms.

The binding modes and configurations of cysteine, homocysteine and methionine monomers on the Au(111) surface were studied as the references. We found that only the unconventional zwitterionic forms (-S^- and -NH_3^+) of cysteine and homocysteine and the cooperative binding modes presented stable binding structures. The proposed (direct and indirect) proton transfer pathways could be experimental examined by using cysteine (or homocysteine) with deuterium attaching to the sulfur (-SD). At a low surface coverage scenario, if the deuterium is found attaching to the carboxylic (-COOD) or the amino (-NH_2D^+) group, then the proposed proton transfer mechanism can be proved indirectly. The nonionic monomers with single-coordinate bonds interacted weakly on the Au(111) surface, and the vdW dispersion was the predominant interaction. With the presence of the adatom, overall binding strengths were enhanced significantly for the three amino acids. Additionally, a stable cooperative binding mode of cysteine was formed in the presence of the adatom; whereas such binding mode created too much stress on the hydrocarbon backbone and became unstable on the ideal Au(111) surface.

The intermolecular interactions of the three amino acids were investigated on the Au(111) surface. Dimerization also enhanced the overall binding strengths due to stronger vdW dispersive interaction. For cysteine and homocysteine, both unconventional and conventional (-COO^- and -NH_3^+) zwitterionic structures had similar binding strengths on the Au(111) surface. No orientational preferences have been found for the three nonionic amino acids on the two surfaces. However, the preferences can have occurred for the dimers on the adatom surface; further work has to be done for this investigation.

Chapter 5

Atomic Layer Deposition on a Silicon Oxide Surface

5.1 Introduction

A primary advantage of the catalytic ALD is that the catalytic reaction opens an alternative reaction pathway that has a lower activation energy barrier(s), so the deposition can be performed at lower temperatures. The current understanding is that the catalyst weakens a hydrogen-oxygen bond on the silicon oxide surface, so that a nearby silicon precursor ($SiCl_4$ is used for the example case shown in Fig. 5.1) can chemically bind to the substrate with lower activation energy. Once the Si–O bond is formed, the precursor undergoes inversion which weakens a Si–Cl bond. This Cl then interacts with the proton on the catalyst and becomes a byproduct, HCl. The byproduct is purged and removed in the following sequential ALD steps. Low-temperature ALD is achieved by introducing Lewis-base catalysts, such as pyridine and ammonia.[7] Recently, a catalytic ALD of SiO_2 was reported using aminosilane.[126] To avoid involving halides, silicon oxide ALD was also accomplished using some alter-

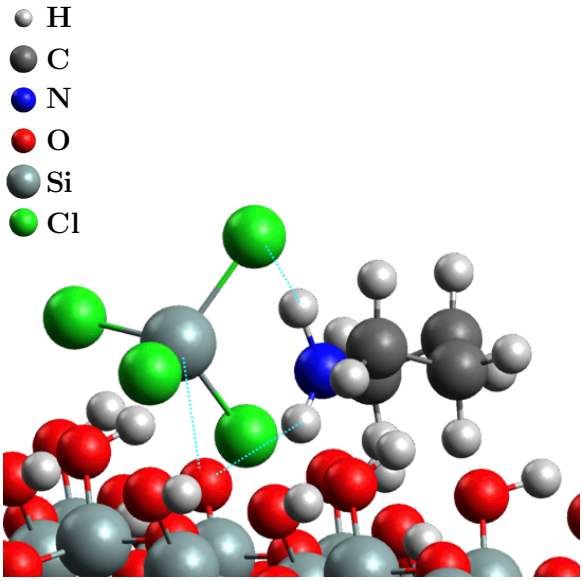

Figure 5.1: Trimolecular catalyzed deposition of SiO_2. The cyan dash lines show the interactions of a $SiCl_4$ precursor, a silicon oxide surface and a pyrrolidine catalyst.

native silicon precursors, such as TEOS, $Si(OEt)_4$[127] and water, along with ammonia as a catalyst. A room temperature ALD was achieved for this system but required large exposures of the precursors and catalysts.[129]

A challenge of the catalytic ALD process is that it involves a trimolecular first step, with low probability, and consequently low reaction rates. Therefore, an alternative approach is to design a silicon precursor with the catalyst as a ligand, so that when the precursor interacts with the surface, the catalyst is always present to enhance the chemical reaction. For example, the set ($(OEt)_3$-Si-($C_3H_6NH_2$), water and ozone) operates at 150 °C by thermal ALD,[132] and the ALD process produces no corrosive byproducts. A good candidate self-catalying silicon precursor should satisfy the conditions of reactivity towards surface deprotonation and stability of the bound configuration. The latter is important in determining the residence time of the precursor on the substrate, indirectly affecting deposition times and thus growth rate. Growth rates are also directly connected to the kinetics of the two sequential deposition steps, and thus to barrier heights and steric hindrance on the surface.

This study was a cooperative project with our industrial partner, Seastar Chemicals Inc. company from 2015 to 2017. The long term objective is to integrate the experimental and industrial results with the theoretical models and computational simulation so that a more complete understanding of ALD can be achieved and a more predictable model can be constructed. During the internship, some precursors were synthesized and examined based on our computational results, and many experimental data had feed-backed to the theoretical models. Some precursors eventually were examined in the ALD growing chamber in Japan. Due to the fast-paced, product-focused, goal-oriented aspects of industrial research, four short term objectives were prioritized and focused:

1. Establish and optimize theoretical models for the SiO_2 system. The models use a surface or a truncated cluster as the substrates with various proposed precursors.

2. Verify the model and the simulation methods by comparing the results against the experimental data provided by the company or literature search. Agreement of the two approaches can provide a better insight of the experimental results.

3. Rationalize the trends for precursor reactivities, reaction rates, preferred binding modes, and then use the understanding to further design and optimize new precursors.

4. Apply to Si_3N_4 systems to identify potential silicon precursor candidates for growing quality Si_3N_4 thin film via lower temperature ALD.

5.2 Methodology

DFT approximation and functionals: Zero-temperature DFT calculations were performed using the GGA with PBE[265] functional in the SIESTA 3.2 package[87,173] and Gaussian 09 version A.[196] A hybrid functional, Becke, three-parameter, Lee-Yang-Parr (B3LYP)[184,267] was also used in the Gaussian calculations because this functional has been widely used in the organic chemistry community for its decent accuracy on organic molecules.[71,126,130,160,162,191]

Basis sets: In SIESTA, the core electrons were described in terms of the pseudopotentials constructed in the scheme of Troullier and Martins,[194] and the valence electrons were described using PAOs with a TZP basis set. In Gaussian 09, 6-311+G(d,p) basis set was used. Since the basis set in Gaussian is also atom-based (similar to the PAOs), CP correction is implemented and corrected by the program as the default.

PAO cut-off radius and CP correction: For the PAOs in SIESTA, the orbitals are strictly localized and fall to zero outside a given cut-off radius by specifying a value of energy shift. Previous calculations by our group and others[60,93] suggested that 1 mRy is sufficiently fine to compute total energies with almost insignificant BSSE effect. The 1 mRy energy shift confinement is equivalent to 6 Å for the cut-off radius of the carbon PAO with the smallest ζ. Therefore, the CP correction was omitted in this set of calculations using SIESTA in this chapter.

van der Waals correction: No vdW correction was included in this study. Most of the self-catalying silicon precursors and reactants (water and ammonia) were small in size, and the gas phase calculations should have minimal vdW interaction. The contribution would be less significant comparing to the total binding energies and the reaction enthalpies. Technically, the vdW dispersive correction is not supported in any older versions of Gaussian 09 program, and the first version which includes the

Grimme-type pairwise potentials is version D; however, version A was available for this study.

Periodic boundary condition: All the surface calculations between the adsorbates and the silicon oxide surface were performed using SIESTA program with PBC. For modelling catalyst adsorption on the surface, a 2×2×2 silicon dioxide slab was used with 50 Å along the *z*-direction. For larger self-catalying silicon precursors, two larger slabs, 3×3×2 and a 4×4×2 were used to ensure that the precursors in the simulation box did not interact with their neighbouring images. All gas phase calculations were performed in the Gaussian 09 program.

Geometry optimization and AIMD approach: Optimizations were carried out using multiple input geometries. For more complex structures such as self-catalying silicon precursors, about ten input geometries were computed, and only the most stable configurations were reported herein. Some of the most stable configurations were also used as inputs for AIMD simulations. In this study, the mean of using AIMD was to investigate the conformational evolution of binding modes for the selected catalysts on a SiO_2 slab in some temperatures and thermostats. No statistical analysis was considered. As an attempt, the AIMD method was also used for two self-catalying silicon precursors, $(OMe)_2$-Si-$(Py)_2$ and $(OMe)_2$-Si-$(TMG)_2$ on the $SiO_2(110)$ surface, where Py and TMG stand for pyrrolidino and tetramethylguanidino. However, their thermal equilibria can not be reached within eight-month computing time (used 2 nodes with 32 cores each). We concluded that the AIMD approach was not yet suitable and practical for a more complicated silicon precursor on a SiO_2 surface.

Transition state (TS) calculation: Transition state calculation was performed using QST methods in the Gaussian 09 program. Two QST methods, QST2 and QST3, existed in the program, and they differed in if a guessed TS geometry was provided or not. The latter one required a guessed TS geometry. Multiple input

geometry strategy was also used for the calculation since the relative orientation of two reactants affected the simulation results, and only the lowest total energy results were reported herein. Configuration in a TS was proposed and considered only via 4-member ring reaction mechanism.[7,130,133] In this study, we interested in a reaction between a self-catalying silicon precursor and a water molecule; therefore, the guessed configuration in the TS was rearranged such that the Si–catalyst and the HO–H bonds were about to break and that the Si–OH and H–catalyst bonds were about to form.

5.3 Results and Discussion

5.3.1 Catalyst adsorption on the SiO_2 slab

We searched for catalysts able to deprotonate a surface -OH group. Nitrogen-containing catalysts are our primary target because of the lone pair on the nitrogen. Nine catalysts were selected: ammonia (NH_3), pyrrolidine, pyridine, pyrazine, 4-(*tert*-butyl)pyridine, 4-dimethylamino pyridine (4-DMAP), 4-aminopyridine (4-AP), 1,1,3,3-tetramethylguanidine (TMG) and triazabicyclodecene (TBD). Their structures are displayed in Fig. 5.2 except NH_3. These catalysts were chosen based on their pK_a values (see Table 5.1), and we aimed to examine a wide range of basicities. The binding configurations of the nine N-containing catalysts on a fully hydrogenated $2\times2\times2\times$ SiO_2 slab were optimized using DFT method, and the most stable configurations were shown in Fig. 5.4 with binding energies in Fig. 5.3.

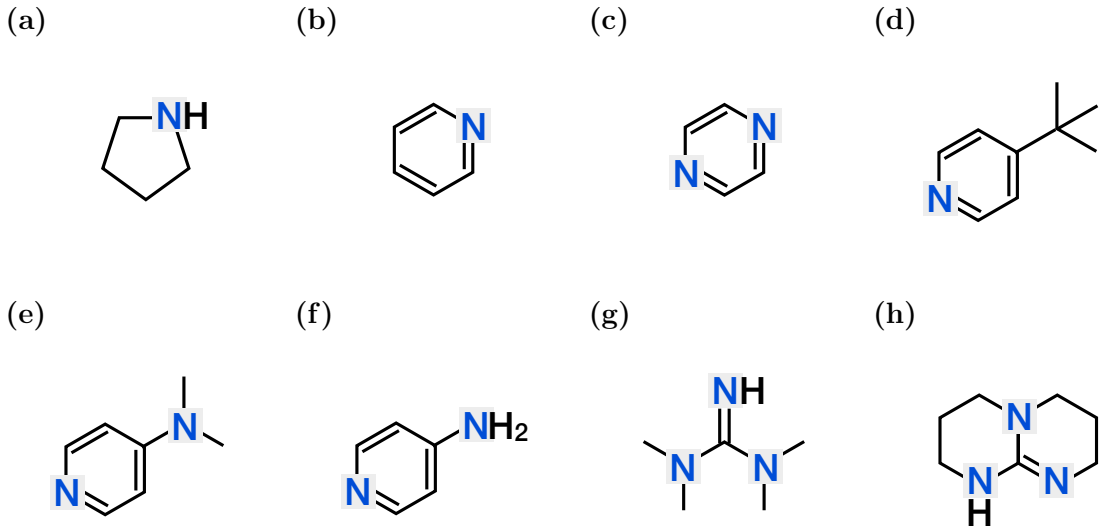

Figure 5.2: Structures of the selected catalysts: (a) pyrrolidine, (b) pyridine, (c) pyrazine, (d) 4-(*tert*-butyl)pyridine, (e) 4-dimethylaminopyridine (4-DMAP), (f) 4-aminopyridine (4-AP), (g) 1,1,3,3-tertramethylguanidine (TMG) and (h) triazabicyclodecene (TBD).

Table 5.1: pK_a values for some N-containing catalysts.

Catalysts	pK_a	ref.
TBD[1]	15.2	[268]
TMG [2]	13.0	[268]
pyrrolidine	11.27	[269]
4-DMAP[3]	9.6	[270]
ammonium	9.21	[269]
4-AP [4]	9.17	[271]
imidazole	7.05	[272]
4-tButylpyridine	5.99	[269]
pyridine	5.14	[269]
pyrazine	0.6	[273]

[1]TBD, (triazabicyclodecene)
[2]TMG, (tetramethylguanidine)
[3]DMAP, (dimethylamino pyridine)
[4]AP, (aminopyridine)

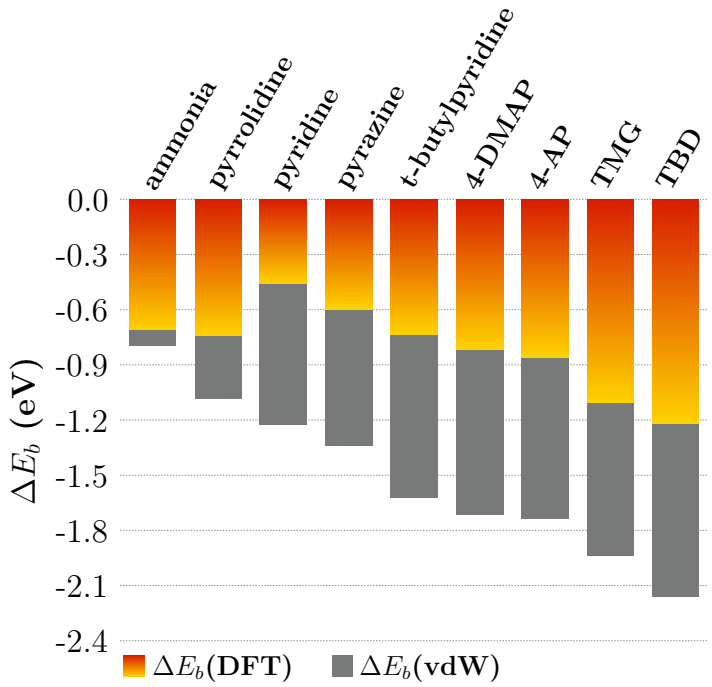

Figure 5.3: The binding energies of the nine selected N-containing catalysts on a SiO_2 slab, where the acronyms are defined in Table 5.1.

In general, the zero-temperature DFT calculations showed the lone-pair of N pointing directly toward the surface H, aligning the -OH bond without surface deprotonation. The exception was TBD (see Fig. 5.4). For the catalysts without aromatic rings such as ammonia, pyrrolidine, TMG and TBD, DFT contributions to binding energies were also higher than those with aromatic rings, as seen in Fig. 5.3. The most stable adsorbed configurations were examined at a higher temperature via AIMD. When an aromatic ring was absent, unimodal binding conformation, orientating tilted on the surface, was observed (see Fig. 5.5 and 5.6), and the major interaction was between the lone-pair of N and the surface -OH group. Pyrrolidine, especially, was the only catalyst showing upright orientation. On the other hand, bimodal binding conformations, orientating tilted and flattened to the surface, were observed in the presence of an aromatic ring, as shown in Fig. 5.7. One binding mode showed the same interaction as the unimodal binding mode (see Fig. 5.7 (a) and (c)), and another showed

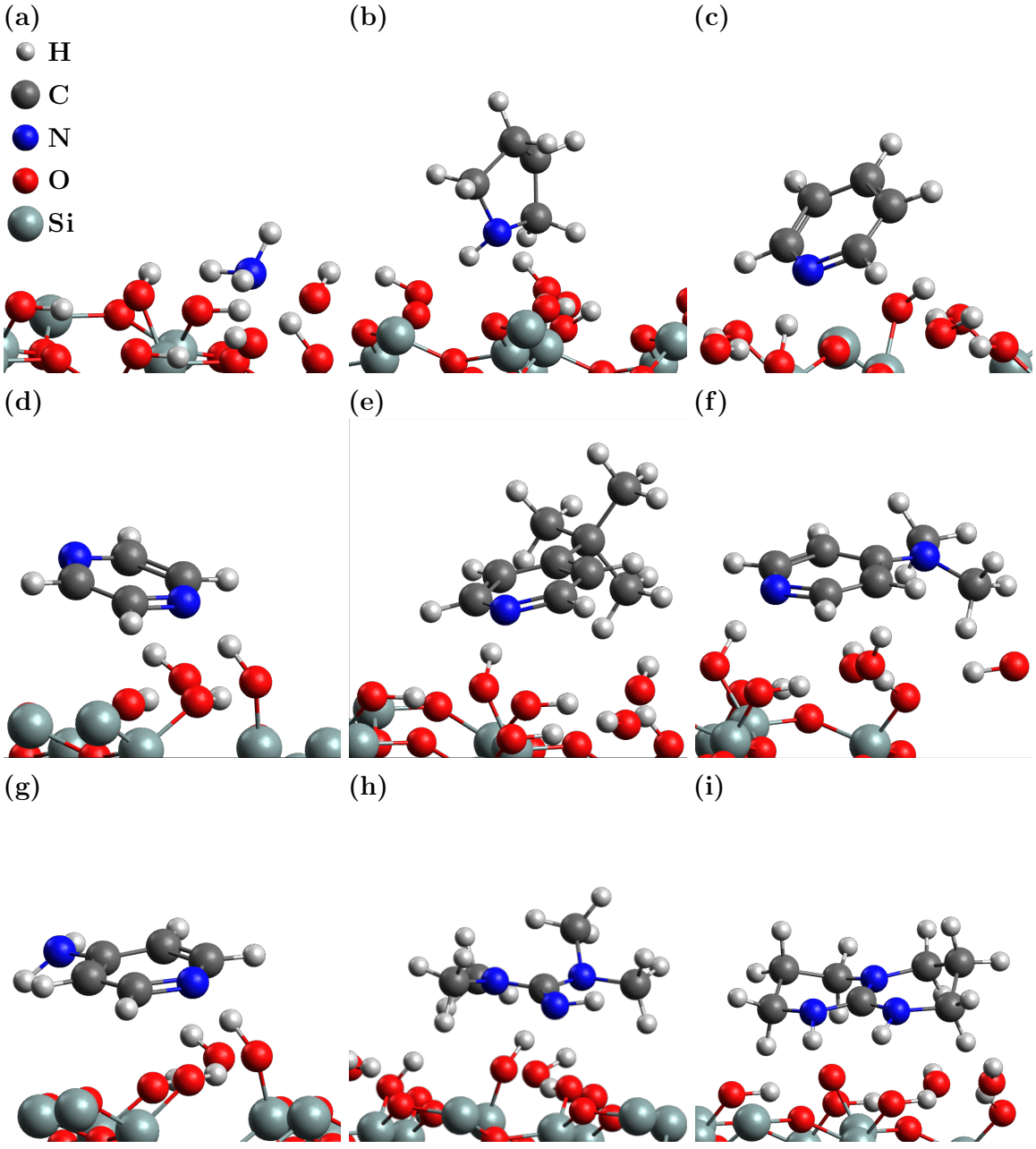

Figure 5.4: Configurations of the selected catalysts on a slab: (a) ammonia, (b) pyrrolidine, (c) pyridine, (d) pyrazine, (e) 4-(*tert*-butyl)pyridine, (f) 4-dimethylaminopyridine (4-DMAP), (g) 4-aminopyridine (4-AP), (h) 1,1,3,3-tertramethylguanidine (TMG) and (i) triazabicyclodecene (TBD).

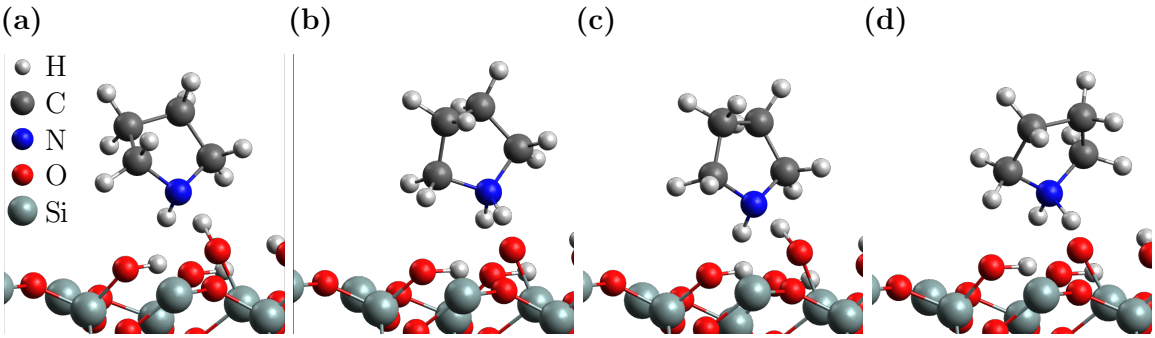

Figure 5.5: Conformational evolution of a pyrrolidine on a SiO_2 slab at 300 K.

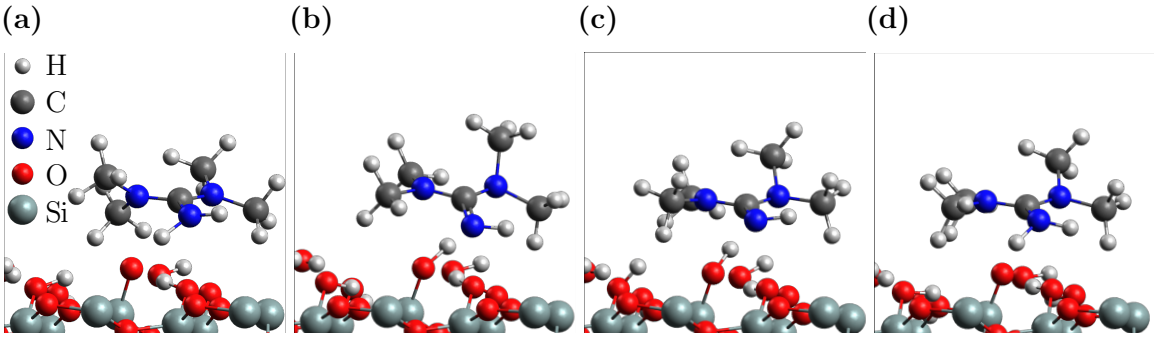

Figure 5.6: Conformational evolution of a TMG on a SiO_2 slab at 300 K.

the interaction between the delocalized π-orbital and the surface as the ring sat relatively flat on the surface, shown in (b). The bimodal binding mode also explained the tilted orientation for the most stable binding configurations shown in Fig. 5.4. Surface deprotonation was observed in almost all the catalysts except for the pyridine

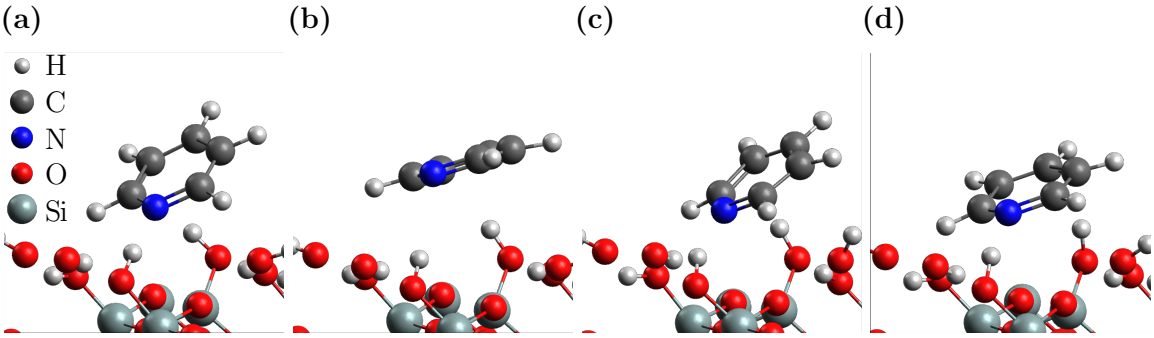

Figure 5.7: Conformational evolution of a pyridine on a SiO_2 slab at 300 K.

in the AIMD simulations, and a surface proton only transferred to a catalyst once the appropriate orientation was established: the lone-pair of N and the surface -OH in alignment. Another factor was the strength of deprotonation ability, and the pyridine was simply not a strong catalyst in this case.

5.3.2 Self-catalying silicon precursors on a SiO_2 slab

This subsection focuses on the three self-catalying precursors that were synthesized by our collaborators on a fully hydrogen-saturated $SiO_2(110)$ slab: H_n–Si–$(Py)_m$, $(OMe)_n$–Si–$(Py)_m$ and $(OMe)_n$–Si–$(TMG)_m$, where -Py and -TMG stand for pyrrolidino and tetramethylguanidino, and $n + m = 4$ (see Figs. 5.8, 5.9 and 5.11). In the solution phase experimental results provided by our collaborator, $(OMe)_2$–Si–$(Py)_2$ and $(OMe)_2$–Si–$(TMG)_2$ showed excellent reactivities, and the company was interested in: a) the stabilities of other ligand combinations (for example, $(OMe)_3$–Si–$(Py)_1$ and $(OMe)_1$–Si–$(Py)_3$) on the $SiO_2(110)$ surface, b) the binding modes of the precursors on the surface, c) the steric effect of the precursors and d) the binding configuration where a chemical reaction takes place. Here, no attempts were made on any TS calculation using the relaxed-scan method in SIESTA because of the complexities of the simulated systems and the lengthy simulation time required. Binding energy is presented as the total binding energy in this subsection.

H_n–Si–$(Py)_m$:

Two self-catalying precursors were targeted, H_2–Si–$(Py)_2$ and H–Si–$(Py)_3$. Their binding configurations and energies were shown in Fig. 5.8. The most stable configuration formed via two H-bonds (see panel (d)), and this binding motif was more stable by about 0.5 eV than single H-bond motif. Attempts were made to optimize a H–Si–$(Py)_3$ precursor via three H-bonds; however, such orientation was not stable due

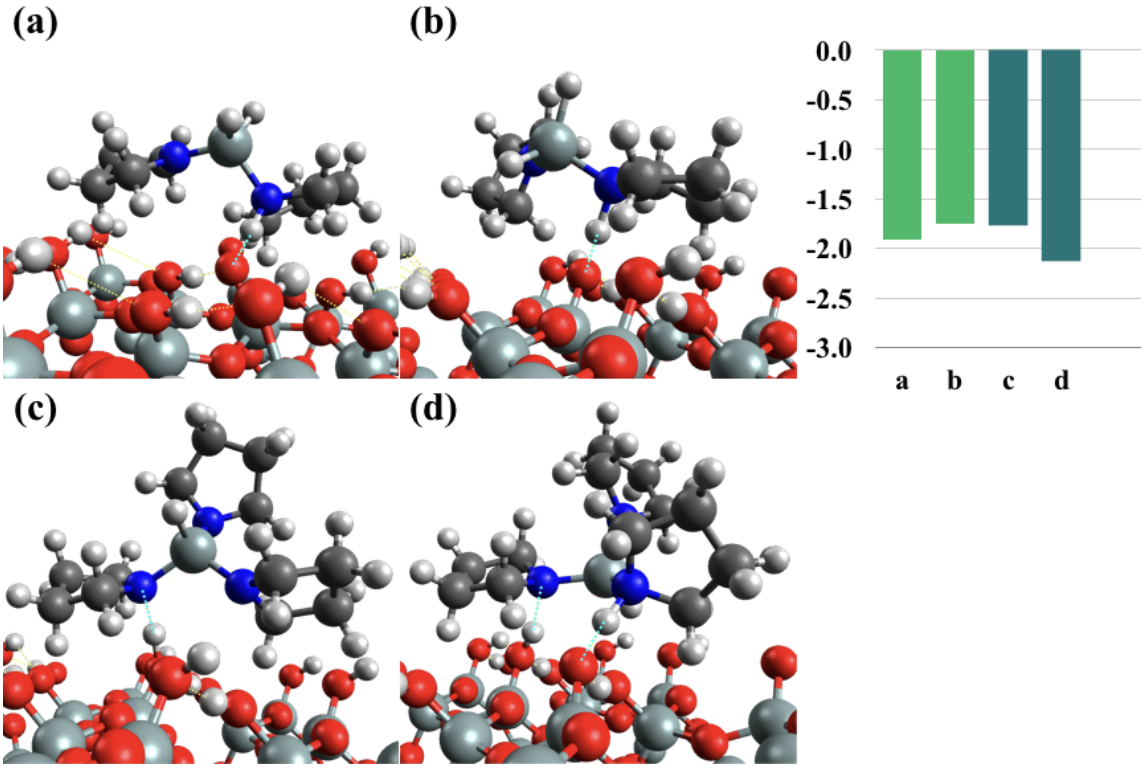

Figure 5.8: The binding configurations of H_2–Si–$(Py)_2$ in panels (a) and (b), and of H–Si–$(Py)_3$ in panels (c) and (d) with their corresponding binding energies in eV units. The precursor-surface interaction via H-bonding was marked in cyan dot lines.

to steric repulsion. Ideally, attaching more catalytic ligands to a precursor increases the chance for a surface reaction taking place, and the stability of the bound state of a precursor-surface complex; however, the steric effects of the bulkier substituent can prevent this type of binding.

$(OMe)_n$–Si–$(Py)_m$:

Three self-catalying precursors were studied in this series, $(OMe)_3$–Si–(Py), $(OMe)_2$–Si–$(Py)_2$ and (OMe)–Si–$(Py)_3$. The -H considered previously was replaced by a -OMe group, and the oxygen was able to interact with the surface -OH via H-bond. Similar to the H_n–Si–$(Py)_m$ result, the most stable configuration was formed via two H-bonds between the lone-pairs of N and the surface -OH groups, shown in Fig. 5.9

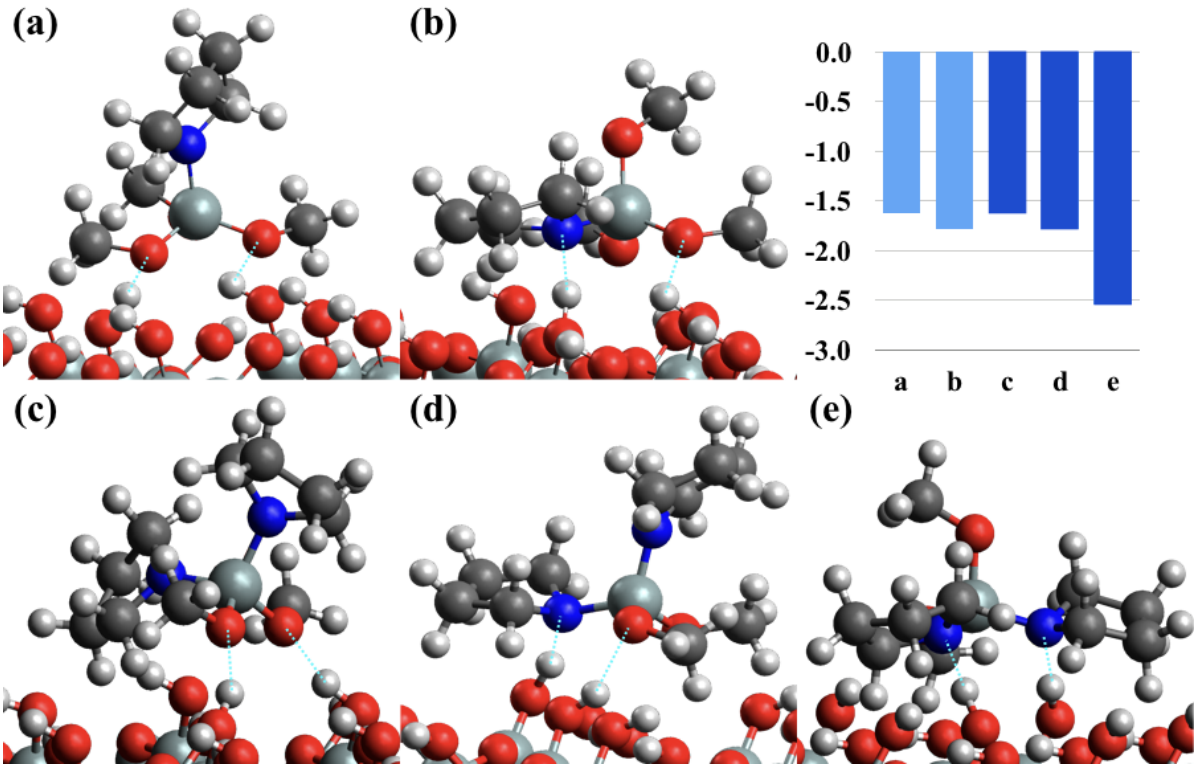

Figure 5.9: The binding configurations of (OMe)–Si–$(Py)_3$ in panels (a) and (b) and $(OMe)_2$–Si–$(Py)_2$ in panels (c), (d) and (e) with their corresponding binding energies in eV units. The precursor-surface interaction via H-bonding was marked in cyan dot lines.

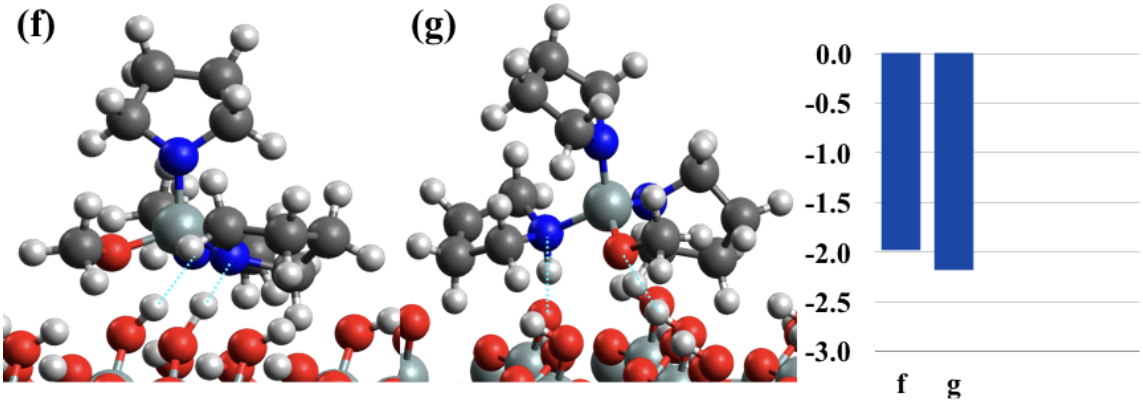

Figure 5.10: The binding configurations of $(OMe)_3$–Si–(Py) in panels (f) and (g) with their corresponding binding energies in eV units. The precursor-surface interaction via H-bonding was marked in cyan dot lines.

(e). Although such binding orientation was also achieved for the (OMe)–Si–$(Py)_3$ on the slab shown in Fig. 5.10 (f), its binding energy was 0.5 eV less than the most stable form, possibly due to the steric effect of an extra -Py group. The binding energies showed no significant differences for the interaction via two H-bonds involving a -OMe group, shown in panels (a) to (d). Additionally, these binding modes via two H-bonds had similar binding strengths as the bound states of H_n–Si–$(Py)_m$-surface via a single H-bond.

$(OMe)_n$–Si–$(TMG)_m$:

Two self-catalying precursors were studied, $(OMe)_3$–Si–$(TMG)_1$ and $(OMe)_2$–Si–$(TMG)_2$. Based on the experimental pK_a values (in Table 5.1) and our catalyst-slab binding energy results (in Fig. 5.3), TMG is a stronger Lewis base (more likely to take a proton) than pyrrolidine, and the company was interested to know if -TMG was a more reactive ligand than -Py. From the binding energy results shown in Fig. 5.11, the -TMG substituted precursors indeed formed more stable bound states than the -Py ones on the slab. The most stable configuration, shown in Fig. 5.11 panel (e) was formed in a similar way as $(OMe)_2$–Si–$(Py)_2$ on the slab, via two H-bonds between the lone-pairs of N and the surface -OH groups. The figure also presented the excellent deprotonation abilities of the precursors; nearly all -TMG ligands extracted a surface proton from a -OH group. Since the company was not interested in the three-equivalent precursor, (OMe)–Si–$(TMG)_3$, we can not conclude if such precursor outperformed the two-equivalent one.

In conclusion, our DFT-based simulation results showed that both 2-equivalent self-catalying precursors, $(OMe)_2$–Si–$(Py)_2$ and $(OMe)_2$–Si–$(TMG)_2$ performed outstandingly in terms of their binding stabilities in the bound states, preferred binding

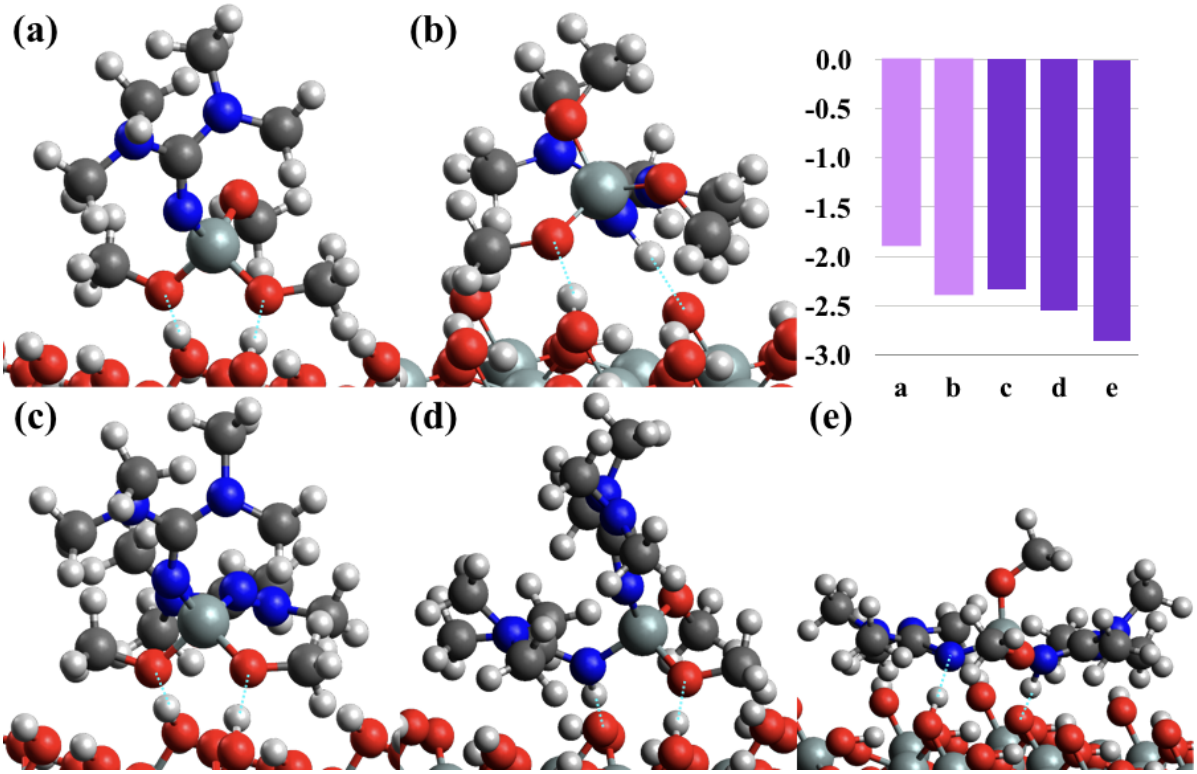

Figure 5.11: The binding configurations of $(OMe)_3$–Si–$(TMG)_1$ in panels (a) and (b) and $(OMe)_2$–Si–$(TMG)_2$ in panels (c), (d) and (e) with their corresponding binding energies in eV units. The precursor-surface interaction via H-bonding was marked in cyan dot lines.

orientations on the slab and minimal steric effect due to the -OMe group. From the most stable binding configurations, their two substituted catalysts (-Py and -TMG) orientated toward the $SiO_2(110)$ slab and interacted with the surface -OH groups. In the ALD process, the surface reaction was more likely to take place in such preferred bound state orientation and to form an adsorbed complex with two -OMe groups remaining in attachment and two byproducts (pyrrolidine and TMG catalysts). A more realistic non-fully hydrogen-saturated surface was suggested; however, this plan was postponed due to other research focuses and limited time.

5.3.3 Hydrolysis reaction for self-catalying precursors

Although our surface calculation results provided a substantial amount of information, including the steric effect of a self-catalying precursor, the preferred bound orientation on a slab and where a proton transfer taking place, such calculations are computationally intensive and not suitable for compound screening. Moreover, one crucial factor was intractable - activation energy. This result which directly related to reaction rate required even longer computational time because searching for a TS is not an easy task, especially involving a slab. We, therefore, focused on TS calculation and activation energy (ΔE_a) estimation in this subsection using QST methods in the Gaussian 09 program and a gas phase model.

The hydrolysis reaction was chosen here because the experiment can be performed on bench-top by our collaborators, and a gas phase simulation required less computing resources than a surface calculation. Here, two self-catalying silicon precursors were studied, $(\mathrm{OMe})_n$–Si–$(\mathrm{Py})_m$ and $(\mathrm{OMe})_n$–Si–$(\mathrm{TMG})_m$ where $m+n=4$. Total energy was computed by two functionals, PBE and B3LYP. As we compared the reaction enthalpies and the activation energies for the five precursors, the B3LYP results were generally 15% to 30% higher than the PBE's. Since the general trends were similar between the two functionals, only the PBE results are presented herein.

Notations and presentation:

The conventional way of presenting an energy diagram associating with reaction enthalpy and activation energy is shown in Fig. 5.12. In this representation, energies can be compared visually in a more obvious way, and their corresponding transition state configurations can also be seen. However, when presenting more than 9 precursors in such an energy diagram, the substantial amount of information can be quite challenging to read. Here, a more compact representation is used, and only reaction

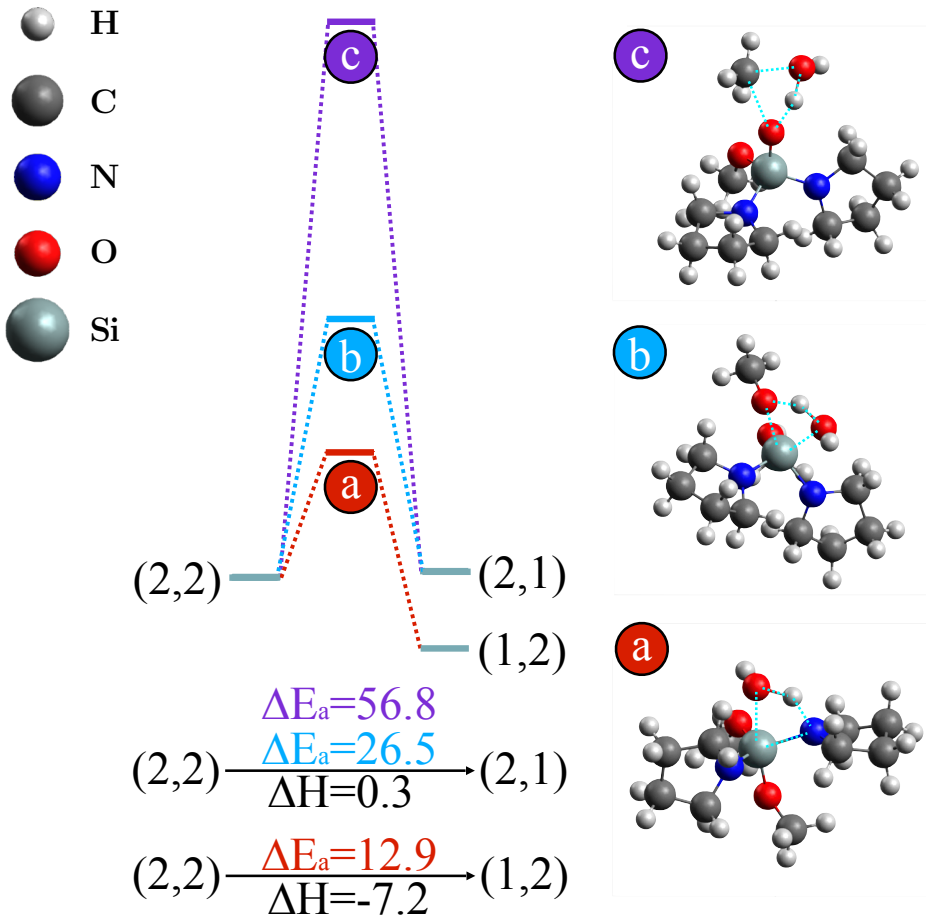

Figure 5.12: A energy diagram of presenting reaction enthalpy (ΔH) and activation energy (ΔE_a) for a hydrolysis reaction. The two indices in a round bracket mean the numbers of -catalyst and -OMe groups substituted to the Si. The energy values above and below the arrow are activation energy and reaction enthalpy respectively.

enthalpies and activation energies are specified. For a self-catalying silicon precursor, the numbers of substituted -catalyst and -OMe groups are indicated in round bracket notation, (m,n). For example, $(OMe)_1$–Si–$(Py)_3$ is denoted as (3,1).

$(OMe)_n$–Si–$(Py)_m$:

In the hydrolysis reaction, for the reaction of a water molecule with the Si centre of a self-catalying precursor, two possible pathways were considered: exchanging the catalyst (-Py group here) or the -OMe group with a -OH group. The reaction terminated when all the substituents were replaced by the -OH, and Si-$(OH)_4$ was formed. Three self-catalying precursors, -$(Py)_3$, -$(Py)_2$ and -(Py) were studied under sequential replacements until the final product was formed, as shown in Fig. 5.13. The map presents all the possible reaction pathways for the $(OMe)_n$–Si–$(Py)_m$ series. Reaction rates were primarily sought because the deposition time for lower temperature ALD was short, and thus a self-catalying precursor must react rapidly with the SiO_2 surface. Although we, here, examined the bond strengths of Si–Py and Si–OMe by using hydrolysis reaction, we expected to observe lower activation energy, ΔE_a for breaking a Si–Py bond. Fig. 5.13 shows that replacing a -Py group with a -OH group (arrows going from left to right) was generally preferred due to lower activation energies (ranging from 10.7 to 17.3 kcal/mol). On the contrary, replacing a -OMe group (arrows going from top to bottom in the same Figure) required higher ΔE_a values (ranging from 14.4 to 26.9 kcal/mol). The simulation results supported the experimental observation providing by our collaborators. In terms of reaction enthalpy ΔH, replacing a -Py group with a -OH led to an exothermic reaction while no significant enthalpy differences were obtained for replacing a -OMe group with an -OH.

The overall performance of the (2,2)-precursor, $(OMe)_2$–Si–$(Py)_2$ was outstanding. Initiating a -Py replacement (from (2,2) to (1,2)) required less ΔE_a than starting with the (3,1)-precursor by 4.4 kcal/mol. Additionally, the sequential reaction (from (1,2) to (0,2)) did not require a higher ΔE_a value. Probability-wise, the (2,2)-precursor contained one extra -Py group than the (1,3)-precursor which gave the (2,2)-precursor

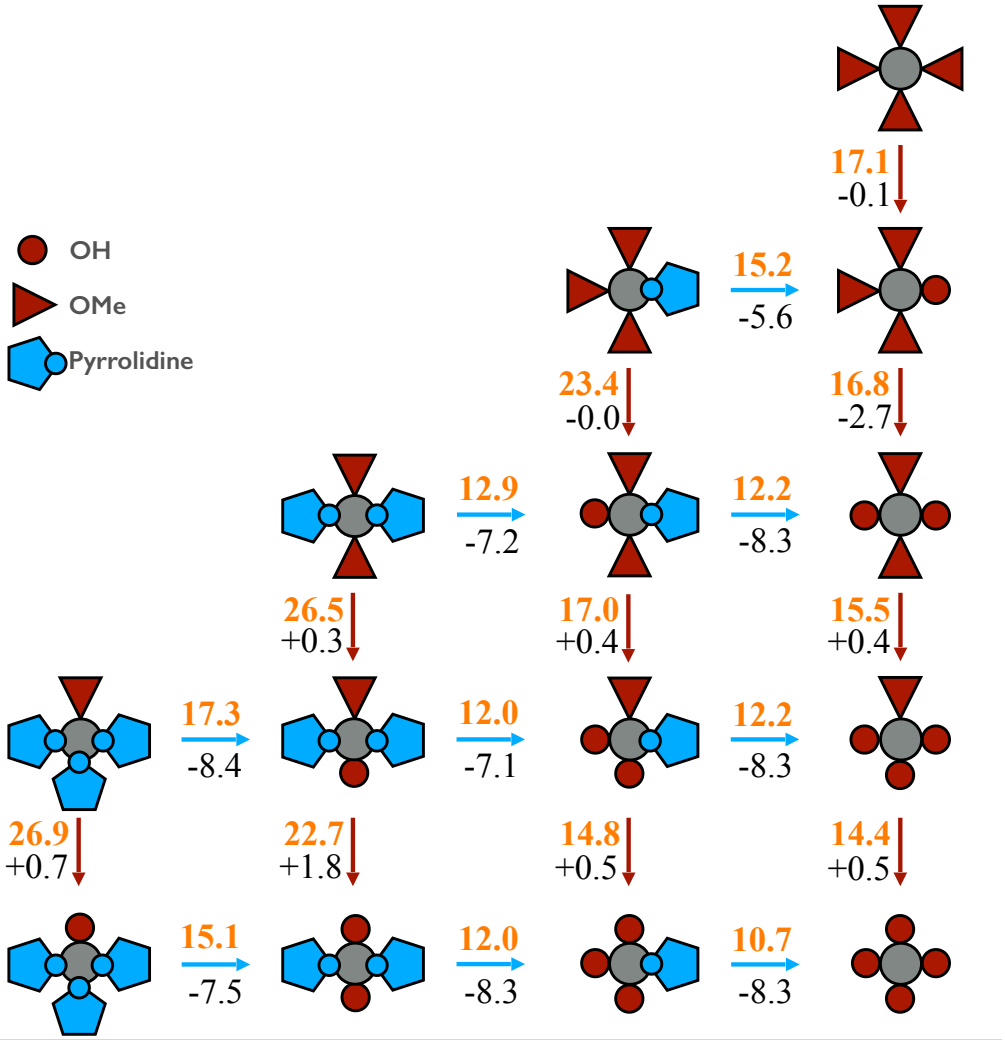

Figure 5.13: Hydrolysis reaction pathways of the self-catalying precursor, $(OMe)_n$–Si–$(Py)_m$ where $m+n=4$. The blue and red arrows indicate the replacement of -Py and -OMe groups with a -OH group, and the purple arrow indicates the exchange between the two substituted groups. The energy values are in kcal/mol units. The energy values in orange and in black are the activation energies and reaction enthalpies respectively.

higher chance to chemically react with another reactant, a water molecule in this case, and therefore faster reaction rate.

$(OMe)_n$–Si–$(TMG)_m$:

Two self-catalying precursors, -$(TMG)_2$ and -(TMG) were studied under sequential replacements, and Fig. 5.14 showed all the possible reaction pathways for the $(OMe)_n$–Si–$(TMG)_m$ series. The -TMG substituted precursors followed similar trends

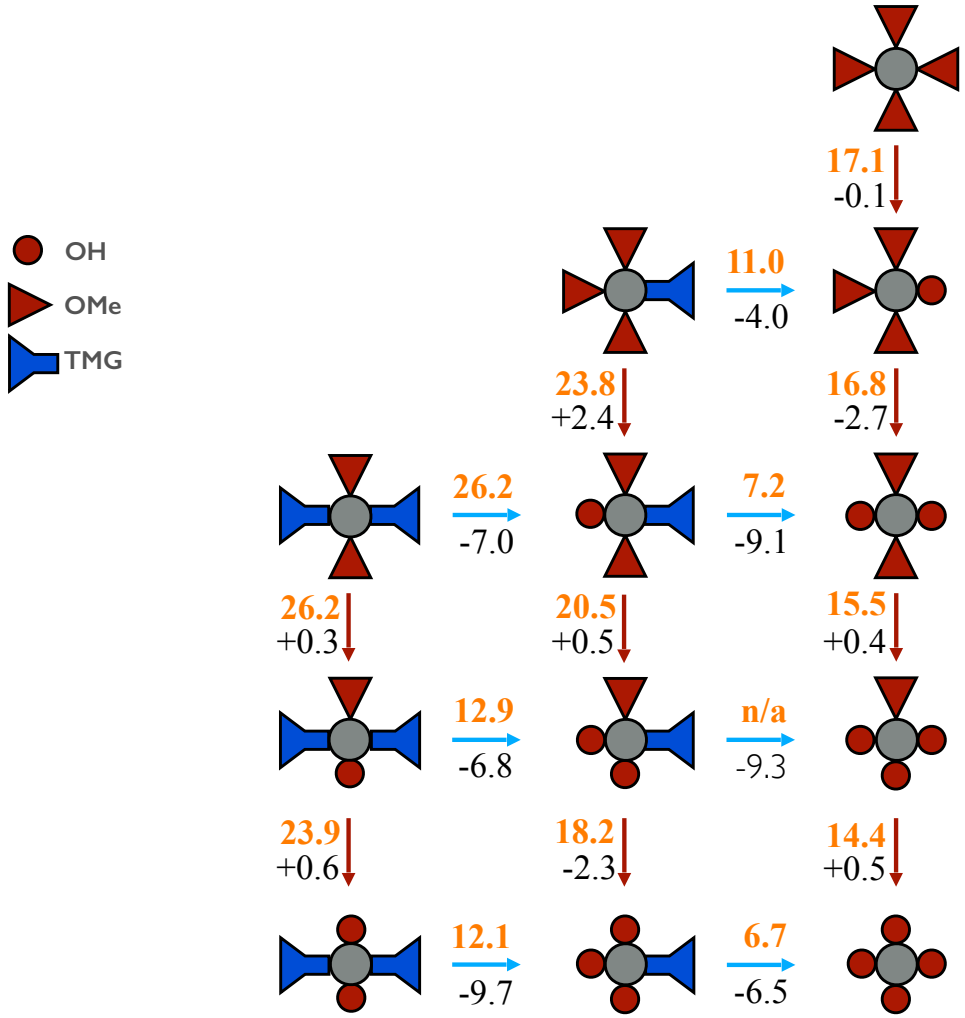

Figure 5.14: Hydrolysis reaction pathways of the self-catalying precursor, $(OMe)_n$–Si–$(TMG)_m$ where $m+n=4$. If not otherwise specified, headings are the same as in Fig. 5.13

as the -Py ones, including the enthalpy changes. Replacing a -TMG substituent required less ΔE_a than replacing a -OMe group; the Si–TMG bond strength was generally weaker than the Si–OMe bond in the hydrolysis reaction. Somewhat surprisingly,

the first -TMG replacement was exceedingly hard (ΔE_a value is 26.2 kcal/mol), despite repeated calculations with different initial geometries. Thus, the (2,2)-TMG precursor was a less favourable precursor. On the contrary, replacing the last -TMG substituent from (1,n) to (0,n) with a -OH group required less ΔE_a than replacing a -Py substituent.

5.4 Conclusion

This study was a collaborative project with our industrial partner, Seastar Chemicals Inc. company funded by MITACS from 2015 to 2017. The project focused on understanding the chemical and physical effects of some catalytic substituents on a Si centre, including the binding strengths, the binding modes, the steric effects, and the reactivities on a SiO_2 surface in the ALD process. An extension of the project was to build a predictable model that is able to guide precursor design. All the surface calculations were performed using DFT-D2/PBE method with the TZP basis set and 1 mRy energy shift setting by the SIESTA 3.2 package, and using DFT/PBE/QST method with 6-311+G(d,p) basis set by the Gaussian 09 version A for the transition state calculations. Two experimentally synthesized self-catalying silicon precursors, $(OMe)_2$–Si–$(Py)_2$ and $(OMe)_2$–Si–$(TMG)_2$ were under detailed investigation. We found that the preferred binding mode for the two precursors on the $SiO_2(110)$ slab had the two catalyst substituents oriented toward the slab, and interacting with the surface -OH groups via two H-bonds. We also concluded that breaking the Si–N bond generally required less energy than the Si-O bond from the activation energy data, and thus was consistent for all precursors considered here. The precursors examined in detail exhibited outstanding performance in chemical reactivities, with minimal steric effect on the surface.

Chapter 6

General Conclusions and Future Work

6.1 General conclusions

Our group has been investigating the binding behaviours and the interplay of molecule-surface and intermolecular interactions of sulfur-containing amino acids (cysteine, homocysteine and methionine) on gold surfaces using Monte Carlo, classical force field, *ab initio* DFT and DFT-TS methods. Previous work had shown that the binding strengths of the three nonionic amino acids on the Au(111) surface were generally weak due to the absence of the dispersive vdW potential. The DFT method is known to describe dispersive vdW interaction inadequately. Although dispersion corrections to DFT were published as early as 2005, the implementation in SIESTA simulation program happened only recently (2016). Therefore, one of the objectives in this dissertation was to revisit the binding behaviour of the three amino acids on the Au(111) surface using DFT-TS method (discussed in Chapter 4). This particular method was chosen because of two main reasons: **a)** the TS formalism uses a classical pairwise po-

tential approach, thus the computational cost was insignificant, and **b)** the dispersive energy was estimated separately from the DFT algorithm, thus the dispersive binding energy can be estimated. The total binding energy can then be partitioned into the *pure* DFT and dispersive correction contributions. The beauty of this approach was that it bridged the results of the fundamental DFT to the more advanced vdW-DF which can be one of the future studies.

Another objective was to examine whether the computational cost of surface-adsorbate interactions can be reduced by reducing the size of the simulation system from a more realistic surface to a cluster (discussed in Chapter 3). Although the computational cost of the DFT method is relatively low compared to post-Hartree-Fock methods, the resources used can increase significantly when the size of the simulating system was relatively large, especially considering some adsorbates on a more realistic surface.

Previous studies in the group suggested that the binding behaviour of an adsorbate-substrate complex may depend on the saturation (the coordination number) of the surface binding site. A 20-atom gold cluster was designed to provide a series of distinct available binding sites, with coordination numbers between 3 and 9. The study in Chapter 3 reduced the more realistic binding complexes (cysteine, homocysteine and methionine) on a gold surface down to the functional group on a small gold cluster. In this case, only the adsorbed groups, methylthiol, methylthiolate, dimethyl sulfide and methylamine involved to the binding at a gold binding site. Due to the size of the system, the computational cost significantly reduced, so the configurational space was systematically sampled (exhaustive search method). This exhaustive search strategy required a substantial amount of distinct calculations, and thus might not be appropriate for more realistic adsorbates and gold surfaces with various coordination numbers and much larger system sizes (Chapter 4 as example).

The binding strengths calculated on Au_{20} did not increase monotonously with the unsaturation of a binding site (smaller CN value). For all four methyl-capped adsorbates, the energetically preferred binding site was at the kink binding site with an intermediate CN value, CN6. The kink site had the strongest binding reactivity by maximizing the dispersive interactions between the gold atoms and the methyl group. Surprisingly, methylamine showed similar binding strengths as methylthiol due to a more localized lone-pair-cluster interaction. Despite known issues with the empirical nature of dispersive corrections, the inclusion in DFT calculation was necessary, particularly for the more weakly-bound adsorbates since the dispersive interactions played a significant role in overall binding behaviour.

The investigations of the three *L*- form sulfur-containing amino acids (cysteine, homocysteine and methionine) on gold surfaces had two aims: **a)** to revisit the previous results that used *pure* DFT method by using DFT-TS method, and **b)** to extend the coordination number study from the Au_{20} cluster model to a more realistic surface model with a surface adatom. For the monomers on the Au(111), only the unconventional zwitterionic forms (for cysteine and homocysteine) and the nonionic cooperative binding modes (homocysteine and methionine) presented relatively stable binding configurations. The vdW dispersion dominated the binding interaction between the nonionic monomers and the surface via a single-coordinate bond, either the mercapto or the amino group. With the presence of a surface adatom, the covalent-type (approximated by *pure* DFT) binding strengths were enhanced significantly by 0.4 eV to 0.7 eV, depending on the amino acids, even for the nonionic monomers on the adatom surface. The dimer forms were also investigated to determine the binding strengths of various distinct intermolecular interactions on the Au(111) surface. The unconventional (forming intramolecularly) and conventional (forming intermolecularly) dimer motifs resulted in the most stable dimer binding

configurations while the most stable nonionic form involved a cooperative binding modes with COOH – COOH intermolecular interaction between the dimer.

For the internship with Seastar Chemicals Inc. company, the study first focused on establishing a simulation model to describe the binding behaviours of various nitrogen-containing catalysts and two self-catalyzing silicon precursors on a SiO_2 surface in the ALD process. The preferred binding modes of the two self-catalyzing silicon precursors, $(OMe)_2$–Si–$(Py)_2$ and $(OMe)_2$–Si–$(TMG)_2$ on the SiO_2 surface were bound to have the two catalytic ligands orientated toward the surface, forming two H-bonds between the lone-pair of N and the surface -OH groups. Hydrolysis reactions were considered to study the chemical reactivities of the two self-catalyzing silicon precursors, and activation energies were computed for various distinct reaction pathways. With the relative low activation energies and high reaction enthalpies, the two self-catalying silicon precursors showed outstanding performance, and were considered to be the most promising catalytic candidates for the silicon-cycle in the ALD process.

6.2 Future work

The stable dimer forms of the three amino acids (cysteine, homocysteine and methionine) on the adatom surface require further investigation. Although the optimized configurations of the dimers on Au(111) and the monomers on adatom surface were used, with some modifications, as the inputs, searching for stable optimized dimer configurations on the adatom surface still requires extensive computational resources for computing sufficient distinct input geometries. Input files increased manyfold because the potential energy surface of the adatom surface was extremely complex, and degrees of freedom of the adsorbed dimers were high.

The stronger binding strength due to the highly unsaturated surface adatom should be examined from the electronic structures, integrated projected density of states (IPDOS), integrated crystal orbital Hamilton population (ICOHP) analysis and molecular orbitals (MOs) since the reactivity related to its energy states and densities. We had previously considered the electronic structures for the adsorbate-Au_{20} binding complexes; however, because each binding site was unique with distinct of neighbouring geometries, general trends were obscured. The work remained unpublished. Counterintuitively, the electronic structures of the adatom surface model might be simpler than the Au_{20} cluster model because the adatom had almost identical surrounding everywhere on the Au(111) surface.

Bibliography

[1] Liu, W.; Ruiz, V. G.; Zhang, G.-X.; Santra, B.; Ren, X.; Scheffler, M.; Tkatchenko, A. *New J. Phys.* **2013**, *15*, 053046–1–27.

[2] Hoja, J.; Reilly, A. M.; Tkatchenko, A. *WIREs Comput. Mol. Sci.* **2016**, *7*, 1–26.

[3] Vericat, C.; Vela, M. E.; Benitez, G.; Carro, P.; Salvarezza, R. C. *Chem. Soc. Rev.* **2010**, *39*, 1805–1834.

[4] Adamkiewicz, M.; O'Hagan, D.; Hähner, G. *Beilstein J. Org. Chem.* **2014**, *10*, 2897–2902.

[5] Nicosia, C.; Huskens, J. *Mater. Horiz.* **2014**, *1*, 32–45.

[6] Costa, D.; Pradier, C.-M.; Tielens, F.; Savio, L. *Surf. Sci. Rep.* **2015**, *70*, 449–553.

[7] George, S. M. *Chem. Rev.* **2010**, *110*, 111–131.

[8] Nuzzo, R. G.; Allara, D. L. *J. Am. Chem. Soc.* **1983**, *105*, 4481–4483.

[9] Love, J. C.; Estroff, L. A.; Kriebel, J. K.; Nuzzo, R. G.; Whitesides, G. M. *Chem. Rev.* **2005**, *105*, 1103–1169.

[10] Häkkinen, H. *Nat. Chem.* **2012**, *4*, 443–455.

[11] Bürgi, T. *Nanoscale* **2015**, *7*, 15553–15567.

[12] Sagiv, J. *J. Am. Chem. Soc.* **1980**, *102*, 92–98.

[13] Netzer, L.; Sagiv, J. *J. Am. Chem. Soc.* **1983**, *105*, 674–676.

[14] Onclin, S.; Ravoo, B. J.; Reinhoudt, D. N. *J. Am. Chem. Soc.* **2005**, *44*, 6282–6304.

[15] Haensch, C.; Hoeppener, S.; Schubert, U. S. *Chem. Soc. Rev.* **2010**, *39*, 2323–2334.

[16] Benitez, D.; Shapiro, N. D.; Tkatchouk, E.; Wang, Y.; Goddard, W. A.; Toste, F. D. *Nat. Chem.* **2009**, *1*, 482–486.

[17] Zhukhovitskiy, A. V.; Mavros, M. G.; Voorhis, T. V.; Johnson, J. A. *J. Am. Chem. Soc.* **2013**, *135*, 7418–7421.

[18] Crudden, C. M.; Horton, J. H.; Ebralidze, I. I.; Zenkina, O. V.; McLean, A. B.; Drevniok, B.; She, Z.; Kraatz, H.-B.; Mosey, N. J.; Seki, T.; Keske, E. C.; Leake, J. D.; Rousina-Webb, A.; Wu, G. *Nat. Chem.* **2014**, *6*, 409–553.

[19] Engel, S.; Fritz, E.-C.; Ravoo, B. J. *Chem. Soc. Rev.* **2017**, *46*, 2057–2075.

[20] Larrea, C. R.; Baddeley, C. J.; Narouz, M. R.; Mosey, N. J.; Horton, J. H.; Crudden, C. M. *ChemPhysChem* **2017**, *18*, 1–5.

[21] Guo, Q.; Li, F. *Phys. Chem. Chem. Phys.* **2014**, *16*, 19074–19090.

[22] Maier, N. M.; Franco, P.; Lindner, W. *J. Chromatogr. A* **2001**, *906*, 3–33.

[23] Barlow, S.; Raval, R. *Surf. Sci. Rep.* **2003**, *50*, 201–341.

[24] Mallat, T.; Orglmeister, E.; Baiker, A. *Chem. Rev.* **2007**, *107*, 4863–4890.

[25] Kühnle, A. *Curr. Opin. Colloid Interface Sci.* **2009**, *14*, 157–168.

[26] Stobiecka, M.; Deeb, J.; Hepel, M. *Biophys. Chem.* **2010**, *146*, 98–107.

[27] Wenzel, B.; Fischer, S.; Brust, P.; Steinbach, J. *J. Chromatogr. A* **2010**, *1217*, 3855–3861.

[28] Bantz, K. C.; Meyer, A. F.; Wittenberg, N. J.; Im, H.; Kurtulus, Ö.; Lee, S. H.; Lindquist, N. C.; Oh, S.-H.; Haynes, C. L. *Phys. Chem. Chem. Phys.* **2011**, *13*, 11551–11567.

[29] Hussain, A.; Sarangi, S.; Kesarwani, J.; Sahu, S. *Biosens. Bioelectron.* **2011**, *29*, 60–65.

[30] Weng, Z.; Wang, H.; Vongsvivut, J.; Li, R.; Glushenkov, A. M.; He, J.; Chen, Y.; Barrow, C. J.; Yang, W. *Anal. Chim. Acta* **2013**, *803*, 128–134.

[31] Miao, L.-J.; Xin, J.-W.; Shen, Z.-Y.; Zhang, Y.-J.; Wang, H.-Y.; Wu, A.-G. *Sens. Actuators, B* **2013**, *176*, 906–912.

[32] Conzone, S. D.; Pantano, C. G. *Mater. Today* **2004**, 20–26.

[33] Jain, P. K.; Lee, K. S.; El-Sayed, I. H.; El-Sayed, M. A. *J. Phys. Chem. B* **2006**, *110*, 7238–7248.

[34] Kogot, J. M.; England, H. J.; Strouse, G. F.; Logan, T. M. *J. Am. Chem. Soc.* **2008**, *130*, 16156–16157.

[35] Heinz, H.; Lin, T.-J.; Mishra, R. K.; Emami, F. S. *Langmuir* **2012**, *29*, 1754–1765.

[36] Wang, A.; Vangala, K.; Vo, T.; Zhang, D.; Fitzkee, N. C. *J. Phys. Chem. C* **2014**, *118*, 8134–8142.

[37] Larson, T. A.; Joshi, P. P.; Sokolov, K. *ACS Nano* **2012**, *6*, 9182–9190.

[38] Dreaden, E. C.; Alkilany, A. M.; Huang, X.; Murphy, C. J.; El-Sayed, M. A. *Chem. Soc. Rev.* **2012**, *41*, 2740–2779.

[39] Costa, D.; Savio, L.; Pradier, C.-M. *J. Phys. Chem. B* **2016**, *120*, 7039–7052.

[40] Islam, A.; Rabbani, M.; Bappy, M. H.; Miah, M. A. R.; Sakib, N. *IEEE* **2013**, 1–5.

[41] Pathak, S.; Sakai, N.; Rivarola, F. W. R.; Stranks, S. D.; andGiles E. Eperon, J. L.; Ducati, C.; Wojciechowski, K.; Griffiths, J. T.; Haghighirad, A. A.; Pellaroque, A.; Friend, R. H.; Snaith, H. J. *Chem. Mater.* **2015**, *27*, 8066–8075.

[42] Guo, F.; Karl, A.; Xue, Q.-F.; Tam, K. C.; Forberich, K.; Brabec, C. J. *Light: Sci. App.* **2017**, *6*, 1–8.

[43] Grönbeck, H.; Curioni, A.; Andreoni, W. *J. Am. Chem. Soc.* **2000**, *122*, 3839–3842.

[44] Andreoni, W.; Curioni, A.; Groenbeck, H. *Int. J. Quantum Chem.* **2000**, *80*, 598–608.

[45] Kühnle, A.; Linderoth, T. R.; Hammer, B.; Besenbacher, F. *Nature* **2002**, *415*, 891–893.

[46] Kühnle, A.; Linderoth, T. R.; Besenbacher, F. *J. Am. Chem. Soc.* **2003**, *125*, 14680–14681.

[47] Felice, R. D.; Selloni, A.; Molinari, E. *J. Phys. Chem. B* **2003**, *107*, 1151–1156.

[48] Kühnle, A.; Linderoth, T. R.; Schunack, M.; Besenbacher, F. *Langmuir* **2006**, *22*, 2156–2160.

[49] Kühnle, A.; Linderoth, T. R.; Besenbacher, F. *J. Am. Chem. Soc.* **2006**, *128*, 1076–1077.

[50] Kühnle, A.; Linderoth, T. R. *Top. Catal* **2011**, *54*, 1384–1391.

[51] Buimaga-Iarinca, L.; Calborean, A. *Phys. Scr.* **2012**, *86*, 1–6.

[52] Askerka, M.; Pichugina, D.; Kuz'menko, N.; Shestakov, A. *J. Phys. Chem. A* **2012**, *116*, 7686–7693.

[53] Zhao, Y.; Zhou, F.; Zhou, H.; Su, H. *Phys. Chem. Chem. Phys.* **2013**, *15*, 1690–1698.

[54] Fajín, J. L. C.; Gomes, J. R. B.; Cordeiro, M. N. D. S. *Langmuir* **2013**, *29*, 8856–8864.

[55] Popa, T.; Ting, E. C.; Paci, I. *Surf. Sci.* **2014**, *629*, 20–27.

[56] Verde, A. V.; Acres, J. M.; Maranas, J. K. *Biomacromolecules* **2009**, *10*, 2118–2128.

[57] Wright, L. B.; Rodger, P. M.; Corni, S.; Walsh, T. R. *J. Chem. Theory Comput.* **2013**, *9*, 1616–1630.

[58] Corni, S.; Hnilova, M.; Tamerler, C.; Sarikaya, M. *J. Phys. Chem. C* **2013**, *117*, 16990–17003.

[59] Mateo-Martí, E.; Rogero, C.; Gonzalez, C.; Sobrado, J. M.; de Andrés, P. L.; Martin-Gago, J. *Langmuir* **2009**, *26*, 4113–4118.

[60] Chapman, C. R. L.; Ting, E. C.; Kereszti, A.; Paci, I. *J. Phys. Chem. C* **2013**, *117*, 19426–19435.

[61] Crowell, J. E. *J. Vac. Sci. Technol., A* **2003**, *21*, 88–95.

[62] Ritala, M.; Leskelä, M.; Dekker, J.-P.; Mutsaers, C.; Soininen, P. J.; Skarp, J. *Chem. Vap. Deposition* **1999**, *5*, 7–9.

[63] Ritala, M.; Kukli, K.; Rahtu, A.; Räisänen, P. I.; Leskelä, M.; Sajavaara, T.; Keinonen, J. *Science* **2000**, *288*, 319–321.

[64] Leskelä, M.; Ritala, M. *Thin Solid Films* **2002**, *409*, 138–149.

[65] Puurunen, R. L. *J. Appl. Phys.* **2005**, *97*, 121301–1–52.

[66] Suntola, T.; Antson, J. Method for producing compound thin films. Patent US 4058430, 1977.

[67] Nishizawa, J.; Abe, H.; Kurabayashi, T. *J. Electrochem. Soc.* **1985**, *132*, 1197–1200.

[68] Bedair, S. M.; Tischler, M. A.; Katsuyama, T.; El-Masry, N. A. *Appl. Phys. Lett.* **1985**, *47*, 51– 53.

[69] Goodman, C. H. L.; Pessa, M. V. *J. Appl. Phys.* **1986**, *60*, 65–81.

[70] George, S. M.; Ott, A. W.; Klaus, J. W. *J. Phys. Chem.* **1996**, *100*, 13121–13131.

[71] Perrine, K. A.; Teplyakov, A. V. *Chem. Soc. Rev.* **2010**, *39*, 3256–3274.

[72] Hoeffling, B.; Ortmann, F.; Hannewald, K.; Bechstedt, F. *Phys. Rev. B* **2010**, *81*, 1–12.

[73] Tuttle, T. *Isr. J. Chem.* **2015**, *55*, 724–734.

[74] Sholl, D. S.; Asthagiri, A.; Power, T. D. *J. Phys. Chem. B* **2001**, *105*, 4771–4782.

[75] Horvath, J. D.; Gellman, A. *J. Am. Chem. Soc.* **2002**, *124*, 2384–2392.

[76] Horvath, J. D.; Koritnik, A.; Kamakoti, P.; Sholl, D. S.; Gellman, A. J. *J. Am. Chem. Soc.* **2004**, *126*, 14988–14994.

[77] Rampulla, D. M.; Francis, A. J.; Knight, K. S.; Gellman, A. J. *J. Phys. Chem. B* **2006**, *132*, 10411–10420.

[78] Yun, Y.; Gellman, A. J. *Angew. Chem. Int. Ed.* **2013**, *52*, 3394–3397.

[79] Gellman, A. J.; Huang, Y.; Feng, X.; Pushkarev, V. V.; Holsclaw, B.; Mhatre, B. S. *J. Am. Chem. Soc.* **2013**, *135*, 19208–19214.

[80] Yun, Y.; Gellman, A. J. *Nat. Chem.* **2015**, *7*, 520–525.

[81] Needs, R.; Godfrey, M.; Mansfield, M. *Surf. Sci.* **1991**, *242*, 215–221.

[82] Chen, W.; Madhavan, V.; Jamneala, T.; Crommie, M. F. *Phys. Rev. Lett.* **1998**, *80*, 1469–1472.

[83] Mavrikakis, M.; Stoltze, P.; Nørskov, J. *Catal. Lett.* **2000**, *64*, 101–106.

[84] Ireta, J.; Neugebauer, J.; Scheffler, M. *J. Phys. Chem. A* **2004**, *108*, 5692–5698.

[85] Rao, L.; Ke, H.; Fu, G.; Xu, X.; Yan, Y. *J. Chem. Theory Comput* **2009**, *5*, 86–96.

[86] Bucher, J.-P.; Santesson, L.; Kern, K. *Langmuir* **1994**, *10*, 979–983.

[87] Sánchez-portal, D.; Ordejón, P.; Artacho, E.; Soler, J. M. *Int. J. Quantum Chem.* **1997**, *65*, 453–461.

[88] Krüger, D.; Fuchs, H.; Rousseau, R.; Marx, D.; Parrinello, M. *J. Chem. Phys.* **2001**, *115*, 4776–4786.

[89] Letardi, S.; Cleri, F. *J. Chem. Phys.* **2004**, *120*, 10062–10068.

[90] Gonella, G.; Terreni, S.; Cvetko, D.; Cossaro, A.; Mattera, L.; Cavalleri, O.; Rolandi, R.; Morgante, A.; Floreano, L.; Canepa, M. *J. Phys. Chem. B* **2005**, *109*, 18003–18009.

[91] Kühnle, A.; Linderoth, T. R.; Schunack, M.; Besenbacher, F. *Langmuir* **2006**, *22*, 2156–2160.

[92] Dobrowolski, J. C.; Rode, J. E.; Sadlej, J. *J. Mol. Struct. (THEOCHEM)* **2008**, *130*, 129–134.

[93] Lee, K.; Yu, J.; Morikawa, Y. *Phys. Rev. B* **2007**, *75*, 045402–1–5.

[94] Iori, F.; Felice, R. D.; Molinari, E.; Corni, S. *J. Comput. Chem.* **2009**, *30*, 1465–1476.

[95] Popa, T.; Paci, I. *Soft Mater.* **2013**, *9*, 7988–7998.

[96] Daniel, M.-C.; Astruc, D. *Chem. Rev.* **2004**, *104*, 293–346.

[97] Aryal, S.; B.K.C., R.; Dharmaraj, N.; Bhattarai, N.; Kim, C. H.; Kim, H. Y. *Spectrochim. Acta, Part A* **2006**, *63*, 160–163.

[98] Christensen, C. H.; Nørskov, J. K. *J. Chem. Phys.* **2008**, *128*, 182503–1–8.

[99] Nørskov, J. K.; Bligaard, T.; Hvolbæk, B.; Abild-Pedersen, F.; Chorkendorff, I.; Christensen, C. H. *Chem. Soc. Rev.* **2008**, *37*, 2163–2171.

[100] Ionita, P.; Volkov, A.; Jeschke, G.; Chechik, V. *Anal. Chem.* **2008**, *80*, 95–106.

[101] Lopez-Acevedo, O.; Tsunoyama, H.; Tsukuda, T.; Häkkinen, H.; Aikens, C. M. *J. Am. Chem. Soc.* **2010**, *132*, 8210–8218.

[102] Mostafa, S.; Behafarid, F.; Croy, J. R.; Ono, L. K.; Li, L.; Yang, J. C.; Frenkel, A. I.; Cuenya, B. R. *J. Am. Chem. Soc.* **2010**, *132*, 15714–15719.

[103] Toma, H. E.; Zamarion, V. M.; Toma, S. H.; Araki, K. *J. Braz. Chem. Soc.* **2010**, *21*, 1158–1176.

[104] Sui, R.; Lesage, K. L.; Carefoot, S. K.; Fürstenhaupt, T.; Rose, C. J.; Marriott, R. A. *Langmuir* **2016**, *32*, 9197–9205.

[105] Tlahuice-Flores, A. *Phys. Chem. Chem. Phys.* **2016**, *18*, 27738–27744.

[106] Pirkle, W. H.; Liu, Y. *J. Chromatogr.* **1996**, *749*, 19–24.

[107] Tissot, O.; Gouygou, M.; Dallemer, F.; Daran, J.-C.; Balavoine, G. G. *Angew. Chem. Int. Ed.* **2001**, *40*, 1076–1078.

[108] Popa, T.; Paci, I. *Chem. Phys. Lett.* **2011**, *507*, 128–133.

[109] Kühnle, A.; Molina, L. M.; Linderoth, T. R.; Hammer, B.; Besenbacher, F. *Phys. Rev. Lett.* **2004**, *93*, 086101–1–4.

[110] Canepa, M.; Lavagnino, L.; Pasquali, L.; Moroni, R.; Bisio, F.; Renzi, V. D.; Terreni, S.; Mattera, L. *J. Phys.: Condens. Matter* **2009**, *21*, 264005–1–7.

[111] Maksymovych, P.; Sorescu, D. C.; Yates, J. T. *Phys. Rev. Lett.* **2006**, *97*, 146103–1–4.

[112] Buimaga-Iarinca, L.; Morari, C. *Theor. Chem. Acc.* **2014**, *133*, 1502–1–11.

[113] Wang, Y.; Hush, N. S.; Reimers, J. R. *Phys. Rev. B* **2007**, *75*, 233416–1–4.

[114] Liu, Y.; Ozolins, V. *J. Phys. Chem. C* **2012**, *116*, 4738–4747.

[115] Hanke, F.; Björk, J. *Phys. Rev. B* **2013**, *87*, 235422–1–6.

[116] Renzi, V. D.; Lavagnino, L.; Corradini, V.; Biagi, R.; Canepa, M.; del Pennino, U. *J. Phys. Chem. C* **2008**, *112*, 14439–14445.

[117] Buimaga-Iarinca, L.; Morari, C. *RSC. Adv.* **2013**, *3*, 5036–5044.

[118] Ataman, E.; Isvoranu, C.; Andersen, J. N.; Schnadt, J.; Schulte, K. *J. Phys. Chem. Lett.* **2011**, *2*, 1677–1681.

[119] Woo, H.-K.; Lau, K.-C.; Wang, X.-B.; Wang, L.-S. *J. Phys. Chem. A* **2006**, *110*, 12603–12606.

[120] Oomens, J.; Steill, J. D.; Redlich, B. *J. Am. Chem. Soc.* **2009**, *131*, 4310–4319.

[121] Cossaro, A.; Dell'Angela, M.; Verdini, A.; Puppin, M.; Kladnik, G.; Coreno, M.; de Simone, M.; Kivimäki, A.; Cvetko, D.; Canepa, M.; Floreano, L. *J. Phy. Chem. C* **2010**, *114*, 15011–15014.

[122] Ataman, E.; Isvoranu, C.; Knudsen, J.; Schulte, K.; Andersen, J. N.; Schnadt, J. *Surf. Sci.* **2011**, *605*, 179–186.

[123] George, S.; Sneh, O.; Dillon, A.; Wise, M.; Ott, A.; Okada, L.; Way, J. *Appl. Surf. Sci.* **1994**, *82/83*, 460–467.

[124] Dillon, A.; Ott, A.; Way, J.; George, S. *Surf. Sci.* **1995**, *322*, 230–242.

[125] Sneh, O.; Wise, M.; Ott, A.; Okada, L.; George, S. *Surf. Sci.* **1995**, *334*, 135–152.

[126] Fang, G.; Chen, S.; Li, A.; Ma, J. *J. Phys. Chem. C* **2012**, *116*, 26436–26448.

[127] Burton, B. B.; Kang, S. W.; Rhee, S. W.; George, S. M. *J. Phys. Chem. C* **2009**, *113*, 8249–8257.

[128] Klaus, J. W.; Ott, A. W.; Johnson, J. M.; George, S. M. *Appl. Phys. Lett.* **1997**, *70*, 1092–1094.

[129] Ferguson, J. D.; Smith, E. R.; Weimer, A. W.; George, S. M. *J. Electrochem. Soc.* **2004**, *151*, G528–G535.

[130] Chen, S.; Qian, G. F. X.; Li, A.; Ma, J. *J. Phys. Chem. C* **2011**, *115*, 23363–23373.

[131] Du, Y.; Du, X.; George, S. M. *Thin Solid Films* **2005**, *491*, 43–53.

[132] Hiller, D. et al. *J. Appl. Phys.* **2010**, *107*, 064314–1–10.

[133] Klaus, J.; George, S. *Surf. Sci.* **2000**, *447*, 81–90.

[134] Du, Y.; Du, X.; George, S. M. *J. Phys. Chem. C* **2007**, *111*, 219–226.

[135] Iori, F.; di Felice, R.; Molinari, E.; Corni, S. *J. Comput. Chem.* **2008**, *30*, 1465–1476.

[136] Wright, L. B.; Rodger, P. M.; Walsh, T. R.; Corni, S. *J. Phys. Chem. C* **2013**, *117*, 24292–24306.

[137] Oroguchi, T.; Nakasako, M. *Sci. Rep.* **2017**, *7*, 15859–1–14.

[138] van Duin, A. C.; Dasgupta, S.; Lorant, F.; III, W. A. G. *J. Phys. Chem. A* **2001**, *105*, 9396–9409.

[139] Strachan, A.; Kober, E. M.; van Duin, A. C.; Oxgaard, J.; III, W. A. G. *J. Chem. Phys.* **2005**, *122*, 054502–1–10.

[140] Buehler, M.; van Duin, A.; Goddard, W. *Phys. Rev. Lett.* **2006**, *96*, 095505–1–4.

[141] Kulkarni, A. D.; Truhlar, D. G.; Srinivasan, S. G.; van Duin, A. C.; Norman, P.; Schwartzentruber, T. E. *J. Phys. Chem. C* **2013**, *117*, 258–269.

[142] Deetz, J. D.; Faller, R. *J. Phys. Chem. B* **2014**, *118*, 10966–10978.

[143] Lopez, N.; Nørskov, J. K. *J. Am. Chem. Soc.* **2002**, *124*, 11262–11263.

[144] Ting, E. C. M.; Popa, T.; Paci, I. *Beilstein J. Nanotechnol.* **2016**, *7*, 53–61.

[145] Lee, J.-G.; Lee, J.; Yates, J. T. *J. Am. Chem. Soc.* **2004**, *126*, 440–441.

[146] Batchelder, D. N.; Evans, S. D.; Freeman, T. L.; Häusling, L.; Ringsdorf, H.; Wolf, H. *J. Am. Chem. Soc.* **1994**, *116*, 1050–1053.

[147] Rojas, M. T.; Königer, R.; Stoddart, J. F.; Kaifer, A. E. *J. Am. Chem. Soc.* **1995**, *117*, 336–343.

[148] Ulman, A. *Chem. Rev.* **1996**, *96*, 1533–1554.

[149] Collard, D. M.; Sayre, C. N. *Synth. Met.* **1997**, *84*, 329–332.

[150] Flink, S.; Boukamp, B. A.; van den Berg, A.; van Veggel, F. C.; Reinhoudt, D. N. *J. Am. Chem. Soc.* **1998**, *120*, 4652–4657.

[151] Yan, L.; Huck, W. T. S.; Zhao, X.-M.; Whitesides, G. M. *Langmuir* **1999**, *15*, 1208–1214.

[152] Imahori, H.; Norieda, H.; Yamada, H.; Nishimura, Y.; Yamazaki, I.; Sakata, Y.; Fukuzumi, S. *J. Am. Chem. Soc.* **2001**, *123*, 100–110.

[153] Sek, S.; Palys, B.; Bilewicz, R. *J. Phys. Chem. B* **2002**, *106*, 5907–5914.

[154] Beer, P. D.; Davis, J. J.; Drillsma-Milgrom, D. A.; Szemes, F. *Chem. Commun.* **2002**, 1716–1717.

[155] Yokkota, Y.; Fukui, K.; Enoki, T.; Hara, M. *J. Am. Chem. Soc.* **2007**, *129*, 6571–6575.

[156] Hsu, S.-H.; Reinhoudt, D. N.; Huskens, J.; Velders, A. H. *J. Mater. Chem.* **2011**, *21*, 2428–2444.

[157] Fernández-Ramos, A.; Cabaleiro-Lago, E.; Hermida-Ramón, J.; Martínez-Núñez, E.; Peña-Gallego, A. *J. Molec. Struc.* **2000**, *498*, 191–200.

[158] Moggach, S. A.; Clark, S. J.; Parsons, S. *Acta. Crystallogr. E* **2005**, *61*, 02739–02742.

[159] Thomsen, L.; Wharmby, M.; Riley, D.; Held, G.; Gladys, M. *Surf. Sci.* **2009**, *603*, 1253–1261.

[160] Okamoto, Y. *J. Phys. Chem. B* **1999**, *103*, 11074–11077.

[161] Huang, L.; Han, B.; Han, B.; Derecskei-Kovacs, A.; Xiao, M.; Lei, X.; O'Neill, M. L.; Pearlstein, R. M.; Chandra, H.; Cheng, H. *J. Phys. Chem. C* **2013**, *117*, 19454–19463.

[162] Duan, Y.; Lin, J.-M.; Teplyakov, A. V. *J. Phys. Chem. C* **2015**, *119*, 13670–13681.

[163] Capelo, R. G.; Leppert, L.; Albuquerque, R. Q. *J. Phys. Chem. C* **2014**, *118*, 21647–21654.

[164] Zhang, P. *J. Phys. Chem. C* **2014**, *118*, 25291–25299.

[165] Duchesne, P. N.; Zhang, P. *J. Phys. Chem. C* **2014**, *118*, 21714–21721.

[166] Calle-Vallejo, F.; Tymoczko, J.; Colic, V.; Vu, Q. H.; Pohl, M. D.; Morgenstern, K.; Loffreda, D.; Sautet, P.; Schuhmann, W.; Bandarenka, A. S. *Science* **2015**, *350*, 185–189.

[167] Yourdshadyan, Y.; Rappe, A. M. *J. Chem. Phys.* **2002**, *117*, 825–833.

[168] Cohen, A. J.; Mori-Sánchez, P.; Yang, W. *Chem. Rev.* **2012**, *112*, 289–320.

[169] Tavazza, F.; Senftle, T. P.; Zou, C.; Becker, C. A.; van Duin, A. C. T. *J. Phys. Chem. C* **2015**, *119*, 13580–13589.

[170] Ulissi, Z. W.; Tang, M. T.; Xiao, J.; Liu, X.; Torelli, D. A.; Karamad, M.; Cummins, K.; Hahn, C.; Lewis, N. S.; Jaramillo, T. F.; Chan, K.; Nørskov, J. K. *ACS Catal.* **2017**, *7*, 6600–6608.

[171] Roux, M. V.; Foces-Foces, C.; Notario, R.; da Silva, M. A. V. R.; das Dores M. C. Ribeiro da Silva, M.; Santos, A. F. L. O. M.; Juaristi, E. *J. Phys. Chem. B* **2010**, *114*, 10530–10540.

[172] Payne, M.; Teter, M.; Allan, D.; Arias, T.; Joannopoulos, J. *Rev. Mod. Phys.* **1992**, *64*, 1045–1097.

[173] Soler, J. M.; Artacho, E.; Gale, J. D.; García, A.; Junquera, J.; Ordejón, P.; Sánchez-Portal, D. *J. Phys.: Condens. Matter* **2002**, *14*, 2745–2779.

[174] Sankey, O. F.; Niklewski, D. J. *Phys. Rev. B* **1989**, *40*, 3979–3995.

[175] Ordejón, P.; Artacho, E.; Soler, J. M. *Phys. Rev. B* **1996**, *53*, 441–444.

[176] Fattebert, J.-L. *J. Phys.: Condens. Matter* **2008**, *20*, 294210–1–6.

[177] Torralba, A. S.; Todorović, M.; Brázdová, V.; Choudhury, R.; Miyazaki, T.; Gillan, M. J.; Bowler, D. R. *J. Phys.: Condens. Matter* **2008**, *20*, 294206–1–8.

[178] Kohn, W.; Sham, L. J. *Phys. Rev.* **1965**, *140*, 1133–1138.

[179] Pople, J. A.; Gill, P. M.; Johnson, B. G. *Chem. Phys. Lett.* **1992**, *199*, 557–560.

[180] Rudberg, E. *Fock Matrix Construction for Large Systems*; 2006; pp 1–28.

[181] Jensen, F. *Introduction to Computational Chemistry*; John Wiley & Sons, Ltd, 2007; pp 80–132.

[182] Yang, K.; Zheng, J.; Zhao, Y.; Truhlar, D. G. *J. Chem. Phys.* **2010**, *132*, 164117–1–10.

[183] Clark, S. DFT: Exchange-Correlation. `http://www.tcm.phy.cam.ac.uk/castep/oxford/xc.pdf`, University of Durham.

[184] Becke, A. D. *J. Chem. Phys.* **1993**, *96*, 5648–5652.

[185] Adamo, C.; Barone, V. *J. Chem. Phys.* **1999**, *110*, 6158–6170.

[186] Sousa, S. F.; Fernandes, P. A.; Ramos, M. J. *J. Phys. Chem. A* **2007**, *111*, 10439–10452.

[187] Giese, T. J.; York, D. M. *J. Chem. Phys.* **2010**, *133*, 244107–1–10.

[188] Cancio, A. C.; Stewart, D.; Kuna, A. *J. Chem. Phys.* **2016**, *144*, 084107–1–17.

[189] Mardirossian, N.; Head-Gordon, M. *Mol. Phys.* **2017**, *115*, 2315–2372.

[190] Patra, A.; Bates, J. E.; Sun, J.; Perdew, J. P. *PNAS* **2017**, *114*, E9188–E9196.

[191] Zhao, Y.; Truhlar, D. G. *Theor. Chem. Acc.* **2008**, *120*, 215–241.

[192] Staroverov, V. N.; edited by N. Sukumar, *Density-functional approximations for exchange and correlation*; John Wiley & Sons, 2012; pp 125–156.

[193] Grimme, S.; Hansen, A.; Brandenburg, J. G.; Bannwarth, C. *Chem. Rev.* **2016**, *116*, 5105–5154.

[194] Troullier, N.; Martins, J. L. *Phys. Rev. B* **1991**, *43*, 1993–2006.

[195] García-Gil, S.; García, A.; Lorente, N.; Ordejón, P. *Phys. Rev. B* **2009**, *79*, 075441–1–9.

[196] Frisch, M. J. et al. Gaussian 09 Revision A and Revision D. Gaussian Inc. Wallingford CT 2009.

[197] Sherrill, D. Counterpoise Correction and Basis Set Superposition Error. http://vergil.chemistry.gatech.edu/notes/.

[198] Wise, Q. Grimme DFT-D2 and the BSSE counterpoise correction: Tutorial on calculating the interlayer distance of bilayer graphene. Version 2015.2.

[199] Zhao, J.; Buldum, A.; Han, J.; Lu, J. P. *J. Nanotechnol.* **2002**, *13*, 195–200.

[200] Woods, L. M.; Badescu, S. C.; Reinecke, T. L. *Phys. Rev. B* **2007**, *75*, 155415–1–9.

[201] Mateo-Martí, E.; Rogero, C.; Gonzalez, C.; Sobrado, J. M.; de Andrés, P. L.; Martin-Gago, J. A. *Langmuir* **2010**, *26*, 4113–4118.

[202] Sinnokrot, M. O.; Sherrill, C. D. *J. Phys. Chem. A* **2004**, *108*, 10200–10207.

[203] Langreth, D. C. et al. *J. Phys.: Condens. Matter* **2009**, *21*, 084203–1–15.

[204] Rosa, M.; Corni, S.; Felice, R. D. *Phys. Rev. B* **2014**, *90*, 125448–1–8.

[205] Kohn, W.; Meir, Y.; Makarov, D. E. *Phys. Rev. Lett.* **1998**, *80*, 4153–4156.

[206] Misquitta, A. J.; Jeziorski, B.; Szalewicz, K. *Phys. Rev. Lett.* **2003**, *91*, 033201–1–4.

[207] Wang, J.; Selloni, A. *J. Phys. Chem. C* **2007**, *111*, 12149–12151.

[208] Voznyy, O.; Dubowski, J. J. *J. Phys. Chem. C* **2008**, *112*, 3726–3733.

[209] Rao, L.; Ke, H.; Fu, G.; Xu, X.; Yan, Y. *J. Chem. Theory Comput.* **2009**, *5*, 86–96.

[210] Wu, X.; Vargas, M. C.; Nayak, S.; Lotrich, V.; Scoles, G. *J. Chem. Phys.* **2001**, *115*, 8748–8757.

[211] Latil, S.; Roche, S.; Mayou, D.; Charlier, J.-C. *Phys. Rev. Lett.* **2004**, *92*, 256805–1–4.

[212] Grimme, S. *J. Comput. Chem.* **2004**, *25*, 1463–1473.

[213] Grimme, S. *J. Comput. Chem.* **2006**, *27*, 1787–1799.

[214] Grimme, S.; Antony, J.; Ehrlich, S.; Krieg, H. *J. Chem. Phys.* **2010**, *132*, 154104–1–19.

[215] Ruiz, V. G.; Liu, W.; Zojer, E.; Scheffler, M.; Tkatchenko, A. *Phys. Rev. Lett.* **2012**, *108*, 146103–1–5.

[216] Nazmutdinov, R. R.; Manyurov, I. R.; Zinkicheva, T. T.; Jang, J.; Ulstrup, J. *Russ. J. Electrochem.* **2007**, *43*, 328–341.

[217] Dion, M.; Rydberg, H.; Schröder, E.; Langreth, D. C.; Lundqvist, B. I. *Phys. Rev. Lett.* **2004**, *92*, 246401–1–4.

[218] Vydrov, O. A.; Voorhis, T. V. *J. Chem. Phys.* **2010**, *133*, 244103–1–9.

[219] Berland, K.; Hyldgaard, P. *Phys. Rev. B* **2014**, *89*, 035412–1–8.

[220] Artacho, E.; Cela, J. M.; Gale, J. D.; García, A.; Junquera, J.; Martin, R. M.; Ordejón, P.; Sánchez-Portal, D.; Soler, J. M. **2016**,

[221] Greber, T.; Šljivančanin, Ž.; Schillinger, R.; Wider, J.; Hammer, B. *Phys. Rev. Lett.* **2006**, *96*, 056103–1–4.

[222] Naitabdi, A.; Humblot, V. *Appl. Phys. Lett.* **2010**, *97*, 223112–1–3.

[223] Schlenoff, J. B.; Li, M.; Ly, H. *J. Am. Chem. Soc.* **1995**, *117*, 12528–12536.

[224] Poirier, G. E. *Chem. Rev.* **1997**, *97*, 1117–1127.

[225] Larsson, J. A.; Nolan, M.; Greer, J. C. *J. Phys. Chem. B* **2002**, *106*, 5931–5937.

[226] Chaki, N. K.; Vijayamohanan, K. *Biosens. Bioelectron.* **2002**, *17*, 1–12.

[227] Bilić, A.; Reimers, J. R.; Hush, N. S. *J. Chem. Phys.* **2005**, *122*, 094708–1–15.

[228] Schmid, G. *Chem. Soc. Rev.* **2008**, *37*, 1909–1930.

[229] Heimel, G.; Romaner, L.; Zojer, E.; Bredas, J.-L. *Acc. Chem. Res.* **2008**, *41*, 721–729.

[230] Cao, R. J.; Díaz-García, A. M.; Cao, R. *Coord. Chem. Rev.* **2009**, *253*, 1262–1275.

[231] Eckermann, A. L.; Feld, D. J.; Shaw, J. A.; Meade, T. J. *Coord. Chem. Rev.* **2010**, *254*, 1769–1802.

[232] Maksymovych, P.; Voznyy, O.; Dougherty, D. B.; Sorescu, D. C.; Jr., J. T. Y. *Prog. Surf. Sci.* **2010**, *85*, 206–240.

[233] Pensa, E.; Cortés, E.; Corthey, G.; Carro, P.; Vericat, C.; Fonticelli, M. H.; Benítez, G.; Rubert, A. A.; Salvarezza, R. C. *Acc. Chem. Res.* **2012**, *45*, 1183–1192.

[234] Zhao, P.; Li, N.; Astruc, D. *Coord. Chem. Rev.* **2013**, *257*, 638–665.

[235] Zeng, C.; Jin, R. *Struct. Bond.* **2014**, *161*, 87–115.

[236] Humblot, V.; Barlow, S.; Raval, R. *Prog. Surf. Sci.* **2004**, *76*, 1–19.

[237] Barlow, S.; Raval, R. *Curr. Opin. Colloid Interface Sci.* **2008**, *13*, 65–73.

[238] Zaera, F. *J. Phys. Chem. C* **2008**, *112*, 16196–16203.

[239] Gautier, C.; Bürgi, T. *ChemPhysChem* **2009**, *10*, 483–492.

[240] Mark, A. G.; Forster, M.; Raval, R. *ChemPhysChem* **2011**, *12*, 1474–1480.

[241] Weissbuch, I.; Lahav, M. *Chem. Rev.* **2011**, *111*, 3236–3267.

[242] González-Campo, A.; Amabilino, D. B. *Top. Curr. Chem.* **2012**, *333*, 109–156.

[243] Perdew, J. P.; Burke, K.; Wang, Y. *Phys. Rev. B* **1996**, *54*, 16533–16539.

[244] López-Lozano, X.; Pérez, L. A.; Garzón, I. L. *Phys. Rev. Lett.* **2006**, *97*, 233401–1–4.

[245] Pérez, L. A.; López-Lozano, X.; Garzón, I. L. *Eur. Phys. J. D* **2009**, *52*, 123–126.

[246] Wetterer, S. M.; Lavrich, D. J.; Cummings, T.; Bernasek, S. L.; Scoles, G. *J. Phys. Chem. B* **1998**, *102*, 9266–9275.

[247] Lang, S. M.; Bernhardt, T. M.; Barnett, R. N.; Landman, U. *ChemPhysChem* **2010**, *11*, 1570–1577.

[248] Bilić, A.; Reimers, J. R.; Hush, N. S.; Hafner, J. *J. Chem. Phys.* **2002**, *116*, 8981–8987.

[249] Li, Z.; Kosov, D. S. *Phys. Rev. B* **2007**, *76*, 035415–1–7.

[250] Hoft, R. C.; Ford, M. J.; McDonagh, A. M.; Cortie, M. B. *J. Phys. Chem. C* **2007**, *111*, 13886–13891.

[251] de la Llave, E.; Clarenc, R.; Schiffrin, D. J.; Williams, F. J. *J. Phys. Chem. C* **2014**, *118*, 468–475.

[252] Hauptmann, N.; Robles, R.; Abufager, P.; Lorente, N.; Berndt, R. *J. Phys. Chem. Lett.* **2016**, *7*, 1984–1990.

[253] Tian, Z.; Pawlow, A.; Poutsma, J. C.; Kass, S. R. *J. Am. Chem. Soc.* **2007**, *129*, 5403–5407.

[254] Zhang, H.-M.; Su, G.-J.; Wang, D.; Wan, L.-J.; Jin, G.; Bai, C.-L.; Zhou, X. *Electrochim. Acta* **2004**, *49*, 1629–1633.

[255] Zhang, J.; Demetriou, A.; Welinder, A. C.; Albrecht, T.; Nichols, R. J.; Ulstrup, J. *Chem. Phys.* **2005**, *319*, 210–221.

[256] Schiffrin, A.; Riemann, A.; Auwärter, W.; Pennec, Y.; Weber-Bargioni, A.; Cvetko, D.; Cossaro, A.; Morgante, A.; Barth, J. V. *PNAS* **2007**, *104*, 5279–5284.

[257] Felice, R. D.; Selloni, A. *J. Chem. Phys.* **2004**, *120*, 4906–4914.

[258] Roper, M.; Skegg, M.; Fisher, C.; Lee, J.; Dhanak, V.; Woodruff, D.; Jones, R. G. *Chem. Phys. Lett.* **2004**, *389*, 87–91.

[259] Hu, G.; Jin, R.; en Jiang, D. *Nanoscale* **2016**, *8*, 20103–20110.

[260] Toyoda, K.; Hamada, I.; Lee, K.; Yanagisawa, S.; Morikawa, Y. *J. Chem. Phys.* **2010**, *132*, 134703–1–9.

[261] Vanin, M.; Mortensen, J. J.; Kelkkanen, A. K.; Garcia-Lastra, J. M.; Thygesen, K. S.; Jacobsen, K. W. *Phys. Rev. B* **2010**, *81*, 081408–1–4.

[262] Chapman, C.; Paci, I. *J. Phys. Chem. C* **2010**, *114*, 20556–20563.

[263] Torrelles, X.; Vericat, C.; Vela, M. E.; Fonticelli, M. H.; Millone, M. A. D.; Felici, R.; Lee, T.-L.; Zegenhagen, J.; Muñoz, G.; Martín-Gago, J. A.; Salvarezza, R. C. *J. Phys. Chem. B* **2006**, *110*, 5586–5594.

[264] Higai, S.; Nara, J.; Ohno, T. *Surf. Sci.* **2006**, *600*, 685–692.

[265] Perdew, J. P.; Burke, K.; Ernzerhof, M. *Phys. Rev. Lett.* **1996**, *77*, 3865–3868.

[266] Lglesias, E.; Prado-Gotor, R. *Phys. Chem. Chem. Phys.* **2015**, *17*, 644–654.

[267] Becke, A. D. *Phys. Rev. A* **1988**, *38*, 3098–3100.

[268] Kaupmees, K.; Trummal, A.; Leito, I. *Croat. Chem. Acta* **2014**, *87*, 385–395.

[269] Hall, H. K. J. *J. Am. Chem. Soc.* **1957**, *79*, 5441–5444.

[270] Kaljurand, I.; Kütt, A.; Sooväli, L.; Rodima, T.; Mäemets, V.; Leito, I.; Koppel, I. A. *J. Org. Chem.* **2005**, *70*, 1019–1028.

[271] Angyal, S. J.; Angyal, C. L. *J. Am. Chem. Soc.* **1952**, *268*, 1461–1466.

[272] Walba, H.; Isensee, R. W. *J. Org. Chem.* **1961**, *26*, 2789 – 2791.

[273] Albert, A.; Phillips, J. N. *J. Chem. Soc.* **1956**, *264*, 1294–1304.